Micromachined Joule-Thomson cryocooler

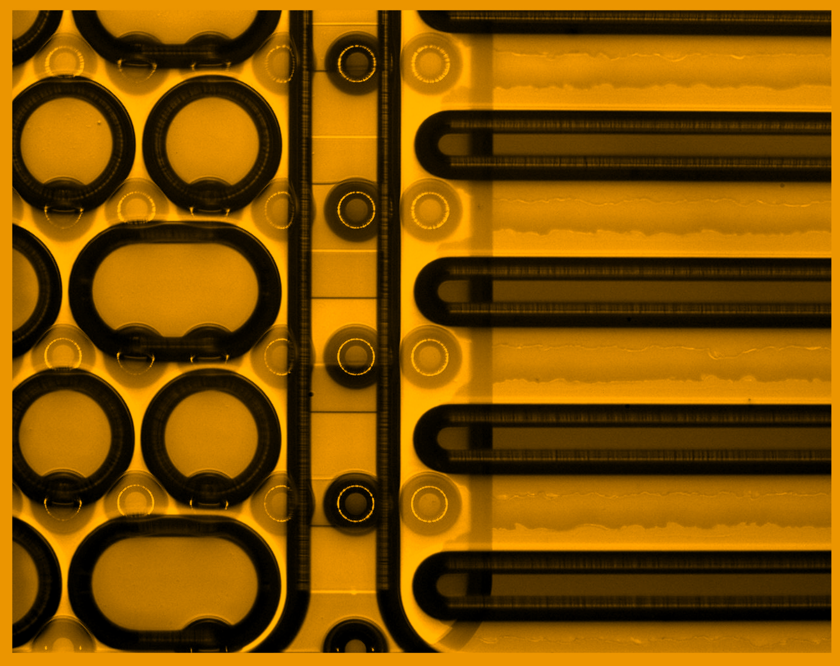

P.P.P.M. Lerou

Micromachined Joule-Thomson cryocooler

The research described in this thesis is part of and financially supported by STW. It was carried out at the Low Temperature Division of the faculty of Science and Technology of the University of Twente.

Print: Ipskamp Print Partners, Enschede.

ISBN 90-365-2458-x

Copyright © 2007, Pieter-Paul Lerou

Micromachined Joule-Thomson cryocooler

PROEFSCHRIFT

ter verkrijging van
de graad van doctor aan de Universiteit Twente,
op gezag van de rector magnificus,
prof. dr. W.H.M. Zijm,
volgens besluit van het College voor Promoties
in het openbaar te verdedigen
op donderdag 22 februari 2007 om 15:00 uur

door

Pieter-Paul Patrick Maurits Lerou

geboren op 18 december 1977
te Nijmegen.

Dit proefschrift is goedgekeurd door de promotoren:

prof. dr. ir. H.J.M. ter Brake
prof. dr. H. Rogalla

Aan mijn familie,
Jos, Mieke en Michiel

Nomenclature

A	area	[m^2]
C	geometric constant	[-]
D_h	hydraulic diameter	[m]
E	modulus of elasticity	[Pa]
G	Gibbs free energy	[J]
G	shear modulus of elasticity	[Pa]
H	enthalpy	[J]
O	perimeter	[m]
P	power	[W]
$\dot{Q}$	heat transfer rate	[W]
S	entropy	[$J \cdot K^{-1}$]
$\dot{S}$	entropy production	[$J \cdot K^{-1} \cdot s^{-1}$]
T	temperature	[K]
U	overall heat transfer coefficient	[$W \cdot m^{-2} \cdot K^{-1}$]
c_p	specific heat capacity	[$J \cdot kg^{-1} \cdot K^{-1}$]
d	characteristic length	[m]
d	thickness	[m]
f	friction factor	[-]
h	specific enthalpy	[$J \cdot kg^{-1}$]
h	heat transfer coefficient	[$W \cdot m^{-2} \cdot K^{-1}$]
l	length	[m]
$\dot{m}$	mass flow rate	[$kg \cdot s^{-1}$]
n	total number of model elements	[-]
p	pressure	[Pa]
s	specific entropy	[$J \cdot kg^{-1} \cdot K^{-1}$]
t	thickness of the CFHX wall	[m]
v	fluid velocity	[$m \cdot s^{-1}$]
v_m	mean fluid velocity	[$m \cdot s^{-1}$]
w	width	[m]

$CFHX$	counterflow heat exchanger	[-]
COP	coefficient of performance	[-]
HX	heat exchanger	[-]
JT	Joule-Thomson	[-]
Kn	Knudsen number	[-]
LH	Linde-Hampson	[-]
$MEMS$	Micro-Electro-Mechanical Systems	[-]
Nu	Nusselt number	[-]
Pr	Prandtl number	[-]
Re	Reynolds number	[-]
St	Stanton number	[-]
Λ	mean free path of gas molecules	[m]
Φ	permeation rate	[Pa·m^3·s^{-1}]
α	thermal diffusivity	[m^2·s^{-1}]
$\overline{\alpha}$	average thermal accommodation coefficient	[-]
ϵ	emissivity	[-]
ϵ	strain	[-]
η	heat exchanger effectiveness	[-]
λ	heat conduction coefficient	[W·m^{-1}·K^{-1}]
μ	dynamic fluid viscosity	[Pa·s]
ν	mean velocity	[m·s^{-1}]
ν	kinematic fluid viscosity	[m^2·s^{-1}]
ρ	density	[kg·m^{-3}]
σ_b	Boltzmann's constant	[W·m^{-2}·K^{-4}]
σ_{bond}	bond stress	[Pa]
$\sigma_\perp$	normal stress	[Pa]
$\sigma_\parallel$	shear stress	[Pa]

Contents

1 Introduction **1**
- 1.1 Project description and motivation . . . 1
- 1.2 Cryogenics . . . 2
- 1.3 MEMS based cryogenic cold stages . . . 4
- 1.4 Thesis outline . . . 5

2 Cold-stage design based on MEMS processing **11**
- 2.1 Substrate materials . . . 11
- 2.2 Fabrication techniques . . . 13
  - 2.2.1 Photolithography . . . 13
  - 2.2.2 Wet chemical etching . . . 14
  - 2.2.3 Abrasive etching . . . 15
  - 2.2.4 Thin film formation . . . 16
  - 2.2.5 Wafer bonding . . . 17
- 2.3 Basic micro cold stage design . . . 18
- 2.4 Conclusions . . . 20

3 Design optimization **25**
- 3.1 Fluid dynamics . . . 25
  - 3.1.1 Reynolds number . . . 25
  - 3.1.2 Pressure drop and friction factor . . . 26
- 3.2 Thermodynamics . . . 28
  - 3.2.1 Convective heat transfer . . . 28
  - 3.2.2 Parasitic heat losses . . . 30
- 3.3 Static models of a CFHX . . . 33
  - 3.3.1 LMTD method . . . 33
  - 3.3.2 Δh method . . . 35
  - 3.3.3 Bahnke-Howard method . . . 37
  - 3.3.4 Static model comparison . . . 38
- 3.4 Dynamic model of a CFHX . . . 39
  - 3.4.1 Dynamic model layout . . . 39
- 3.5 Optimization study . . . 41
  - 3.5.1 Entropy production in the cold stage . . . 42
  - 3.5.2 Optimization of CFHX dimensions . . . 49
  - 3.5.3 Parameter sensitivity of the optimized design . . . 53

3.5.4 Optimum CFHX dimensions for various cooling powers in the mW range . . . 54
3.6 Conclusions . . . 55

4 Mechanical stress compensation **59**
4.1 Strain and stress definition . . . 59
4.1.1 Stress . . . 59
4.1.2 Strain . . . 59
4.1.3 Relationship between stress and strain . . . 60
4.1.4 Failure criteria . . . 60
4.2 Finite element simulation . . . 61
4.3 Pressure tests . . . 62
4.4 Channel pillar configuration . . . 65
4.5 Restriction design . . . 67
4.6 Conclusions . . . 68

5 Micro cold-stage fabrication **71**
5.1 Prototype design specifications . . . 71
5.2 Process scheme . . . 73
5.3 Prototypes . . . 76
5.4 Conclusions . . . 77

6 Measurements **79**
6.1 Measurement setup . . . 79
6.2 Cooler characterization measurements . . . 81
6.2.1 Cool down . . . 81
6.2.2 Cooling power . . . 82
6.2.3 Cool-down time and comparison with the dynamic model . . . 84
6.3 Clogging . . . 84
6.3.1 Clogging phenomenon . . . 84
6.3.2 Uncontrolled clogging at relative high partial water pressure . . . 85
6.3.3 Uncontrolled clogging at relative low partial water pressure . . . 87
6.3.4 Clogging at controlled temperature . . . 90
6.3.5 Clogging prevention . . . 92
6.4 Multi-stage micro cooler . . . 92
6.4.1 Design and measurememts . . . 92
6.4.2 Multi stage recommendations . . . 94
6.5 Conclusions . . . 95

7 Micro vacuum packaging **97**
7.1 Micro vacuum package requirements . . . 97
7.2 Vacuum and gas sources . . . 97
7.2.1 Vaporization . . . 98
7.2.2 Desorption . . . 98
7.2.3 Diffusion . . . 98
7.2.4 Permeation . . . 99
7.3 Required chamber pressure . . . 100
7.4 Gettering . . . 100

7.5 Pirani pressure sensor . . . 101
7.5.1 Electrical feedthrough technology . . . 103
7.6 Packaging design and fabrication . . . 104
7.7 Measurements . . . 106
7.7.1 Sensor calibration . . . 106
7.7.2 Package pressures . . . 107
7.8 Conclusions . . . 108

8 Conclusions and recommendations 111
8.1 Micro cold stage . . . 111
8.1.1 Conclusions . . . 111
8.1.2 Recommendations . . . 112
8.2 Micro vacuum package . . . 114
8.2.1 Conclusions . . . 114
8.2.2 Recommendations . . . 114

9 Outlook 117
9.1 Integration . . . 117
9.2 Compressor . . . 118

Appendices 120

A Gas and cycle properties 121

B Optimization graphs 125

C Fabrication details 127

D Getter data sheet 131

Summary 133

Samenvatting 136

Dankwoord 140

List of publications 144

Chapter 1

Introduction

1.1 Project description and motivation

This thesis describes the research performed in designing, optimizing, and fabricating a cryogenic micro cold stage by means of micromachining. The origin of the project is found in 1995 when Burger et al. started to investigate the possibilities to 'miniaturize' common thermodynamic fluid cooling cycles [1]. They managed to fabricate micro cooler components using Micro-Electro-Mechanical Systems (MEMS) technology [2, 3] and built a demonstrator cooling system [4]. Since 2002, two follow-up projects were initiated in parallel: one on regenerative cooling [5–7] and one on recuperative micro cooling which is the subject of this thesis. The goal of the recuperative micro cooling project is to design and realize a cryogenic micro cold stage which:

- is based on the Linde-Hampson (LH) cooling cycle
- can generate a cooling power in the mW range at a cryogenic temperature
- has a total volume smaller than 1 cm^3
- is fabricated by means of MEMS technology only
- can be integrated with the device to be cooled
- can be integrated with a micro vacuum chamber
- can be combined with a sorption compressor.

One of the advantages of using a LH cooling cycle is that the cold stage has no moving parts. By using a sorption compressor [8–10] the gas cycle will be closed in combination with a total exclusion of any mechanical moving parts. Such a cooler is virtually vibration free and highly durable, which potentially results in a long lifetime. A miniature cryogenic cooler with these properties would be appealing in a wide variety of applications [11] including the cooling of vibration-sensitive detectors in space missions [9, 12], low-noise amplifiers and semi- and superconducting circuitry. Cooling these devices can improve the signal-to-noise ratio and bandwidth of a system [13]. For superconducting devices it is crucial that they are cooled below their critical temperature in order to work [14]. In many cases the system to be cooled is very small thus an accompanying small cryocooler would be obvious. However, such a small cryogenic cooler is not yet available. For thermal insulation and thus to operate properly, the cold stage needs to be situated inside a vacuum environment. This vacuum chamber can also be miniaturized using

MEMS technology [15] as will be discussed in this thesis. A micro cryogenic cold stage combined with a device to be cooled, will be integrated with such a micro vacuum chamber into a single compact unit.

1.2 Cryogenics

Cryogenics is the field of physics which is concerned with the production and investigation of extremely low temperatures, typically temperatures below 120 K. Cryocoolers are based on a whole range of different cooling principles. An overview of the different cryocooling cycles can be found in [16, 17]. All previous micro cooler work presented in section 1.3 as well as the work described in this thesis is based on a Linde-Hampson cycle incorporating Joule-Thomson (JT) expansion (figure 1.1).

In a Linde-Hampson cycle, gas flows continuously through a tubing system. The gas is pressurized isothermally using a compressor (figure 1.1, $1 \rightarrow 2$). After compression the gas flows from the compressor through a counterflow heat exchanger (CFHX) exchanging heat with the gas flowing in the opposite direction inside the low-pressure line ($2 \rightarrow 3$). When the gas has reached the restriction, the gas undergoes isenthalpic expansion to the low-pressure side, cools and usually partially changes its phase to a liquid ($3 \rightarrow 4$) [16, 17]. By absorbing heat from its surroundings the liquid evaporates ($4 \rightarrow 5$) and the vapor flows back through the CFHX absorbing heat from the warm high-pressure side ($5 \rightarrow 1$). In open-cycle systems, the low-pressure gas leaving the CFHX is vented to air, whereas in a closed-cycle system the fluid is re-compressed as is depicted in figure 1.1.

During the JT expansion, the gas expands at constant enthalpy and changes its temperature. Depending on the initial temperature and pressure, this temperature may either decrease or increase.

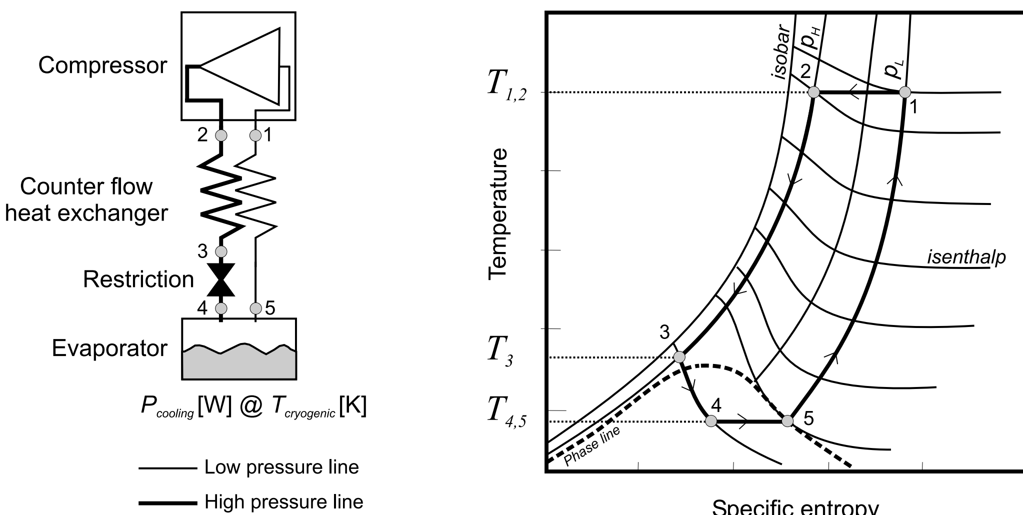

Figure 1.1: Schematic of the Linde-Hampson cooling cycle and the gas cycle drawn in the T-s diagram.

The change of temperature with respect to the change in pressure for a certain gas can be represented by the Joule-Thomson coefficient:

$$\mu_{JT} = (\frac{\delta T}{\delta p})_h \tag{1.1}$$

If the JT coefficient is positive the gas cools during expansion and if its negative the gas heats up. At the inversion point, μ_{JT} equals zero. The temperature at this point is called the inversion temperature and the maximum value where μ_{JT} changes sign is called the maximum inversion temperature [18]. If the inversion temperature of a gas lies above room temperature, it does not need pre-cooling to obtain a cooling effect.

The temperature of the cold tip is determined by the evaporation temperature of the gas at the chosen low pressure. Table 1.1 shows the boiling temperature at 1 bar and maximum inversion temperature of a few different gases. In the search for a cheap, non toxic and inflammable gas which can create a cryogenic temperature and has a maximum inversion temperature above room temperature, nitrogen is an obvious choice. The boiling temperature of nitrogen at 1 bar is about 77 K. Various useful nitrogen gas properties and both a general T-s diagram and a T-s diagram specific for the used Linde-Hampson cycle can be found in appendix A.

With the change in pressure during compression, the gas undergoes a change in enthalpy. According to theory, this change in enthalpy determines the maximum available gross cooling power at the evaporator. For an ideal CFHX there is no enthalpy exchange with the environment and the maximum amount of enthalpy is released by the high-pressure gas and totally absorbed by the low-pressure gas, hence $\Delta h_{23} = \Delta h_{51}$, see figure 1.1 and appendix A.2. Since the JT expansion is assumed to be adiabatic and isenthalpic Δh_{34} equals zero. For the complete cycle the enthalpy change of the gas also is zero. Ergo, the enthalpy change of the fluid in the evaporator equals the enthalpy change during compression: $\Delta h_{45} = -\Delta h_{12}$. The gross cooling power (P_{cool}) is defined by:

$$P_{cool} = \dot{m}\Delta h_{45} = -\dot{m}\Delta h_{12} \tag{1.2}$$

where $\dot{m}$ is the mass flow through the system. To create sufficient cooling power with nitrogen, in other words a large Δh_{12}, a relatively high pressure of 80 bar is chosen at the high-pressure side of the cycle, see appendix A.2. It is our intention in the future to combine the cold stage with a sorption compressor [4, 8–10]. Based on first calculations of a two-stage nitrogen sorption compressor, the low-pressure side is chosen at 6 bar. At this pressure the sorption material of the compressor has considerably more sorption capacity than at lower pressures [8]. This way a cooler with acceptable efficiency can be

	Boiling temperature at 1 bar [K]	Maximum inversion temp. [K]
Oxygen	90.07	761
Argon	87.16	794
Nitrogen	77.20	621
Neon	27.05	213
Hydrogen	20.23	205
Helium-4	4.21	40

Table 1.1: Boiling temperature and maximum inversion temperature of different gases. Data taken from [19].

designed. A pressure change from 80 to 6 bar results for nitrogen in a cooling enthalpy of 14.7 J·g^{-1}, see appendix A.2. The boiling temperature of nitrogen at 6 bar is about 96 K.

The goal is to use the micro cooler for those applications where the device to be cooled has a very low dissipation or no dissipation at all. In these cases the required cooling power is mainly determined by the total parasitic heat load from the environment. By a clever design of the cryogenic enclosure of such a small device, the required cooling power can be limited to a few mW only. To cool down devices with a heat production of just a few mW and bearing in mind the (extra) parasitic heat load which will be induced by the measurement setup (e.g. a temperature sensor, a power resistor, etc), we aim at a net cooling power of about 10 mW. Using equation 1.2, the mass flow will have to be in the order of 1 mg·s^{-1} to create a gross cooling power of 15 mW. This implies that a total parasitic heat loss (exclusive the heat loss due to the measurement setup) of only 5 mW is accepted. The CFHX is a crucial part of the system since a lot of heat is being transported from the high-pressure to the low-pressure gas, which increases the overall COP of the cold stage. In this specific case the total power being transferred inside the CFHX in the ideal cycle is about 225 mW, which is about a factor 16 higher than the gross cooling power. It is therefore essential that the CFHX design is optimized.

1.3 MEMS based cryogenic cold stages

Since the 1980's, different groups around the world have tried to build small cryogenic refrigerators [20–31]. Some focused their interest to MEMS fabrication techniques (see chapter 2) because of its high fabrication accuracy and possibility of batch processing. Previous, most noticeable results were achieved by Little et al. and Burger et al. Both fabricated cold stages which had a total volume of about 1 cm^3 using MEMS technology.

In the 1980's, Little et al. made a range of miniature cold stages [33–36] using an abrasive etching process. The smallest was 15 x 2 x 0.5 mm (0.015 cm^3, see figure 1.2) and used an open-loop JT cycle with nitrogen gas at a high pressure of 165 bar and a

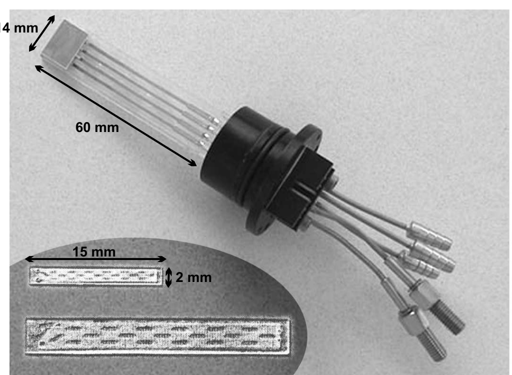

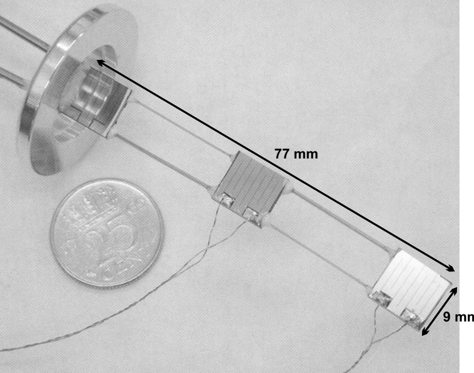

Figure 1.2: On the left: a two stage nitrogen / neon refrigerator made by MMR technologies, Inc. [32] (dimensions 60 x 14 mm) and two prototypes of a micro miniature N_2 refrigerator made by Little et al. [33] shown in the left corner. On the right: a micro machined ethylene cold stage fabricated by Burger et al. [4].

mass flow of about 3 mg·s^{-1}. A cooling power of 25 mW @ 101 K was claimed. The abrasive etching process which was used by Little et al. is a relatively inaccurate and low resolution process when compared to other MEMS etching techniques which will be discussed in chapter 2. Besides the difference in used fabrication techniques, another important distinction between the work of Little et al. and the cold stages presented in this thesis, is that the latter are optimized for maximum cooling power in combination with minimum pressure drop. The coefficients of performance (COP) of the described micro cold stages are approximately doubled compared to the designs fabricated by Little et al. In other words, for the same input power, the net cooling power has roughly doubled. The smallest cold stage that Little et al. have manufactured, see left bottom corner of figure 1.2, was not reproduced or turned into an industrial product probably due to problems with reproducibility. Larger coolers of the same design, however, were made commercially available by MMR technologies, Inc. [32]. Typical dimensions are 60 x 14 x 2 mm (1.7 cm^3). For some applications these coolers are still too large, certainly for those cases where the cooler size is many times larger than the device to be cooled and the demanded cooling power is much smaller than the amount produced. Our research aims at fully optimized, reliable micro cold stages ($V_{total} << 1$ cm^3) that can be manufactured in large quantities.

In early 2000, Burger et al. developed a JT cold stage with a total volume of 0.76 cm^3 (77 x 9 x 1.1 mm), see the right picture of figure 1.2. They combined the cold stage with a sorption compressor, thus realizing for the first time a closed-cycle micro cooler [4]. The cycle used ethylene gas and included a TE pre-cooler connected to the micro cold stage. This miniature cooler had a cooling power of 200 mW @ 170 K. Burger et al. used MEMS technology to construct most of the components of the cold stage. Counterflow heat exchangers were made out of tiny glass capillaries. After fabrication, the different cold-stage parts were glued together.

1.4 Thesis outline

The development of the micro cryogenic cold stage can be divided into five main project steps each treated in a separate chapter. These are:

- investigation of the available MEMS technology, treated in chapter 2
- optimization of the cold-stage design, treated in chapter 3
- calculations concerning mechanical stresses, treated in chapter 4
- final design and micro cold-stage fabrication process, treated in chapter 5
- measurements done on the fabricated cold stages, treated in chapter 6

In more detail the following is discussed in these chapters. Since the cold stage will be fabricated using MEMS technology only, a short introduction and description of some common MEMS fabrication processes is given is chapter 2. We will mainly concentrate on those processes which were actually used during the fabrication of the micro cold stage and the micro vacuum package fabrication process. All used MEMS fabrication techniques have process limitations, so the design of a MEMS based micro cold stage has to satisfy a number of design parameters. Chapter 2 is, therefore, concluded with a basic micro cold stage design.

To optimize the cold-stage design, the temperature profile of the CFHX is needed as will be explained in chapter 3. An introduction into fluid- and thermodynamics, needed to calculate this profile, is given in section 3.1 and 3.2. The CFHX temperature profile is calculated using different static models which are described in section 3.3. A dynamic model, presented in section 3.4, is used to predict the development of the temperature profile of the cold tip through time. The optimization study, done to optimize the CFHX geometry for maximum COP in combination with minimum dimensions, is given in section 3.5.

Since the micro flow channels contain a gas at a very high pressure and the channel walls are extremely thin, high mechanical stresses inside the construction material can be a problem. Calculations and measurements done concerning the stress distribution inside the micro channels are presented in chapter 4. Both the high- and the low-pressure channels contain a pillar configuration to compensate for these mechanical stresses which is presented in section 4.4.

In the first section of chapter 5, MEMS technology, optimal CFHX design and pillar configuration are combined into a final micro cold-stage design. This cold stage, together with seven other designs, all based on it, are fabricated. The fabrication process is described in section 5.2.

All measurements done on the fabricated cold tips are described in chapter 6. Also a comparison between the measurements and the used models is made which is presented in section 6.2. The main problem during operation of a micro cold stage is clogging of the flow restriction. The measurements done to investigate this clogging phenomenon are presented and discussed in section 6.3.

The micro cold stage needs to be situated inside a vacuum environment to operate. All measurements described, were done using a conventional, relatively large vacuum chamber. If the micro cooler is to be turned into a stand-alone commercial product, it would be convenient to integrate the cold stage with a micro vacuum package and the device to be cooled. In chapter 7, the research done to create such a micro vacuum package is presented. In chapter 8, conclusions and recommendations of the project are given.

References

[1] J. Burger. *Cryogenic microcooling, A micromachined cold stage operating with a sorption compressor in a vapor compression cycle*. PhD thesis, University of Twente, 2001.

[2] M. Madou. *Fundamentals of microfabrication*. CRC Press, Boca Raton, USA, 1997.

[3] M. Elwenspoek and H. Jansen. *Silicon Micromachining*. Cambridge University Press, 1998. ISBN 0-521-59054-X.

[4] J.F. Burger, H.J. Holland, J.H. Seppenwoolde, E. Berenschot, H.J.M. ter Brake, J.G.E. Gardeniers, M. Elwenspoek, and H. Rogalla. 165 K microcooler operating with a sorption compressor and a micromachined cold stage. In *Cryocoolers 11*, pages 551–560, New York, 2001. Kluwer Academic/Plenum Publishers.

[5] S. Vanapalli, J.F. Burger, T.T. Veenstra, H.J. Holland, G.C.F. Venhorst, H.V. Jansen, H.J.M. ter Brake, and M. Elwenspoek. Experimental investigation of friction factors for gas flow across dense pillar matrices in microchannels. *proceedings 16th MME conference*, pages 354–357, 2005.

[6] P.P.P.M. Lerou and S. Vanapalli and H.V. Jansen and J.F. Burger and T.T. Veenstra and G.C.F. Venhorst and H.J. Holland and M. Elwenspoek and ter Brake, H.J.M. and H. Rogalla. Microcooling developments at the University of Twente. *to be published in Advances in Cryogenic Engineering*, 51, 2006.

[7] H.J.M. ter Brake, P.P.P.M. Lerou, S. Vanapalli, H.V. Jansen, J.F. Burger, T.T. Veenstra, G.C.F. Venhorst, H.J. Holland, M. Elwenspoek, and H. Rogalla. Microcooling research at the University of Twente. *To be published in ICEC 2006*, 2006.

[8] G. Wiegerinck. *Improving sorption compressors for cryogenic cooling*. PhD thesis, University of Twente, 2005.

[9] J. F. Burger, H. J. M. ter Brake, H. Rogalla, and M. Linder. Vibration-free 5 K sorption cooler for ESA's Darwin mission. *Cryogenics*, 42:97–108, February 2002.

[10] G.F.M. Wiegerinck, J.F. Burger, H.J. Holland, E. Hondebrink, H.J.M. ter Brake, and H. Rogalla. A sorption compressor with a single sorber bed for use with a Linde-Hampson cold stage. *Cryogenics*, 46:9–20, 2006.

[11] G. Walker, R. Fauvel, and G. Reader. Miniature refrigerators for cryogenic sensors and cold electronics. *Cryogenics*, 29:841–845, 1989.

[12] P. Bhandari, M. Prina, R.C. Bowman Jr., C. Paine, D. Pearson, and A. Nash. Sorption coolers using a continuous cycle to produce 20 K for the Planck flight mission. *Cryogenics*, 44:395–401, 2004.

[13] Cheng Chih Yang et al. Cryogenic Characteristics of Wide-Band Pseudomorphic HEMT MMIC Low-Noise Amplifiers. *IEEE Transactions on microwave theory and techniques*, 41:992–997, 1993.

[14] A.E. Mahdi and D.J. Mapps. High-Tc SQUIDs: the ultra sensitive sensors for non-destructive testing and biomagnetism. *Sensors and Actuators*, 81:367–370, 2000.

[15] B. Lee, S. Seok, and K. Chun. A study on wafer level vacuum packaging for MEMS devices. *J. Micromech. Microeng.*, 13:663–669, 2003.

[16] H. J. M. ter Brake. *Cryogenic systems for superconducting devices*, volume 365, pages 561–639. Kluwer Academic Publishers, Dordrecht, 2000. ISBN 0-7923-6113-X.

[17] G. Walker. *Cryocoolers, part 1: Fundamentals*. Plenum Press, New York, 1983.

[18] C.B.P. Finn. *Thermal Physics*. Chapman & Hall, 2nd edition, 1993. ISBN 0-412-49540-6.

[19] Cryocomp, version 3.01. Horizon Techonologies, http://www.htess.com/cryocomp.htm.

[20] Sangkwon Jeong. How difficult is it to make a micro refrigerator? *International Journal of Refrigeration*, 27:309–313, May 2004.

[21] H. J. Holland, J. F. Burger, N. Boersma, H. J. M. ter Brake, and H. Rogalla. Miniature 10-150 mW Linde-Hampson cooler with glass-tube heat exchanger operating with nitrogen. *Cryogenics*, 38:407–410, April 1998.

[22] L. Y. Xiong, G. Kaiser, and A. Binneberg. Theoretical study on a Miniature Joule-Thomson and Bernoulli Cryocooler. *Cryogenics*, 44:801–807, November 2004.

[23] Allan J. Organ. The miniature, reversed Stirling cycle cryo-cooler: integrated simulation of performance. *Cryogenics*, 39:253–266, March 1999.

[24] M. Chorowski, E. Bodio, and M. Wilczek. Development and testing of a miniature Joule-Thomson refrigerator with sintered powder heat exhanger. *Advances in Cryogenic Engineering*, 39:1475–1481, 1994.

[25] A. Karandikar and D. Berchowitz. Low cost small cryocoolers for commercial applications. *Advances in Cryogenic Engineering*, 44, 1995.

[26] Y. Hong, S. Park, H. Kim, and Y. Choi. The cool-down characteristics of a miniature JouleThomson refrigerator. *Cryogenics*, 46:391–395, 2006.

[27] H.T. Chua, X. Wang, and H. Y. Teo. A numerical study of the Hampson-type miniature JouleThomson cryocooler. *International Journal of Heat and Mass Transfer*, 49:582–593, 2006.

[28] K.C. Ng, H. Xue, and J.B. Wang. Experimental and numerical study on a miniature Joule-Thomson cooler for steady-state characteristics. *International Journal of Heat and Mass Transfer*, 45:609–618, 2002.

[29] H. Xue, K.C. Ng, and J. B. Wang. Performance evaluation of the recuperative heat exchanger in a miniature JouleThomson cooler. *Applied Thermal Engineering*, 21:1829–1844, 2001.

[30] B. Eugeniusz, C. Maciej, W. Marta, and B. Arkadiusz. Miniature Joule-Thomson liquefier with sintered heat exchanger . *Cryogenics*, 32 Supplement 1:13–16, 1992.

[31] E. Mikulin, J. Shevich, T. Danilenko, N. Solovov, and V. Veselov. The miniature Joule-Thomson refrigerator. *Cryogenics*, 32 Supplement 1:17–19, 1992.

[32] MMR Technologies Inc. 1400 North Shoreline Boulevard, Mountain View, CA 94043-1346, USA, http://www.mmr.com.

[33] S. Garvey, S. Logan, R. Rowe, and W. A. Little. Performance characteristics of a low-flow rate 25 mW, LN2 Joule-Thomson refrigerator fabricated by photolithographic means. *Appl. Phys. Lett*, 42:1048–1050, June 1983.

[34] W. A. Little. Microminiature refrigeration. *Rev Sci Instrum*, 55:661–680, 1984.

[35] Wu Peiyi and W. A. Little. Measurement of friction factors for the flow of gases in very fine channels used for microminiature Joule-Thomson refrigerators. *Cryogenics*, 23:273–277, May 1983.

[36] Wu Peiyi and W. A. Little. Measurement of the heat transfer characteristics of gas flow in fine channel heat exchangers used for microminiature refrigerators. *Cryogenics*, 24:415–420, 1984.

Chapter 2

Cold-stage design based on MEMS processing

Micro-Electro-Mechanical Systems (MEMS) are mechanical systems of micrometer (micron) size frequently integrated with electronic circuitry. The micro structures are produced on a wafer substrate, often silicon, using micromachining processes. These processes are compatible with integrated circuit technology (ICT) processes which are used to construct the electronics. Patterns are applied on the wafers by lithographic techniques after which the substrate is etched, creating the micro structures and circuits. MEMS fabrication usually consists of a multiple-step process. Since the structures are very tiny, one wafer may contain a large number of devices. The use of batch processing can result in relatively low cost per unit. A basic micro cold-stage design can be defined which is based on a fabrication process using only MEMS technology and taking fabrication process limitations into account.

2.1 Substrate materials

There exists a wide variety of substrate materials to process the micro systems on. Some examples of wafer materials are: silicon, silicon carbide, germanium, quartz, Pyrex glass [1] and borosilicate glass (D263T [2]). Differences between the properties of these substrates include: electrical- and heat conduction properties, conduction type (n or p) and crystal orientation ($< 100 >$,$< 111 >$, and so on). Apart from that, there are also differences in mechanical strength, chemical inertness, optical transparency and available wafer thickness and flatness.

The choice of the fabrication material for the micro cooler depends on a large number of physical properties of the material. The construction material should have a low thermal conductivity to minimize thermal losses. This will be explained extensively in chapter 3. The heat conduction coefficient and its temperature dependence is given for different materials in figure 2.1. At the Transducers Science and Technology Group of the University of Twente, much knowledge is gathered on processing in particular silicon and glass (i.e. Pyrex, Borofloat) wafers using a wide variety of MEMS processes. If the micro cooler is to be constructed using this technology it is required that the fabrication material is supplied in wafer form and is compatible with the available MEMS processes.

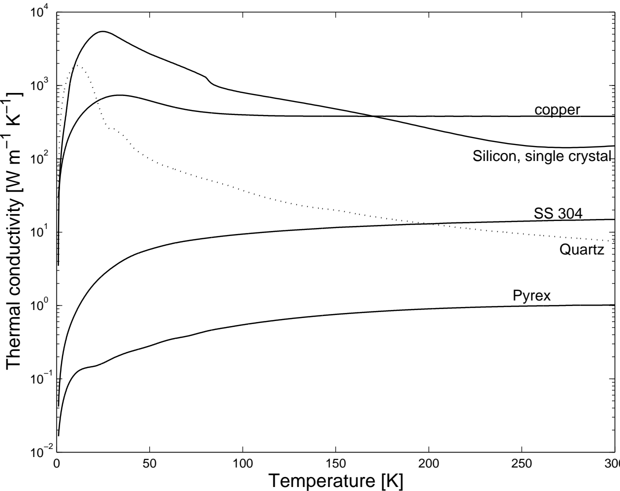

Figure 2.1: Temperature dependence of the thermal conductivity of several materials [3].

In order to withstand mechanical stresses caused by the large gas pressure in the system, the material also requires a large mechanical strength, see chapter 4. Low electrical conductivity is desired if electrical leads are to be integrated with the cooler as will be discussed in chapter 7.

In addition to 'traditional' MEMS fabrication techniques, which will be treated in the next section, there are alternative ways to manufacture micro structures. One example is the so-called PDMS (polydimethylsiloxane) micro-molding process, where PDMS (a polymer) is patterned by pouring it on a already processed silicon or glass wafer [4, 5]. Although the micro-molding process is relatively simple and cheap, PDMS does not have a large mechanical strength and is highly permeable to most gases. Therefore it is not suitable for high-pressure gas applications, like the construction of a micro cooler. Another technique is micromachining metals or glass using laser ablation [6–9]. However, the heat conduction coefficient of most metals is too high and there is not much experience with these techniques at our groups. Furthermore, laser ablation is very expensive and not

Table 2.1: Material properties.

	Si	SiC	Ge	Quartz
Thermal cond. at 300 K [W·m^{-1}·K^{-1}]	106	360	60	7.5
Wafer form	+	+	+	+
Knowledge and technology	+	-	-	+
Electrical resistivity [Ωm]	$1e{-3}$	$1e5$	$5e{-4}$	$7e9$
Young's modulus [GPa]	130	430	103	72
	Pyrex	**Borosilicate**	**SS 304**	**PDMS**
Thermal cond. at 300 K [W·m^{-1}·K^{-1}]	1.0	1.2	14.9	0.2
Wafer form	+	+	-	-
Knowledge and technology	+	+	-	-
Electrical resistivity [Ωm]	$8e12$	$2e13$	$1e{-6}$	$4e13$
Young's modulus [GPa]	67	64	200	0.36-0.87

(yet) suitable for mass production.

Table 2.1 gives an overview of all mentioned materials and their properties. Mainly because of its low thermal conductivity and compatibility with available MEMS technology and knowledge, glass (Pyrex or borosilicate) is an obvious choice for the construction material of the micro cooler. More specific, D263T (a borosilicate glass) is used by Micronit [10] as the construction material to fabricate the cold stages.

2.2 Fabrication techniques

MEMS are manufactured using fabrication techniques like, wet chemical etching (isotropic and anisotropic), dry etching, plasma etching, bonding and many other technologies. Two books which provide a good overview of the various techniques used to fabricate MEMS are 'Silicon Micromachining' [11] and 'Fundamentals of microfabrication' [12]. In the following section, only the MEMS processes which were used to fabricate the micro cooler will be discussed.

2.2.1 Photolithography

The patterns of the different micro shapes, like channels and holes are created on a wafer via photolithography. The process can be explained using figure 2.2. First the wafer is coated with a thin (positive or negative) photoresist layer by spin coating (step I). The resist layer is a polymer which is sensitive to ultraviolet light. The wafer is exposed to a UV-light source through a mask (step II). The mask is a glass plate with a thin chromium layer on one side. In this chrome layer, which is impenetrable for the UV-light, the pattern is printed. At the areas where the UV-light hits the wafer, the polymer is either weakened or strengthened depending on the used resist (positive or negative). After the exposure, the resist is developed (step III). If a positive resist was used, illuminated areas are removed, leaving the desired pattern. However, if a negative resist was used, the illuminated areas stay on the wafer and the rest is washed away. The patterned wafer can be used in an etch process to create the micro structures in the wafer (step IV), see following section. After etching, the wafer is cleaned to remove the etchant and the

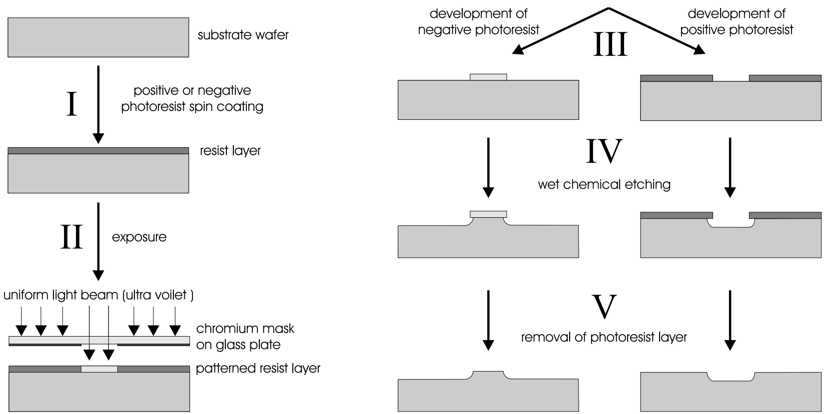

Figure 2.2: Main processing steps of the photolithography and wet etching process.

resist layer (step V). The minimal structure size that can be reached using 'standard' photolithography is roughly 10 μm.

2.2.2 Wet chemical etching

After the photolithography, wet chemical etching can be used to manufacture the micro structures in the substrate wafer. When using wet chemical etching, the patterned wafer is immersed in a liquid reactant. This reactant chemically reacts with the wafer surface dissolving the wafer material. The used resist layer of course has to be immune, or at least highly resistant to the used reactant. Diffusion processes transport the dissolved wafer material away from the surface and provide new reactant to maintain the process. The composition of the reactant depends on the used substrate material. When silicon is used as a substrate material, a mixture of nitric acid (HNO_3) and hydrofluoric acid (HF) in water is a commonly used etchant. The chemical reaction of the etching process can be written as:

$$Si + 2HNO_3 \rightarrow SiO_2 + 2HNO_2$$

$$SiO_2 + 6HF \rightarrow 2H^+ + SiF_6^{2-} + 2H_2O$$

When the wafer material is silicon dioxide (SiO_2 or glass) the common etchant is hydrofluoric acid (HF). The chemical reaction of this etching process is identical to the second chemical equation written above. The etch rate and thus the accuracy of the process, is characteristic for each type of substrate material and depends on the HF concentration in the water. For example for Pyrex glass [1], a HF concentration of 10 % gives an etch rate of 0.5 μm·min^{-1}; 20 % gives an etch rate of 1.5 μm·min^{-1}; 30 % gives an etch rate of 3 μm·min^{-1}; 40 % gives an etch rate of 4.5 μm·min^{-1} [14]. The etch rate of hydrofluoric acid is known to strongly vary over longer etch times [14]. To maintain a constant etch rate, buffering agents are often added to the reactant solution [15]. A known

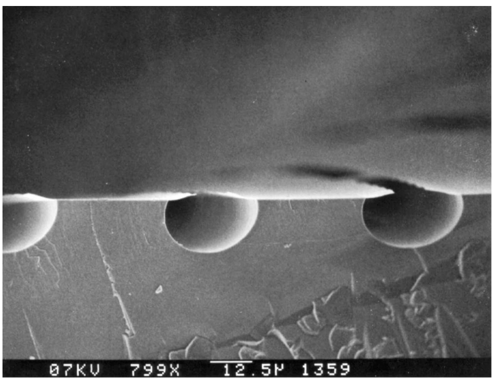

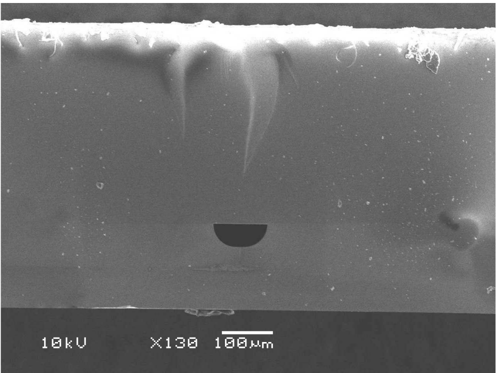

Figure 2.3: SEM pictures of wet etched micro channels. Left: three channels with a width of approximately 30 μm [13]. The photoresist layer is not yet removed and clearly visible. Right: single channel with a width of approximately 110 μm. The channel was closed using a fusion bonding process.

buffer agent is ammonium fluoride (NH_4F). The reactant is, for obvious reasons, then called buffered HF or BHF. The etch rate of BHF is often lower, typically 50 nm·min^{-1}. Examples of wet etched channels can be seen in figure 2.3.

2.2.3 Abrasive etching

The abrasive etching technique (better known as powder blasting) is a micromachining technique where a high-pressure mixture of air and powder particles is accelerated toward a substrate [17, 18]. The powder consists of Al_2O_3 particles (SiC particles are also known to be used) and is accelerated through a nozzle (figure 2.4). Once the particles hit the substrate they erode surface particles. Again, a mask protects parts of the substrate to create different structures. Wensink et al. [16] found a removal rate for glass and silicon of approximately 25 μm·min^{-1}. This rate can be increased by increasing the gas pressure and/or powder flux. The smallest feature size attainable, found by Wensink et al., is about 30 μm with an aspect ratio of 2.5 (figure 2.4). This aspect ratio is considered the absolute limit. A more common ratio, also used during this project, is about 1:1. For this ratio the minimum structure size is about 20 μm [19]. The main disadvantage of powder blasting is the relatively high roughness of the blasted surface which goes hand in hand with the process [20], see figure 2.5. Small imperfections at the sides of the channels are likely to be the starting point of a rupture when a micro channel is pressurized to a high pressure. Also the flow behavior through the micro channels is influenced [21]. Higher roughness results in a higher flow resistance and associated pressure drop [22]. The rough surface can also be more sensitive to clogging. This is why the use of the wet etching process for the fabrication of the micro channels is preferred. Powder blasting is, because of its high aspect ratio, mainly suitable for creating small holes and slits through a wafer.

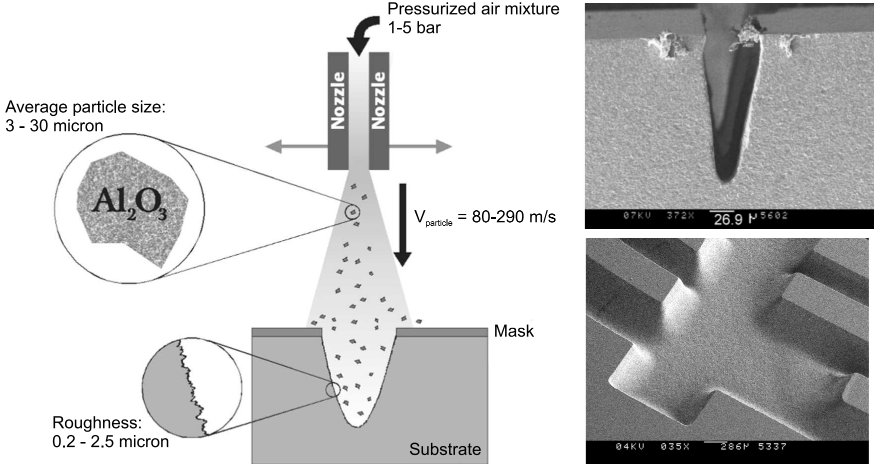

Figure 2.4: Left: schematic impression of the powder blast process[16]. Top rigth: 50 μm wide channel in Pyrex with an aspect ratio of 2.5 (blasted with 9 μm alumina particles at 290 m·s^{-1}). Bottom right: powder blasted micro channels [17].

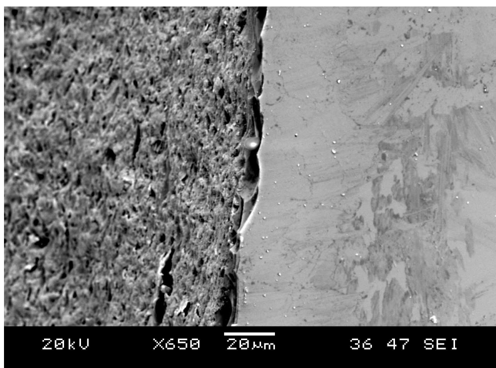

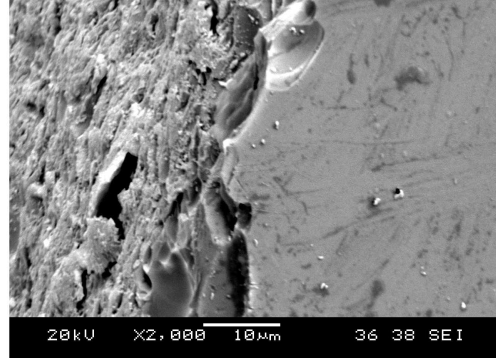

Figure 2.5: SEM pictures of a smooth wafer (right side of both pictures) and a powder blasted area (left side of both pictures).

2.2.4 Thin film formation

Thin film formation is relevant for the micro cooler because it can be used to reduce the radiation losses of the cold stage, see section 3.2.2. Deposition of a thin highly reflecting layer is needed since the emissivity of glass is large (ϵ is 0.8 to 0.95 [23]). A thin gold layer of about 200 nm thick can reduce the emissivity to about 0.02 [24]. There are many methods to create a thin metal film on a substrate. A useful reference which gives an extensive overview of these methods is given in [25]. Because of its good step coverage and adhesion to the substrate, so-called DC sputtering is chosen to deposit a thin layer on the cold stage.

The sputter setup is a pressure vessel filled with Argon gas at a low pressure, see figure 2.6. A sputtering plasma is created by applying a negative DC voltage to an electrode system. The target, which is a disc of the metal that is to be deposited, serves as a cathode. The substrate is situated on the anode. Because of the negative charge, positive Argon ions (Ar^{+}) are accelerated toward the cathode. This bombardment of

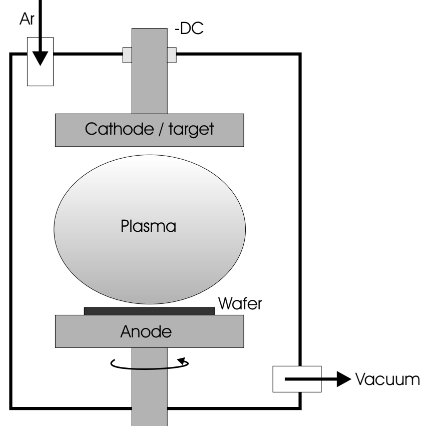

Figure 2.6: Schematic of the DC sputtering setup.

the target with high-energy Ar^+ ions frees surface atoms of the deposit material. These atoms diffuse to the substrate material and deposit on the surface, creating a thin film. Since the target has to function as a cathode, it has to be a conducting material. Some examples of commonly used target materials are: Cr, Pt, Au, Ag, Ta and Ti. To ensure a homogeneous thickness of the layer, the substrate is often rotated.

2.2.5 Wafer bonding

The wafer bonding process refers to the principle that if two wafers are brought in direct contact, the materials fuse and a mechanical fixation occurs. There are many forms of wafer bonding all described in detail in [11]. This section is limited to glass to glass fusion and anodic bonding, because these processes are used during the micro cooler fabrication and the fabrication of a micro vacuum chamber.

In the fusion bonding process, two highly polished, cleaned wafers are brought in direct contact without any intermediate layer, applied high voltage or external high pressure [26–28]. The two wafers will stick together due to atomic attraction forces (van der Waals forces). However, this so-called pre-bond is not very strong. To improve the strength of the bond, the wafer stack is placed in a furnace and undergoes a thermal treatment. Gui et al. investigated the effect of surface roughness on direct wafer bonding and criteria for bondability, depending material properties and bond interface quality were stated [29]. Because a fusion bond purely relies on the flatness of the wafer, the surface roughness has to be less than a few nanometers [30] unlike other bond mechanisms where the roughness can go up to a few tenths of a micron.

Anodic bonding, also known as electrostatic bonding, is performed with a wafer of an electrically conducting material and an ion conducting wafer, for instance silicon and an alkali containing glass [31, 32]. Anodic bonding can also be accomplished between two silicon wafers with an intermediate glass thin film [33]. To achieve glass-to-glass anodic bonding a intermediate layer is needed [34, 35]. Anodic bonding does not require a pre-bond; the wafers can just be placed on top of each other before starting the bonding process. During bonding, a DC voltage is applied across the two wafers, where the glass wafer is connected to the cathode of the power supply and the silicon is connected to the anode. The electrical field causes the positively charged ions to migrate through the glass to the negative electrode, leaving the stronger bound negative ions behind. Initially, the electrical field is uniformly distributed across the glass. However, after the positive ions have drifted towards the cathode, a large potential drop occurs at the glass-silicon interface, which pulls the wafers together. Here the silicon and oxygen react, growing an SiO_2 layer. The bonding is performed at an elevated temperature to increase the mobility of the ions in the glass. This temperature lies in general between 180 and 500 ℃. Anodic bonding is less sensitive to surface roughness compared to fusion bonding. In order to guarantee a hermetic bond, grooves should not exceed 50 nm [36]. In general, the bond strength of an anodic bonded wafer stack for both glass-glass and glass-silicon interfaces [35, 37, 38], is higher than that of a fusion bonded stack [39, 40] although higher low-temperature glass wafer direct bond strengths have been reported by Pigeon et al. [27].

2.3 Basic micro cold stage design

All presented fabrication techniques will be used to construct the micro cold stage. From these techniques, there is always one the most suitable for the fabrication of a specific part of the cold stage. For example powder blasting is excellent for constructing holes whereas wet etched is more suitable for fabricating channels. However, all fabrications techniques have process limitations, some more crucial than others. In summary these are:

- the minimal structure size using 'standard' photolithography: ≈ 10 μm
- the resolution of the powder blasting process: ≈ 5 μm
- the resolution of the HF etch process: ≈ 0.5 μm
- the resolution of the BHF etch process: ≈ 5 nm

Besides these limitations, there is also a limited choice in fabrication material. The standard thickness of a glass wafer is 550 μm. Thinner wafers (down to 50 μm thick) are available but it obviously becomes more difficult to handle and process these wafers. Variability of the glass substrates thickness is standard $\pm 10\%$ according to the manufacturer's specification [2]. A trade-off has to be made to establish a reliable process with acceptable yield using wafers which are as thin as possible, see chapter 5.

A basic micro cooler design can be defined, taking into account the constraints due to technology and complying to the following requirements made in the project description (section 1.1); fabricate a micro cryogenic cooler which is:

- based on the Linde-Hampson (LH) cooling cycle
- fabricated by means of MEMS technology only
- can be combined with a sorption compressor

Figure 2.7 shows a three dimensional view and three different cross-sections of the basic design. The cooling cycle described in section 1.2 is based on a continuous gas cycle working with relatively high pressures. Therefore, the micro cooler will have to have hermetically sealed gas channels which are able to withstand high pressures. The flow channels can be wet chemically etched with a high accuracy into a D263T glass wafer. Because glass has a relatively low thermal conductivity, the heat loss due to conduction from hot end to cold tip can be minimized. The etched channels can be hermetically sealed by fusion bonding another glass wafer on top of the channel. Also, the channel containing the high-pressure gas has to be in direct thermal contact with the low-pressure gas channel to create a CFHX. To increase the effectiveness of the CFHX, a geometry that results in a high enthalpy exchange between the two channels, is needed. In general, this means that the heat-exchange surface between the channels has to be maximized. Two rectangular channels on top of each other form in this respect a convenient configuration, see figure 2.7. This configuration can be constructed by bonding another wafer, also containing flow channels, on top of the two-wafer-stack which contains the earlier mentioned flow channel. The channels are separated by a very thin wafer, minimizing the thermal resistance. The actual dimensions of the channel's cross-sectional area and its length and thus cross-sectional area and length of the CFHX, will be determined in section 3.5 via an optimization study. A small cross-sectional area of the cold stage is desired to minimize heat conduction losses. In other words, the used wafers have to be as

thin as possible. A shallow slit with a very high flow resistance can be used to realize the Joule-Thomson restriction. The pressure drop of 74 bar stands over this restriction which results in the needed mass flow of 1 mg·s^{-1}, as was described in section 1.2. A BHF wet etch process can be used, to very accurately manufacture the slit, since its dimensions are crucial. To reduce the chance of clogging of this restriction, a relatively wide and shallow restriction geometry is chosen. A relatively large open space inside the cold-stage tip can serve as an evaporator. The evaporator serves as a buffer to store liquid nitrogen. To create the evaporator space, the powder-blast process will be used since the volume is relatively large and the smoothness of the walls is not that crucial. The gas in- and outlet are holes which will have to penetrate the entire wafer. Again powder blasting is the most suitable process to create these structures.

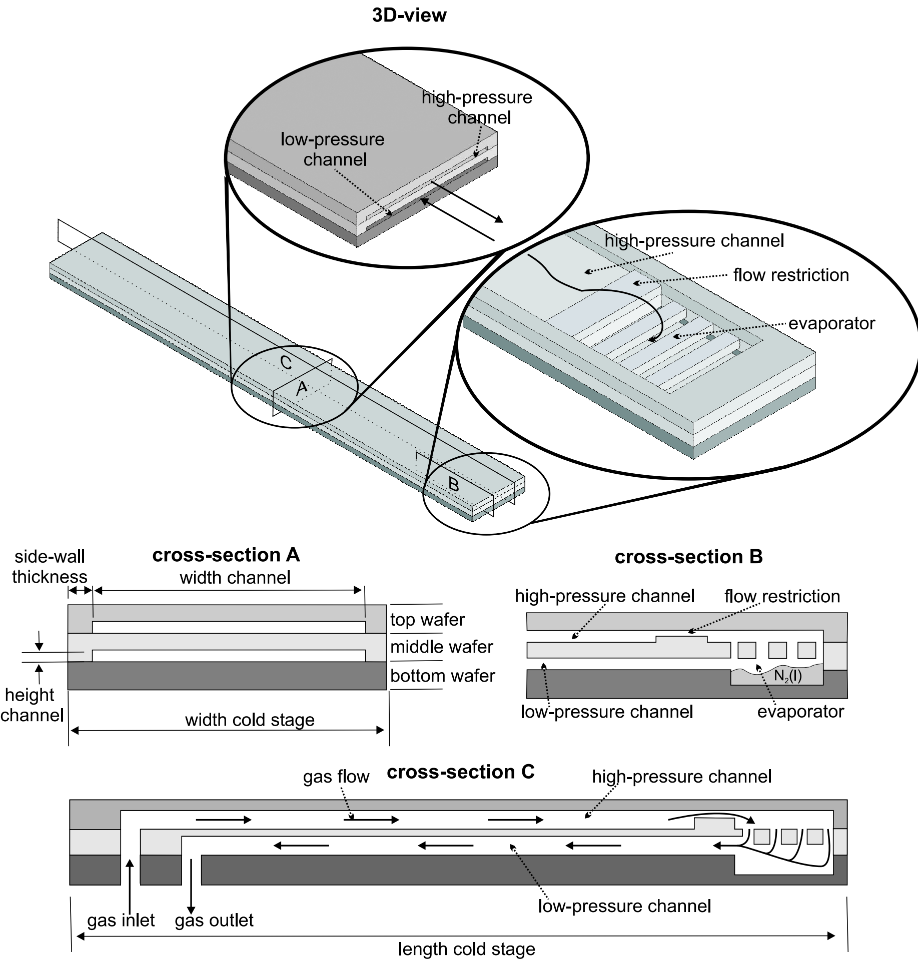

Figure 2.7: Basic design of the micro cold stage.

2.4 Conclusions

MEMS fabrication techniques seem highly suitable for the construction of JT cooler parts in micro dimensions. Different techniques will be used for the fabrication of the micro channels, holes and slits. A basic micro cooler design is defined, taking the constraints due to technology into account. The high fabrication accuracy and possibility of batch processing open the opportunity to mass produce the micro cold stages with predictable specifications. Glass is chosen as the construction material because of its low thermal conductivity and compatibility with available MEMS technology and knowledge. More specific, D263T (a borosilicate glass) is used by Micronit [10] as the construction material to fabricate the cold stages.

References

[1] Corning. Koolhovenlaan 12, NL-1119 NE Schiphol-Rijk, The Netherlands, http://www.corning.com.

[2] Schott. 555 Taxter Road, Elmsford, NY 10523, USA, http://www.us.schott.com/.

[3] Cryocomp, version 3.01. Horizon Techonologies, http://www.htess.com/cryocomp.htm.

[4] Byung-Ho Jo, L. van Lerberghe, K. Motsegood, and D. Beebe. Three-Dimensional Micro-Channel Fabrication in Polydimethylsiloxane (PDMS) Elastomer. *Journal of Microelectromechanical systems*, 9(1):76–81, 2000.

[5] Cheng Luo, Fang Meng, Xinchuan Liu, and Yiyun Guo. Reinforcement of a PDMS master using an oxide-coated silicon plate. *Microelectronics Journal*, 37(1):5–11, 2006.

[6] R. Le Harzica et al. Pulse width and energy influence on laser micromachining of metals in a range of 100 fs to 5 ps. *Applied Surface Science*, 249:322–331, 2005.

[7] L. Torrisi and D. Margarone. Investigations on pulsed laser ablation of Sn at 1064nm wavelength. *Plasma Sources Sci. Technol.*, 15:635–641, 2006.

[8] Meng-Hua Yen et al. Rapid cell-patterning and microfluidic chip fabrication by crack-free CO2 laser ablation on glass. *J. Micromech. Microeng.*, 16:1143–1153, 2006.

[9] K. Zimmer, A. Braun, and R Bohme. Etching of fused silica and glass with excimer laser 351 nm. *Applied Surface Science*, 208-209:199–204, 2003.

[10] Micronit Microfluidics BV. Hengelosestraat 705, 7521 PA Enschede, The Netherlands, http://www.micronit.com/.

[11] M. Elwenspoek and H. Jansen. *Silicon Micromachining*. Cambridge University Press, 1998. ISBN 0-521-59054-X.

[12] M. Madou. *Fundamentals of microfabrication*. CRC Press, Boca Raton, USA, 1997.

[13] J. Burger. *Cryogenic microcooling, A micromachined cold stage operating with a sorption compressor in a vapor compression cycle*. PhD thesis, University of Twente, 2001.

[14] C. Iliescu, F.E.H. Tay, and J. Miaoc. Strategies in deep wet etching of Pyrex glass. *Sensors and actuators A*, 2006.

[15] V.K. Rathi, M. Gupta, and O.P. Agnihotri. The dependence of etch rate of photo-CVD silicon nitride films on NH_4F content in buffered HF. *Microelectronics Journal*, 26:563–567, 1995.

[16] H. Wensink and M. C. Elwenspoek. Reduction of sidewall inclination and blast lag of powder blasted channels. *Sensors and Actuators A: Physical*, 102:157–164, December 2002.

[17] H. Wensink. *Fabrication of microstructures by powder blasting*. PhD thesis, University of Twente, 2002.

[18] H. Wensink, J. W. Berenschot H. V. Jansen, and M. C. Elwenspoek. Mask materials for powder blasting. *J. Micromech. Microeng.*, 10:175–180, 2000.

[19] A. Pawlowski, A. Sayah, and M. Gijs. Accurate masking technology for high-resolution powder blasting. *J. Micromech. Microeng.*, 15:s60–s64, 2005.

[20] H. Wensink, S. Schlautmann, M. H. Goedbloed, and M. C. Elwenspoek. Fine tuning the roughness of powder blasted surfaces. *J. Micromech. Microeng.*, 12:616–620, 2002.

[21] Wu Peiyi and W. A. Little. Measurement of the heat transfer characteristics of gas flow in fine channel heat exchangers used for microminiature refrigerators. *Cryogenics*, 24:415–420, 1984.

[22] Wu Peiyi and W. A. Little. Measurement of friction factors for the flow of gases in very fine channels used for microminiature Joule-Thomson refrigerators. *Cryogenics*, 23:273–277, May 1983.

[23] C.K. Hsieh and K.C. Su. Thermal radiative properties of glass from 0.32 to 206 μm. *Solar Energy*, 22:37–43, 1979.

[24] A. Bendavida and P.J. Martina and L. Wieczorekb. Morphology and optical properties of gold thin films prepared by filtered arc deposition. *Thin Solid Films*, 354:169–175, 1999.

[25] M. Ohring. *Material Science of Thin Films, Deposition & Structure*. Academic Press, San Diego, USA, 2 edition, 2002. ISBN 0-12-524975-6.

[26] C. Gui. *Direct wafer bonding with chemical mechanical polishing*. PhD thesis, University of Twente, 1998.

[27] F. Pigeon, B. Biasse, and M. Zussy. Low-temperature Pyrex glass wafer direct bonding. *Electronic letters*, 31:792–793, May 1995.

[28] C. Harendt, H. Graf, B. Hofflinger, and E. Penteker. Silicon fusion bonding and its characterization. *J. Micromech. Microeng.*, 2:113–116, 1992.

[29] C. Gui and M. Elwenspoek and N. Tas and J.G.E. Gardeniers. The effect of surface roughness on direct wafer bonding. *Journal of applied physics*, 85:7448–7454, 1999.

[30] S. Mack, H. Baumann, U. Gösele, H. Werner, and R. Schlögl. Analysis of bonding-related gas enclosure in micromachined cavities sealed by silicon wafer bonding. *Journal of the Electrochemical Society*, 144:1106–1110, 1997.

[31] G. Wallis and D. I. Pomerantz. Field assisted glass-metal sealing. *Journal of Applied Physics*, 40:3946–3950, 1969.

[32] Y. Kanda and K. Matsuda and C. Murayama and J. Sugaya. The mechanism of field-assisted silicon - glass bonding. *Sensors and Actuators*, A21-A23:939–943, 1990.

[33] P. Krause, M. Sporys, E. Obermeier, K. Lange, and S. Grigull. Silicon to silicon anodic bonding using evaporated glass. *TRANSDUCERS*, 95:228–232, 1995.

[34] A. Berthold, L. Nicola, P. M. Sarro, and M. J. Vellekoop. Glass-to-glass anodic bonding with standard ic technology thin films as intermediate layers. *Sensors and Actuators A: Physical*, 82:224–228, May 2000.

[35] Jun Wei, Sharon M. L. Nai, C. K. Stephen Wong, Zheng Sun, and Loke Chong Lee. Low temperature glass-to-glass wafer bonding. *IEEE Transactions on advanced packaging*, 26:289–294, August 2003.

[36] S. Mack, H. Baumann, and U. Gösele. Gas tightness of cavities sealed by silicon wafer bonding. In *Proceedings of the 10th IEEE International Conference MEMS 1997*, pages 488–493, Nagoya, Japan, 26 - 30 Jan. 1997.

[37] J. Wei and S.M.L. Nai and C.K. Wong and L.C. Lee. Glass-to-glass anodic bonding process and electrostatic force. *Thin Solid Films*, 462:487–491, 2004.

[38] Thomas M.H. Lee et al. Detailed characterization of anodic bonding process between glass and thin-film coated silicon substrates. *Sensors and Actuators*, 86:103–107, 2000.

[39] A. Sayah, D. Solignac, T. Cueni, and M.A.M. Gijs. Development of novel low temperature bonding technologies for microchip chemical analysis applications. *Sensors and Actuators*, 84:103–108, 2000.

[40] Zhi-Xiong Xiao et al. Silicon-glass wafer bonding with silicon hydrophilic fusion bonding technology. *Sensors and Actuators*, 72:46–48, 1999.

Chapter 3

Design optimization

The counterflow heat exchanger (CFHX) is an essential element for the recuperative cooling cycle. The performance of the CFHX strongly influences the overall performance of the micro cooler. In the ideal case, a CFHX has an infinite heat conduction in radial direction (i.e. between the high- and low-pressure gas lines) and zero heat conduction in axial direction (i.e. from the hot side to the cold tip). To predict the specifications of a CFHX and, more important, the total parasitic heat load on the cold tip as a result of its non-ideal behavior, it is necessary to calculate the CFHX's temperature profile. Using this profile, the total entropy production in the CFHX can be calculated. An optimal CFHX geometry is found by minimizing the generated entropy.

3.1 Fluid dynamics

3.1.1 Reynolds number

In the design process of a CFHX, different fields of physics are of interest of which fluid dynamics and thermodynamics are the most important ones. In fluid dynamics the Reynolds number is used to calculate the ratio of inertial forces to viscous forces and can be used to determine the flow regime of a flow [1]

$$Re = \frac{\rho v_m D_h}{\mu} \tag{3.1}$$

or also often written as

$$Re = \frac{v_m D_h}{\nu} \tag{3.2}$$

where ρ is the fluid density, v_m is the mean fluid velocity, D_h is the hydraulic diameter of the flow channel, μ is the (absolute) dynamic fluid viscosity and ν is the kinematic fluid viscosity. The hydraulic diameter of a channel is defined as:

$$D_h = \frac{4A_{cross}}{O} \tag{3.3}$$

where A_{cross} is the cross sectional area of the channel and O is the perimeter. In case of a round flow channel the hydraulic diameter equals the diameter of the duct.

A flow is called laminar if the velocity profile is smooth and the motion is highly ordered. In general, this is the case for a Reynold number lower than 2300, see figure 3.1. For simple geometries (e.g. a round duct or two parallel plates) the flow profile is parabolic. For higher Reynold numbers ($Re > 6000$) the flow is called turbulent. The smooth flow is disrupted and vortices and flow fluctuations occur. For $2300 < Re < 6000$, often called a critical Reynolds number, the flow is neither laminar nor turbulent and difficult to predict. The hydraulic diameter of a flow channel of the micro cooler is ≈ 0.1 mm. For a mass flow in the system of about 1 mg$\cdot$s^{-1}, the mean velocity is about 0.1 m$\cdot$s^{-1} resulting in a Reynolds number of about 50 and therefore the flow will be laminar. If a higher mass flow is chosen, as will be done in section 3.5.4, the Reynolds number increases.

3.1.2 Pressure drop and friction factor

The pressure drop over a duct can be calculated using the formula [1]:

$$\Delta p = f \frac{l}{D_h} \frac{1}{2} \rho v_m^2 \tag{3.4}$$

If the flow is fully developed over the total length l, this equation holds for both laminar and turbulent flows. In formula 3.4, f is the so-called Darcy-Weisbach friction factor [1]. For fully developed laminar flow (the flow in the micro cooler channel is expected to be laminar at all time) f depends on a geometric factor C and Reynolds. It can be written as:

$$f = \frac{C}{Re} \tag{3.5}$$

The value of C depends on the geometry of the duct, see figure 3.2. For a round tube C equals 64 and for a rectangular shape $C = 96$.

If the flow is fully developed and turbulent, Bejan [1] states the following empirical formulas for the friction factor of a smooth tube:

$$f \cong 0.316 \cdot Re^{-\frac{1}{4}} \quad 2 \cdot 10^3 < Re < 2 \cdot 10^4 \tag{3.6}$$

For higher Reynolds numbers, the friction factor is given by:

$$f \cong 0.184 \cdot Re^{-\frac{1}{5}} \quad 2 \cdot 10^4 < Re < 10^6 \tag{3.7}$$

The relation between the friction factor, the Reynolds number and the relative roughness is drawn in figure 3.1, which is known as Moody's chart [2]. The relative surface roughness of the duct is represented in this graph by the dimensionless ratio $\frac{k_s}{D_h}$, where k_s is the so-called Nikuradse "sand roughness" size [3] which can be experimentally determined. A higher roughness will result in a higher friction factor and pressure drop. Some values of k_s for different pipe surfaces are given in figure 3.1.

Whether this Moody chart is still valid for etched micro channels was investigated by Wu and Little [4]. For micro channels the relative roughness increases because of the small dimensions of the channel. Also the roughness strongly varies depending on the used MEMS processes. If wet etching is used to fabricate the micro channels, the relative

[1] The Darcy-Weisbach friction factor should not be confused with the Fanning friction factor which is also often used in literature. The Fanning friction factor is four times smaller than the Darcy-Weisbach factor.

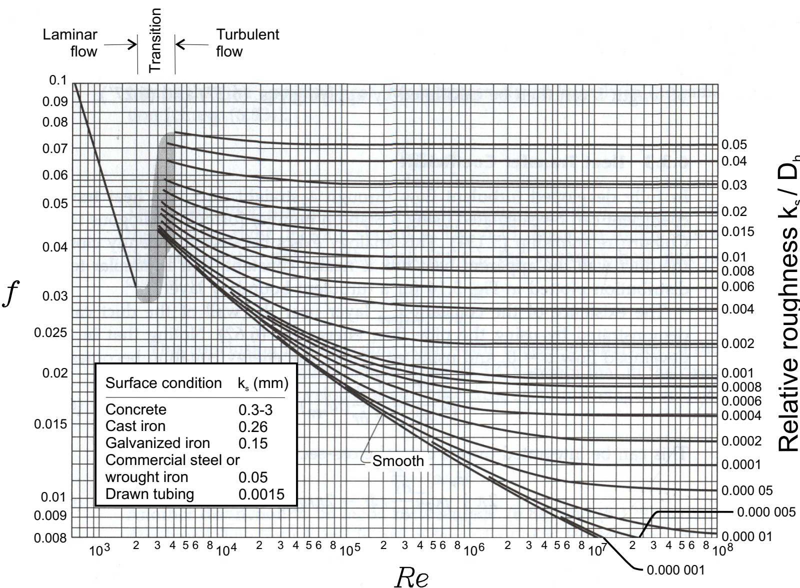

Figure 3.1: Friction factor for fully developed laminar and turbulent flow in a pipe, drawing taken from Moody [2].

roughness will be much smaller than powder blasted channels. Wu and Little found that the friction factor for wet etched channels is nearly in agreement with that for smooth pipes shown in the Moody chart. Channels formed by powder blasting showed a 3 to 3.5 times higher friction factor in the laminar zone and 4 to 5 times higher in the turbulence zone, than if they are compared to a smooth pipe. Also, the transition from laminar to turbulent flow seems to occur earlier ($Re_{trans.} \simeq 400$ [4, 5]). The relative roughness (k_s/D_h) of the powder blasted channels was estimated in the range of $0.2 - 0.3$. Since we are using only wet chemical etching to construct the flow channels of the micro cold stage, we expect that the relation between the friction factor and the Reynolds number will agree with the Moody chart shown in figure 3.1.

3.2 Thermodynamics

3.2.1 Convective heat transfer

Prandtl number

In the previous sections we have seen that the Reynolds number indicates the flow regime and the friction factor can be used to calculate the pressure drop over a duct. To calculate the heat transfer characteristics of a flow channel two other dimensionless number are commonly used. The first is the Prandtl number which is a parameter that characterizes the regime of convection. It gives the ratio of momentum diffusivity, represented by the ratio of kinematic viscosity ν and thermal diffusivity (α) of a fluid:

$$Pr = \frac{\nu}{\alpha} \tag{3.8}$$

It also can be defined as

$$Pr = \frac{c_p \mu}{\lambda} \tag{3.9}$$

where c_p is the specific heat at constant pressure, μ the dynamic viscosity (with $\mu = \nu \cdot \rho$) , and λ the thermal conductivity. When $Pr = 1$, the fluid velocity boundary layer thickness coincide with the fluid temperature boundary layer thickness. When Pr is small, it means that the thickness of the thermal boundary layer is much larger than the velocity boundary layer. It can be concluded from equation 3.9 that Prandtl depends on the kind of fluid and also is temperature and pressure dependent. For example, Prandtl for nitrogen at 80 bar and 300 K is 0.74, if the temperature is lowered to 100 K Prandtl is 1.64.

Nusselt number and Stanton number

The Nusselt number gives the ratio of the convective heat transfer to the heat transfer by conduction and is defined by:

$$Nu = \frac{hD_h}{\lambda} \tag{3.10}$$

where h is the local heat transfer coefficient and λ the heat conduction coefficient of the fluid. A large Nusselt number means very efficient heat transfer by convection (e.g. turbulent pipe flow yields $Nu = 10^2 - 10^3$). For fully developed laminar flow, Nusselt can be determined analytically and depends on the cross section shape of the duct and the assumed boundary conditions [6]. Fig 3.2 gives Nusselt for different geometries[1, 7]. Marco and Han [8] stated the Nusselt number for uniform heat flux for a rectangular channel as a function of the channel aspect ratio ($\chi = \frac{height}{width}$):

$$Nu = 8.235(1 - 2.042\chi + 3.0853\chi^2 - 2.4765\chi^3 + 1.0578\chi^4 - 0.1861\chi^5) \tag{3.11}$$

According to this equation, the Nusselt number increases with a decrease in the aspect ratio. Different groups have investigated the influence of the channel dimensions and geometry on the characteristics of heat transfer [5, 9, 10]. Peiyi and Little [11] also report a surface roughness dependence in contrast to Choi et al. [12]. According to Peiyi and Little, the roughened micro channels have an improved heat transfer coefficient.

Cross section shape	C	Nusselt
Triangle	53.2	3
Square	56.8	3.63
Circle	64	4.364
Rectangle a × 2a	62.4	4.12
Rectangle a × 4a	73.2	5.35
Rectangle a × 8a	84	6.49
Rectangle a × ∞·a	96	8.235

Figure 3.2: Geometric constants C and Nusselt numbers for hydrodynamically and thermally fully developed duct flows [1, 7].

The channels of the presented cold stage will be wet etched and therefore the surface roughness will be considerably smaller than the channel depth. It is therefore expected that the channel roughness will have no significant influence on the heat transfer coefficient or Nusselt number. As a safe estimate of the Nusselt number of a micro channel, equation 3.11 will be used.

The relation between Reynolds, Prandtl and Nusselt is known as the Stanton Number:

$$St = \frac{Nu}{Re \cdot Pr} \tag{3.12}$$

Overall heat transfer coefficient

The local heat transfer coefficient h, mentioned in equation 3.10, can be used to determine the heat flow between a fluid and a solid as a result of a temperature difference between the two. This heat flow $\dot{Q}$ becomes:

$$\dot{Q} = hA\left(\bar{T_h} - T_c\right) \tag{3.13}$$

where A is the heat exchange area, T_c the wall temperature and $\bar{T_h}$ an average fluid temperature taking the flow profile and the temperature gradient into account:

$$\dot{m}\bar{T_h} = \int \rho v(A)T(A)dA \tag{3.14}$$

In a counterflow heat exchanger, heat is exchanged between two fluids via a solid wall, dividing the fluids, see figure 3.3. It is often the case that only the temperatures of the bulk of the fluids are known and not the intermediate temperature of the solid material.

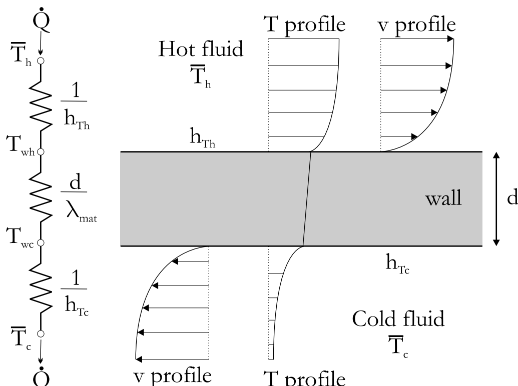

Figure 3.3: Heat exchange between two fluid flows through a wall.

To calculate the heat flux from the hot fluid to the cold fluid the overall heat transfer coefficient can be used:

$$\dot{Q} = UA_{HX}\left(\bar{T}_h - \bar{T}_c\right) \tag{3.15}$$

where A_{HX} is the heat exchange surface area, $\bar{T}_h$ the hot fluid temperature, $\bar{T}_c$ the cold fluid temperature and U the overall heat transfer coefficient equal to:

$$\frac{1}{U} = \frac{1}{h_{T_h}} + \frac{d}{\lambda_{mat}} + \frac{1}{h_{T_c}} \tag{3.16}$$

The overall heat transfer coefficient determines the total heat resistance from one fluid to the other, which is analogous to an electrical resistance calculation, see figure 3.3. It combines the three resistances, two convection and one conduction resistance into one overall heat resistance. Using equation 3.10, it can be seen that the two local heat transfer coefficients h in equation 3.16 are both pressure and temperature dependent through λ and also depend on the CFHX geometry. Therefore, also the overall heat transfer coefficient U depends on fluid properties and CFHX geometry.

3.2.2 Parasitic heat losses

The net cooling power of the micro cooler will be reduced by parasitic heat losses. These losses are treated in this section. To attain maximum net cooling power, these parasitic heat losses should be reduced as much as possible as will be discussed in section 3.5.

Conduction

If there is a temperature difference across an object, heat will flow from the high temperature to the low temperature area. In case of the micro cooler this means heat will flow from the hot side to the cold tip through the CFHX's body, which of course is unwanted.

The amount of heat flowing ($P_{conduction}$) can be expressed as [1]:

$$P_{conduction} = \lambda_{mat} A \frac{dT}{dx} \tag{3.17}$$

As can be seen from this equation, heat flow can be reduced by decreasing the heat conduction coefficient of the object's material (λ_{mat}), decreasing the cross-sectional area A and/or decreasing the temperature gradient $\frac{dT}{dx}$ by for example increasing the length. It is now obvious why in section 2.1 glass was chosen as fabrication material. The thermal conductivity of glass typically lies around 1 W·m^{-1}·K^{-1}, in comparison for silicon this value is about 1000 W·m^{-1}·K^{-1}, see figure 2.1. The optimization of the CFHX geometry, i.e. cross-sectional area and length will be discussed in section 3.5.

Radiation

Two objects which differ in temperature can exchange heat through radiation even when they are separated by absolute vacuum. For a two-surface enclosure, as is depicted in figure 3.4, the amount of heat flow ($P_{radiation}$) is described by [1]:

$$P_{radiation} = \frac{\sigma_b A_1 (T_2^4 - T_1^4)}{\frac{1}{\epsilon_1} + \frac{A_1}{A_2}(\frac{1}{\epsilon_2} - 1)} \tag{3.18}$$

where σ_b is Boltzmann's constant, A_1 and A_2 respectively inner and outer surface, ϵ_1 and ϵ_2 inner and outer emissivity. This equation can be simplified if it is used to calculate the parasitic heat loss due to radiation in the micro cooler setup. In this case, the total hemispherical emissivity of the surroundings (the vacuum chamber) will be very high and assumed to be a black body surface: $\epsilon_2 = 1$. Because the emissivity of glass is very large (ϵ is 0.8 to 0.95 [13]) the cooler's surface is covered with a thin gold layer to maximize reflectivity. Emissivity of a such a smooth gold surface is about $\epsilon = 0.02$ [14]. Also the surface of the surroundings will be much larger than the surface of the micro cooler ($A_1 << A_2$). Knowing this, equation 3.18 becomes:

$$P_{radiation} = \epsilon_1 \sigma_b A_1 (T_2^4 - T_1^4) \tag{3.19}$$

where ϵ_1 and A_1 are respectively the cooler's emissivity and surface area and T_2 and T_1 the temperature of the surroundings and that of the micro cooler.

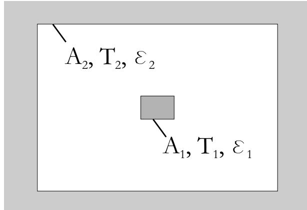

Figure 3.4: Surface enclosed by another surface.

Molecular flow conduction

To minimize heat flux through convection via the surrounding gas, the micro cooler will operate in a vacuum environment. However, even though the pressure is very low, a parasitic heat loss may still occur. To determine this loss, the so-called Knudsen number can be used [15]:

$$Kn = \frac{\Lambda_{gas}}{d} \tag{3.20}$$

where Λ_{gas} is the mean free path of the gas molecules in the vacuum space and d is the characteristic length of the system. Knudsen is useful for determining the flow regime of a system. If $Kn << 1$, the gas behaves like a continuous medium and gas flow is called viscous. For $Kn >> 1$, the gas behaves like a system of separate molecules without interaction. In this case, free molecular flow can be assumed, meaning the chance of a gas molecule hitting another gas molecule is much smaller than the chance of hitting one of the two walls. Knudsen decreases for increasing pressure. At a temperature of 273 K the mean free path of air is [16]:

$$\Lambda_{air} = \frac{6.7 \cdot 10^{-3}}{p} \left[\frac{\mathrm{m \cdot Pa}}{\mathrm{Pa}}\right] \tag{3.21}$$

with p the gas pressure.

In the free molecular flow regime, the heat flux due to molecular flow conduction ($P_{mol.cond}$) is determined by:

$$P_{mol.cond} = \overline{\alpha}\lambda_m pA(T_h - T_c) \tag{3.22}$$

where $\overline{\alpha}$ is the average thermal accommodation coefficient, λ_m is the molecular heat conduction coefficient, p the pressure and A the heat exchange surface. The thermal accommodation coefficient is a factor between 0 and 1 and indicates to what degree the incident gas molecule adopts the temperature of the wall it hits. If $\alpha = 1$, there is full thermal accommodation, and the gas molecule has the same temperature as the wall it is leaving from. Generally α increases when the gas molecules are moving slower, as they spend more time in the neighborhood of the wall and the degree of accommodation will be higher. Hence α increases for decreasing temperature and increasing mass. Furthermore, α depends strongly on the surface condition; the rougher the surface, the higher the thermal accommodation coefficient. This means that a clean and polished surface will have a smaller α than a dirty rough surface. The average thermal accommodation coefficient is estimated using the following relation:

$$\overline{\alpha} = \frac{\alpha_1\alpha_2}{\alpha_1 + \alpha_1 - \alpha_1\alpha_2} \tag{3.23}$$

where α_1 is the thermal accommodation coefficient of the object surrounded by the vacuum enclosure with thermal accommodation coefficient α_2.

In the measurement setup discussed in section 6.1, the pressure inside the vacuum chamber is typically $1 \cdot 10^{-5}$ mbar. The characteristic length of the system is about 3 cm meaning Knudsen has a much higher value than 1, thus the flow is in the molecular regime. Using equation 3.22, it can be seen that molecular flow conduction is extremely low in this case. Therefore, in all static CFHX models which are discussed in section 3.3, this parasitic heat loss is neglected. However, if the micro cooler is to be integrated with

a wafer level vacuum package, as will be discussed in chapter 7 this loss term may be of concern.

3.3 Static models of a CFHX

As was mentioned in the introduction of this chapter, it is necessary to calculate the CFHX's temperature profile in order to predict the specifications of a CFHX and more importantly the parasitic heat load on the cold tip as a result of its non-ideal behavior. A number of calculation methods to determine the temperature profile were investigated and compared. These methods are: the Log Mean Temperature Difference (LMTD) method, the enthalpy (Δh) method and the Bahnke-Howard (BH) method. The methods differ in solving method and the required in- and resulting output parameters, see table 3.1. It is important to mention that in the first two methods, heat flow through the material in longitudinal direction and radiation on the CFHX outer surface is neglected in determining the temperature profile. The three methods are applied to the CFHX geometry of section 2.3 and discussed in the following sections. In all three described models, gas properties vary under changing pressure and temperature, see appendix A.1, which is taken into account in the model.

Table 3.1: In- and output parameters of three methods to evaluate the CFHX temperature profile.

Parameter	LMTD	Δh	BH
$T_{pH,in}$ and $T_{pL,in}$	in	in	in
Gas properties	in	in	in
Mass flow ($\dot{m}$)	in	in	in
Material properties	in	in	in
Channel geometry	in	in	in
CFHX length	in	out	in
CFHX effectiveness	out	in	-
Temperature profile	out	out	out
Parasitic heat load	via $\frac{dT}{dl}$	via $\frac{dT}{dl}$	out

3.3.1 LMTD method

In the Log Mean Temperature Difference (LMTD) method, the CFHX is divided into N elements of a constant length ($\Delta L = L/N$). Each element is divided in 2 sub-elements: a high-pressure gas element and a low-pressure gas element, see figure 3.5. Within a sub-element, pressure and temperature are assumed constant as well as the different properties of the gas. In the LMTD model, it is assumed that all heat flux out of the warm high-pressure gas is absorbed by the cold low-pressure gas. Heat conduction through the CFHX material in longitudinal direction is neglected. Since the temperature profile over a single element (and over the total CFHX length) is non-linear, the log mean temperature difference [1, 17] is used. The heat flux per element (i) is, analogous to equation 3.15, defined by:

$$\dot{Q}_{LMTD,i} = U_i A_{HX} \Delta T_{LMTD,i} \tag{3.24}$$

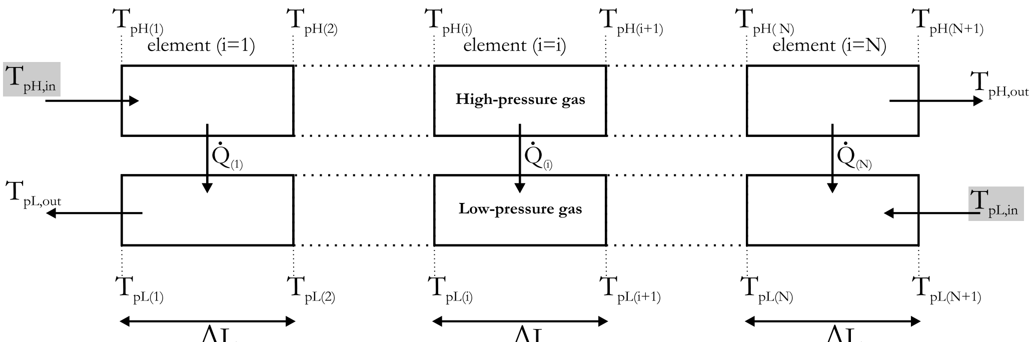

Figure 3.5: Schematic of the LMTD solution method. Highlighted temperatures are fixed and serve as boundary conditions.

Where U_i is the local overall heat transfer coefficient, A_{HX} the heat exchange surface of an element and $\Delta T_{LMTD,i}$ is the log mean temperature difference of an element (i):

$$\Delta T_{LMTD,i} = \frac{\Delta T_{II} - \Delta T_I}{\ln\left(\Delta T_{II}/\Delta T_I\right)} \tag{3.25}$$

With,

$$\Delta T_I = T_{pH(i)} - T_{pL(i)} \tag{3.26}$$

and

$$\Delta T_{II} = T_{pH(i+1)} - T_{pL(i+1)} \tag{3.27}$$

In a first step, an estimate is made of the high-pressure outflow temperature $T_{pH(N+1)}$. Using this estimated value, the gas properties ($c_{p(N)}$, $\mu_{(N)}$, $\rho_{(N)}$ and $\lambda_{(N)}$) of element N are determined. Knowing the channel geometry, thus its hydraulic diameter and Nusselt number, the convective heat transfer coefficient for each sub-element of element N can be determined using equation 3.10. Using equation 3.16 the local overall heat transfer coefficient is calculated. The heat transferred in an element equals the change in internal energy of the gas of both the high- and the low-pressure side. The LMTD method assumes that all enthalpy released by the warm high-pressure gas is absorbed by the cold low-pressure gas. This way the change in temperature from $N+1$ to N can be calculated:

$$\dot{m}c_{p(N)}\left(T_{pH(N+1)} - T_{pH(N)}\right) = U_{(N)}A_{HX}\left(T_{pH(N+1)} - T_{pL(N+1)}\right) \tag{3.28}$$

which is rewritten into:

$$T_{pH(N)} = T_{pH(N+1)} - \frac{U_{(N)}A_{HX}\left(T_{pH(N+1)} - T_{pL(N+1)}\right)}{\dot{m}c_{p(N)}} \tag{3.29}$$

where A_{HX} is the width of the channel times ΔL. The same calculation holds for the low-pressure sub-element. When $T_{pH(N)}$ and $T_{pL(N)}$ are determined, the next element $(N-1)$ can be calculated using these values. All other temperatures are calculated in the same way. Finally, temperatures $T_{pH(1)}$ and $T_{pL(1)}$ are found. Obviously there will be a difference between $T_{pH(1)}$ and the constraint $T_{pH,in} = 300$ K. A new estimate, depending

on this difference, of $T_{pH(n+1)}$ is made and the total calculation is done again but now using the log mean temperature difference in an element:

$$T_{pH(i)} = T_{pH(i+1)} - \frac{U_{(i)} A_{HX} \Delta T_{LMTD,i}}{\dot{m} c_{p(i)}} \tag{3.30}$$

This iteration process continues until $T_{pH,in} - T_{pH(1)} < 10^{-4}$ K. The parasitic heat loss and thus the net cooling power for a certain CFHX geometry can be determined using the calculated temperature profile in combination with the equations from section 3.2.2.

3.3.2 Δh method

In the enthalpy (Δh) method, the CFHX is not divided into elements of a constant length but in N elements of constant enthalpy exchange (Δh). Again each element is divided in 2 sub-elements: a high-pressure gas element and a low-pressure gas element, see figure 3.6.

Just like in the LMTD method, the Δh method assumes that all enthalpy released by the warm high-pressure gas is absorbed by the cold low-pressure gas [18]. Again, heat conduction through the CFHX material in longitudinal direction is neglected. For a perfect operating CFHX, $\Delta h_{23} = -\Delta h_{51}$, see bottom plot of appendix A.2. In the ideal case, the low-pressure gas has absorbed the maximum possible amount of enthalpy resulting in a low-pressure outflow temperature of $T_{pL,out} = T_{pH,in}$, see figure 3.7. Assuming that only gas is flowing through the CFHX we can state that:

$$\Delta h_{max} = h_{pL,300K} - h_{pL,96K} \tag{3.31}$$

This implies that in the ideal case, the high-pressure gas' outflow temperature ($T_{pH,out}$) has a theoretical minimum which is significantly higher than the low-pressure gas' inflow temperature. Knowing that $\Delta h_{pL} = \Delta h_{pH} = \Delta h_{max}$, the enthalpy at the high-pressure gas' outflow becomes:

$$h_{pH,out} = h_{pH,300K} - \Delta h_{max} \tag{3.32}$$

which can be used to determine the high-pressure gas' outflow temperature: $T_{pH,out} = T_{pH}(h_{pH,out})$. This difference in temperature is a result of the difference in c_p of the gas

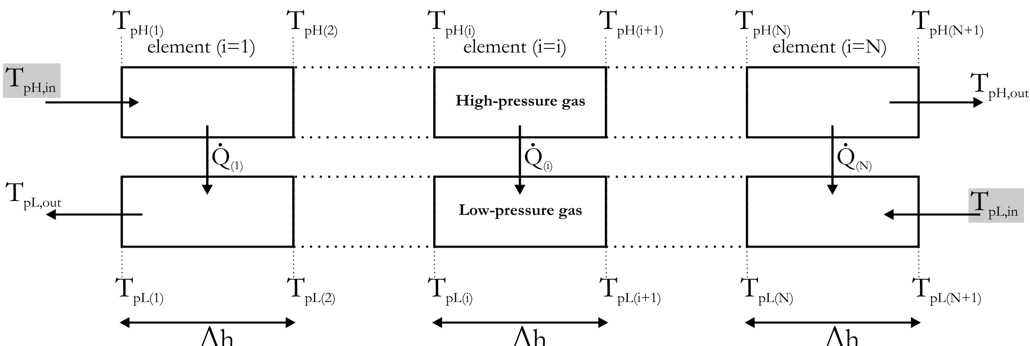

Figure 3.6: Schematic of the Δh solution method. Highlighted temperatures are fixed and serve as boundary conditions.

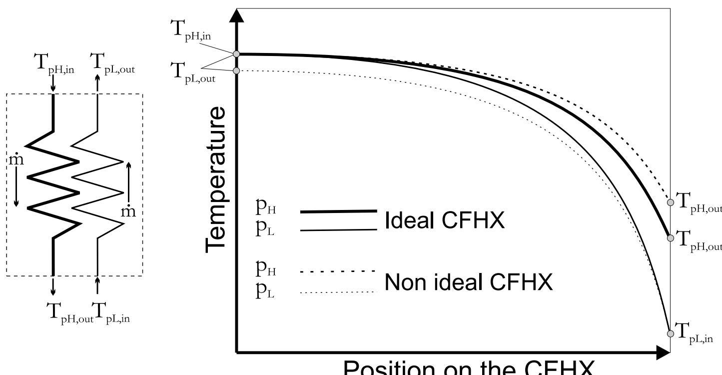

Figure 3.7: Schematic of the temperature profile of a ideal and non-ideal CFHX.

at different pressure, see A.1. For the micro cooler cycle this would mean that the high-pressure outflow temperature, according to this model, can not be lower than 153.36 K, see appendix A.2. In the non-ideal case, the exchanged enthalpy will be less than Δh_{max} ($T_{pL,out} \neq 300$ K), see figure 3.7.

The ratio between the actual exchanged enthalpy and the maximum enthalpy Δh_{max} is called the effectiveness or efficiency of a CFHX:

$$\eta_{CFHX} = \frac{\Delta h_{exchanged}}{\Delta h_{max}} \tag{3.33}$$

In the Δh method, the targetted effectiveness is an input parameter. When an effectiveness is chosen, the CFHX is divided into N elements of constant enthalpy exchange:

$$\Delta h = \frac{\eta_{CFHX} \cdot \Delta h_{max}}{N} \tag{3.34}$$

The Δh method needs as input parameters: the material and gas properties, the channel geometry, the high- and low-pressure gas inflow temperature and the CFHX effectiveness, see table 3.1. The temperature profile (in terms of dT/dh) can be determined using the known enthalpy value of the different elements i. Like equation 3.28, the heat transferred in an element equals the change in internal energy of the gas:

$$\dot{m}dh = U_i \Delta T_i w dx_i \tag{3.35}$$

The length of element i (dx_i) that is required for the enthalpy exchange can thus be determined by:

$$dx_i = \frac{\dot{m}dh}{U_i \Delta T_i w} \tag{3.36}$$

where U_i is the overall heat transfer coefficient of element i, ΔT_i is the temperature difference between the high- and low-pressure channel of element i and w is the width of the channel. Obviously, the summation of all elements dx_i gives the total length of the CFHX. Again, this calculated temperature profile can be used in combination with the equations from section 3.2.2 to determine the parasitic heat loss for a certain CFHX geometry.

3.3.3 Bahnke-Howard method

Just like the LMTD-method, the CFHX is divided into N elements of a constant length. However, in the BH-model these elements are each divided in *three* sub-elements: a high-pressure gas element, a material element and a low-pressure gas element. Conduction in longitudinal direction and radiation on the CFHX outer surface are now taken into account. Figure 3.8 gives a schematic of all elements with the energy flows in and out of the elements. Again all gas- and material properties vary under changing pressure and temperature, which is taken into account in the model. Within a sub-element, pressure and temperature are assumed constant as well as the different properties of the gas and material. The temperatures in figure 3.8 that are highlighted are fixed and thus serve as boundary conditions for the model. In the case of the micro cooler this results in the following boundary conditions:

- $T_{pH(1)}$ equals the high-pressure gas in-flow temperature: $T_{pH,in} = 300$ K
- $T_{m(1)}$ is the temperature of the wall at the hot end: 300 K
- $T_{m(N+1)}$ is the temperature of the wall at the cold end: 96 K
- $T_{pL(N+1)}$ equals the low-pressure gas in-flow temperature: $T_{pL,in} = 96$ K

For each sub-element a energy balance equation for the different energy flows (i.e. the gas, longitudinal conduction, wall transition and radiation) can be formulated.

$$\Sigma\dot{Q} + \Sigma\dot{H} = 0 \tag{3.37}$$

Doing so, the model is configured as a system of equations with $3N$ energy equations and $3N$ unknown variables which are $(3N-1)$ temperatures and one heat flow $\dot{Q}_{c(N+1)}$ which is the actual parasitic heat load on the cold tip. The system can be written as a matrix formula: $C = M * U$, with C the boundary conditions of the system, M the

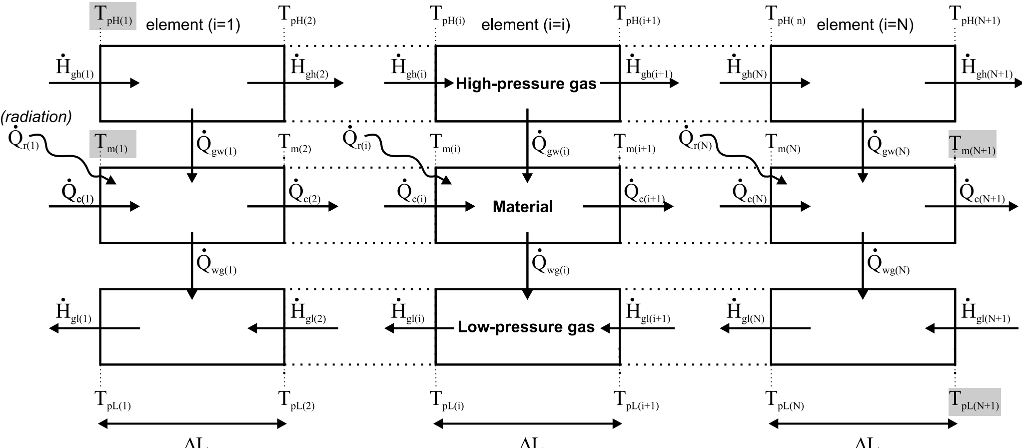

Figure 3.8: Schematic of the Bahnke-Howard model. Highlighted temperatures are fixed and serve as boundary conditions. $\dot{H}_{gh}$ and $\dot{H}_{gl}$ respectively refer to the energy flow carried by the high-pressure and low-pressure gas.

design matrix and U the unknown variables. This system of equations is solved using Matlab [19].

3.3.4 Static model comparison

In principle all described models can be used to calculate the temperature profile of a CFHX and with it the total parasitic heat load on the cold tip. As can be seen in table 3.1 there is some difference between the required in- and resulting output parameters for these models. The choice of what model should be used depends on the available input parameters and/or desired output parameters and the validity of a model for a certain CFHX configuration.

As was mentioned before, in both the LMTD- and the Δh-model, longitudinal heat conduction is neglected while determining the CFHX temperature profile. For the BH-model this is not the case. The effect of this heat flow on the heat exchanger's performance was described by Kays and London [20]. To estimate if longitudinal conduction is of concern, a dimensionless parameter λ_{BH}, defined by Bahnke and Howard [21], can be used:

$$\lambda_{BH} = \frac{\lambda_m A_c}{L \cdot \dot{m} \cdot c_{p_{min}}} \tag{3.38}$$

with λ_m the heat conduction coefficient of the CFHX material, A_c the cross-sectional area of the CFHX, L the length of the CFHX, $\dot{m}$ the mass flow and $c_{p_{min}}$ the minimal specific heat capacity of the gas used in the system. Bahnke and Howard state that longitudinal conduction cannot be neglected if $\lambda_{BH} > 10^{-2}$. To illustrate the difference between the models, figure 3.9 shows the calculated temperature profiles for two different CFHX geometries using all three models. The left graph shows a CFHX with $\lambda_{BH} = 0.001$. According to Bahnke and Howard there is no need to include longitudinal heat conduction in the model. Indeed all three model give nearly the same temperature profile for this specific geometry. The right graphs shows a CFHX with $\lambda_{BH} = 0.05$. In this case longitudinal conduction should not be neglected. As the results show, there is indeed a significant difference between the calculated profile using the BH-model and

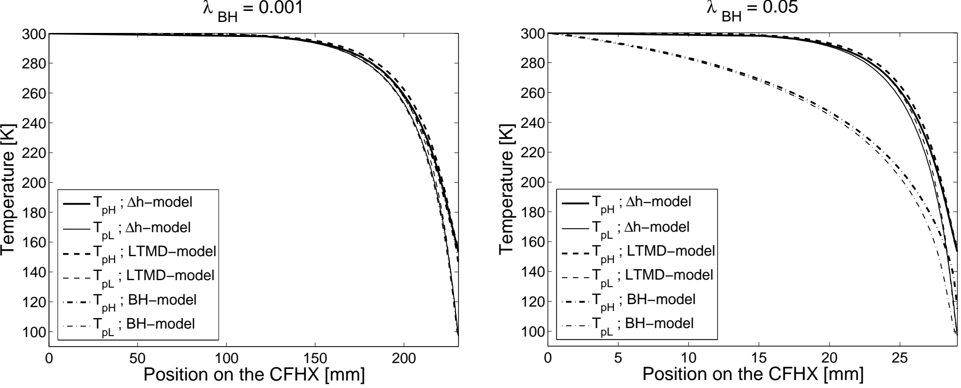

Figure 3.9: Comparison of the different static models.

the profiles found through the LMTD- and Δh-model. Due to the large difference in calculated profiles, the results in determined parasitic heat loss also differ a lot. It is seen that with increasing λ_{BH}, the CFHX temperature profile becomes more and more linear. This is due to the increasing dominance of conduction in the total parasitic heat loss.

If a rough estimate of the parameters of the micro cooler is made (i.e. $\lambda_m \approx 1$ W·m^{-1}·K^{-1}, $A_c \approx 1 \cdot 10^{-6}$ m^2, $L \approx 20 \cdot 10^{-3}$ m, $\dot{m} \approx 1 \cdot 10^{-6}$ kg·s^{-1} and $c_{p_{min}} \approx 1 \cdot 10^3$ J·kg^{-1}·K^{-1}), we can calculate that λ_{BH} is approximately 0.05. In other words, longitudinal heat conduction has to be taken into account while calculating the temperature profile. Therefore, the BH-model will be used to determine the temperature profile of the micro cold stage.

3.4 Dynamic model of a CFHX

3.4.1 Dynamic model layout

In order to simulate the development of the temperature profile of the cold stage through time, a dynamic model can be used. Just like the BH-model, in this model, the CFHX is divided into N elements of a constant length with three sub-elements, see figure 3.10, only now the evaporator is included in the model. At the start of a simulation ($t = 0$), the whole system is at ambient temperature. From this moment on, a cooling power (P_{cool}) starts cooling the system in the evaporator.

Unlike the static model, the heat capacity of the system is now of importance. In principle, when all energy flows for a CFHX element are known, the temperature change for an element (i, j) can be calculated using the equation:

$$\Delta T_{i,j} = \frac{\Sigma \dot{Q}_{i,j} + \Sigma \dot{H}_{i,j}}{m_{i,j} c_{p,i,j}} \Delta t \tag{3.39}$$

where $\Sigma \dot{Q}_{i,j} + \Sigma \dot{H}_{i,j}$ is the sum of all energy flows entering and leaving a sub-element. Here i refers to the element and j to the layer within the element, see figure 3.10. Furthermore, m is the element's mass, c_p its specific heat capacity and Δt the time step used.

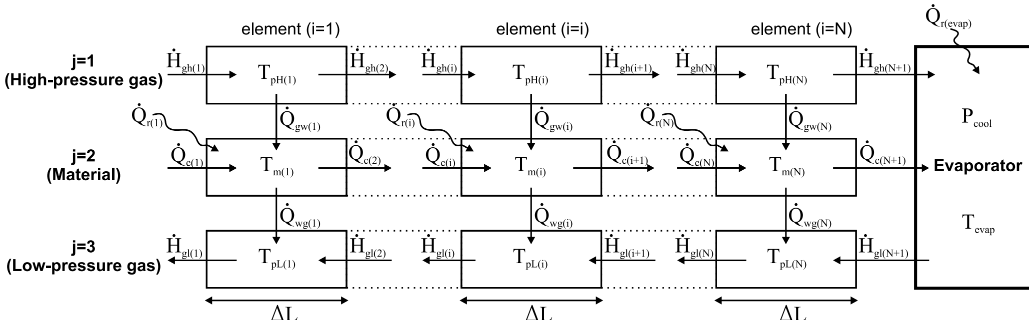

Figure 3.10: Schematic of the dynamic model.

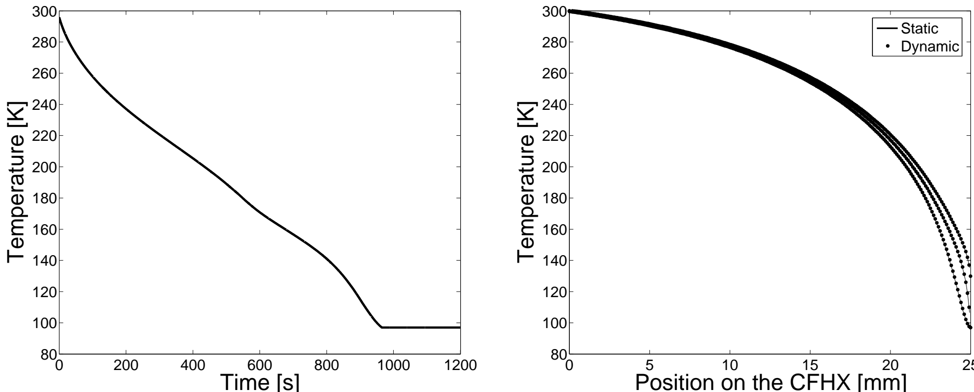

Figure 3.11: Left: the calculated temperature of the evaporator through time. Right: comparison between dynamic and static model. The top line in the graph is the temperature profile of the high-pressure gas, the middle of the material and the bottom line of the low-pressure gas.

The temperature change of the evaporator element in a time span Δt is defined as:

$$\Delta T_{evap} = \frac{\Sigma \dot{Q}_{evap} + \Sigma \dot{H}_{evap}}{C_{evap}} \Delta t \tag{3.40}$$

where $\Sigma \dot{Q}_{evap} + \Sigma \dot{H}_{evap}$ is the sum of all energy flows entering and leaving the evaporator element. This includes the gross cooling power $P_{cool} = \dot{m}\Delta h_{cool}$ which equals $\dot{m}\left(h(p_L, T_{pL(N)} - h(p_H, T_{pH(N)})\right)$. When the temperature change for every element is known and thereby the new temperature profiles at t_k, the calculation will start again, calculating the temperature profiles for the next time step, $t_{k+1} = t_k + \Delta t$. By storing the solutions for all t_k, the temperature development in time is known for each element.

The dynamic model can be used to calculate the cool-down time of a cold stage. Figure 3.11 shows the calculated evaporator temperature versus time. The cooler dimensions used are: 25 mm x 2.2 mm x 0.5 mm.

If the flow is viscous, laminar and isothermal, the mass flow ($\dot{m}$) through the restriction can be described by [1]:

$$\dot{m}(T) = \frac{1}{12} \frac{wh^3}{l} \int_{p_L}^{p_H} \frac{\rho(p,T)}{\mu(p,T)} dp \tag{3.41}$$

where w is the width, h the height and l the length of the restriction, p_L and p_H are the low and high pressure respectively, $\rho(p,T)$ is the density and $\mu(p,T)$ the viscosity which both are a function of pressure and temperature. It is assumed that the temperature of the restriction equals the temperature of the evaporator. The mass flow through the system is thus temperature dependent and is calculated using T_{evap}. Also in this calculations there have been made some adjustments to the model to compensate for heat losses induced by the measurement setup as will be explained in section 6.2.3.

In this example the cool-down time is about 950 seconds. At the final evaporator temperature the temperature profile over the CFHX is stable ($\frac{dT_{i,j}}{dt} < 1$ mK·s^{-1}). This

profile is compared to the static profile calculated using the BH-model, see the right graph of figure 3.11. As can be seen the profiles agree very well.

3.5 Optimization study

The performance of the CFHX strongly influences the overall performance of the cryocooler, as was mentioned before. Next to the parasitic heat losses, treated in section 3.2.2, another loss in the CFHX is the pressure drop. The higher the pressure drop over the flow channels, the lower the available cooling enthalpy at the cold tip. In the design of a heat exchanger, the different loss mechanisms like pressure drop and parasitic heat flows are often treated separately [22–26]. Acceptable values for the pressure drop and total heat leakage are estimated and thus an "optimal" CFHX geometry is more or less arbitrarily chosen. However, if the different losses are all treated as a generation of entropy, they can be added in a total production of entropy within the cold stage. Figure 3.12 shows a schematic of a refrigerator. An amount of input power (P) is needed to realize a cooling power ($\dot{Q}_L$). The first law of thermodynamics states that:

$$\dot{Q}_L - \dot{Q}_H + P = 0 \tag{3.42}$$

The second law states:

$$\frac{\dot{Q}_L}{T_L} - \frac{\dot{Q}_H}{T_H} + \dot{S}_i = 0 \tag{3.43}$$

where $\dot{S}_i$ is the entropy generated in the system due to irreversibilities. Combining equations 3.42 and 3.43 gives:

$$T_H \frac{\dot{Q}_L}{T_L} - (\dot{Q}_L + P) + T_H \dot{S}_i = 0 \tag{3.44}$$

Thus the input power (P) needed to produce a cooling power ($\dot{Q}_L$) at a low tempature (T_L) is:

$$P = (\frac{T_H}{T_L} - 1)\dot{Q}_L + T_H \dot{S}_i \tag{3.45}$$

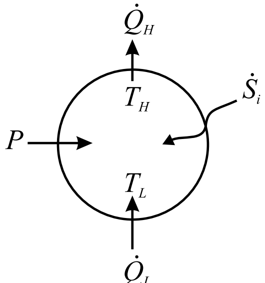

Figure 3.12: Schematic of a refrigerator.

It is now easy see to that an increase in losses ($\dot{S}_i$) results in a higher required input power for the same amount of cooling power. In the case of no losses ($\dot{S}_i = 0$) the cycle is reversible and equals the Carnot cycle. Using this, a CFHX configuration can be found that is optimal for a certain application, producing a minimum of entropy and thus has minimum losses. De Waele and Will have described these methods extensively [27–30]. These entropy methods were also applied to Stirling cycle machines by Organ [31] although he did not include entropy generation due to heat conduction through the heat exchanger wall, nor did he describe the influence of radiation losses.

In the next section, all relevant entropy relations are derived. Apart from entropy production in the CFHX, also the entropy produced in the throttling process in the JT restriction is considered. Section 3.5.2 gives an example of the optimization steps, using the presented relations, carried out for the micro cooler. The parameter sensitivity of the optimum is discussed in section 3.5.3. A generalization of micro CFHX dimensions for cooling powers between 10 and 120 mW is presented in section 3.5.4.

3.5.1 Entropy production in the cold stage

Irreversibilities (e.g. friction, unrestrained gas expansion, etc) and heat transfer cause production of entropy in a cooling cycle [1, 32–35]. In order to derive the equations of entropy production in a cold stage, first the entropy relations of the schematic system of figure 3.12 are described. Using equation 3.43 and stating that $T_L = T$ and $T_H = T + \Delta T$ and $\dot{Q}_L = \dot{Q}_H$, there will be an entropy generation in the system of:

$$\dot{S}_i = \dot{Q}\left(-\frac{\Delta T}{T(T+\Delta T)}\right) \tag{3.46}$$

Since the temperature difference over an infinitesimal length dl is small, the entropy production rate per unit length can be expressed as:

$$\frac{d\dot{S}_i}{dl} = -\dot{Q}\frac{1}{T^2}\frac{dT}{dl} \tag{3.47}$$

In order to calculate the entropy production, it is necessary to know the temperature gradient ($\frac{dT}{dl}$) along the system that can be evaluated using the methods presented in section 3.3.

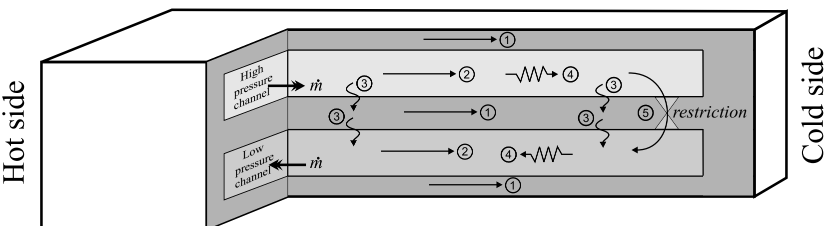

Figure 3.13: Schematic of a cold stage with the different sources of entropy production.

Losses in a cold stage can be divided into five direct sources of entropy generation which is illustrated in figure 3.13. These sources are:

① longitudinal heat conduction through the CFHX material

② longitudinal heat conduction through the gas

③ heat exchange between gas and CFHX material

④ flow resistance in the CFHX channels

⑤ the throttling process

These sources and their corresponding equations are described in the following paragraphs. In the losses listed above, radiation losses are not included. This is because radiation on the CFHX's surface does not directly cause entropy generation in the CFHX's system. It affects the CFHX's temperature profile which, as mentioned before, determines the entropy production. Hence, radiation is taken into account determining the total entropy generation through its influence on ($\frac{dT}{dl}$). The same holds for other parasitic heat loads entering the CFHX (e.g. through mechanical support).

Entropy generation due to longitudinal conductive heat flow through the CFHX material.

The internal entropy production rate per unit length due to heat conduction through the CFHX material can be calculated using equation (3.47) with $\dot{Q} = -\lambda_m A_m \frac{dT}{dl}$, where the direction l is taken along the CFHX.

This results in:

$$\left(\frac{d\dot{S}_i}{dl}\right)_{cond.mat} = \lambda_m A_m \frac{1}{T^2}\left(\frac{dT}{dl}\right)^2 \tag{3.48}$$

with λ_m the heat conduction coefficient of the CFHX material and A_m the cross-sectional area of the CFHX body.

Entropy generation due to conductive heat flow through the gas.

The entropy production rate due to heat conduction through the gas can in the same way be expressed by:

$$\left(\frac{d\dot{S}_i}{dl}\right)_{cond.gas} = \lambda_g A_g \frac{1}{T^2}\left(\frac{dT}{dl}\right)^2 \tag{3.49}$$

with λ_g the heat conduction coefficient of the gas and A_g the cross-sectional area of the channel.

Entropy generation due to heat exchange between high-pressure gas, CFHX material and low-pressure gas.

The heat flux from the high-pressure gas via the wall to the low-pressure gas results in an entropy production in three steps: high-pressure gas to wall material, wall transition and wall material to low-pressure gas. In all three steps, entropy is generated (respectively $\dot{S}_h$, $\dot{S}_m$ and $\dot{S}_l$). Usually, the wall thickness t is relatively small compared to the other dimensions of the system so the entropy production during the wall transition can be neglected. However, for a micro cooler which will be used as an example, this is not necessarily the case.

We know for the steady state that:

$$\dot{S}_i = \dot{S}_h + \dot{S}_m + \dot{S}_l \tag{3.50}$$

To calculate this entropy production, we define three temperatures: the high-pressure gas temperature, the wall temperature and the low-pressure gas temperature, see figure 3.14.

Equation 3.50 can be rewritten as:

$$\dot{S}_i = \dot{S}_{i,I} + \dot{S}_{i,II} \tag{3.51}$$

where $\dot{S}_i$ is divided in the entropy generation due to the heat flux from the high-pressure gas to the middle of the wall and the entropy generation due to the heat flux from the middle of the wall to the low-pressure gas:

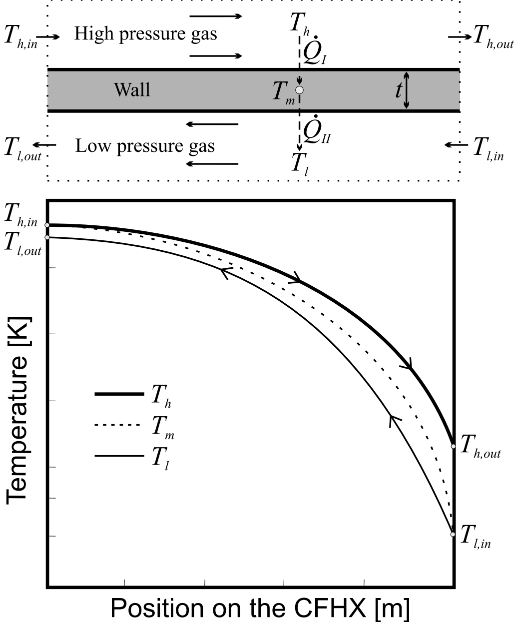

Figure 3.14: Schematic of a CFHX and the temperature profiles.

$$\dot{S}_{i,I} = \dot{Q}_I \cdot \left(\frac{1}{T_m} - \frac{1}{T_h} \right) = \dot{Q}_I \cdot \frac{T_h - T_m}{T_h \cdot T_m} \tag{3.52}$$

$$\dot{S}_{i,II} = \dot{Q}_{II} \cdot \frac{T_m - T_l}{T_m \cdot T_l} \tag{3.53}$$

The different heat flows can be written as:

$$\dot{Q}_I = \frac{2\lambda_m A_c (T_h - T_m)}{t_{eff,I}} \tag{3.54}$$

$$\dot{Q}_{II} = \frac{2\lambda_m A_c (T_m - T_l)}{t_{eff,II}} \tag{3.55}$$

where t_{eff} is an effective thickness, which is convenient to determine the contribution of the generated entropy during the wall transition to the total entropy production.

$$t_{eff,I} = t + \left(\frac{2\lambda_m}{h_h} \right) \tag{3.56}$$

$$t_{eff,II} = t + \left(\frac{2\lambda_m}{h_l} \right) \tag{3.57}$$

and

$$h_h = \left(\frac{\lambda_g \cdot Nu}{D_h} \right)_h \tag{3.58}$$

$$h_l = \left(\frac{\lambda_g \cdot Nu}{D_h} \right)_l \tag{3.59}$$

We assume that the contact areas A_c of the high-pressure line and the low-pressure line are the same, which is the case for the micro cooler having rectangular channels, as well as for thin-walled tube-in-tube heat exchangers; Nu is the Nusselt number, D_h the hydraulic diameter, t the thickness of the wall and h the convective heat transfer coefficient.

Equation 3.56 and 3.57 show that the entropy generated in the wall can be neglected if: $t << \frac{2\lambda_m}{h_h}$ and $t << \frac{2\lambda_m}{h_l}$. In order to express the entropy production rate given by equations 3.52 - 3.53 in terms of the temperature profile $\frac{dT}{dl}$ along the CFHX, we take a closer look at a length section dl as shown in figure 3.15.

The contact area of this section equals: $dA_c = O \cdot dl$ with O the cross-sectional dimension of the contact area (in case of a thin-walled tube-in-tube CFHX this is the perimeter).

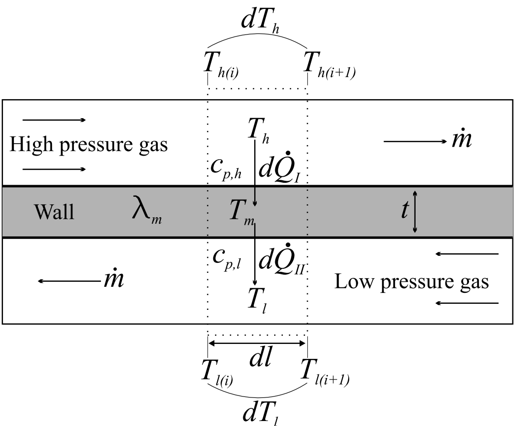

Figure 3.15: Schematic of a cross-section of a CFHX.

The temperature change of the gas and the associated heat flow as depicted in figure 3.15 are related as:

$$d\dot{Q}_I = \dot{m} \cdot c_{p,h} \cdot dT_h = \frac{2\lambda_m dA_c(T_h - T_m)}{t_{eff,I}} \tag{3.60}$$

$$d\dot{Q}_{II} = \dot{m} \cdot c_{p,l} \cdot dT_l = \frac{2\lambda_m dA_c(T_m - T_l)}{t_{eff,II}} \tag{3.61}$$

Combining equations 3.52, 3.53 and 3.60, 3.61 and substitution of $dA_c = O \cdot dl$ results in:

$$\left(\frac{d\dot{S}_{i,I}}{dl}\right) = \frac{t_{eff,I}}{2\lambda_m \cdot O}\frac{(\dot{m} \cdot c_{p,h})^2}{T_h \cdot T_m} \cdot \left(\frac{dT_h}{dl}\right)^2 \tag{3.62}$$

$$\left(\frac{d\dot{S}_{i,II}}{dl}\right) = \frac{t_{eff,II}}{2\lambda_m \cdot O}\frac{(\dot{m} \cdot c_{p,l})^2}{T_m \cdot T_l} \cdot \left(\frac{dT_l}{dl}\right)^2 \tag{3.63}$$

Combining equations 3.62 and 3.63 gives us the total internal entropy production due to the heat flux from high-pressure gas to wall, wall transition and wall to low-pressure gas expressed in the temperature profile along the CFHX:

$$\left(\frac{d\dot{S}_i}{dl}\right)_{gmg} = \frac{t_{eff,I}}{2\lambda_m \cdot O}\frac{(\dot{m} \cdot c_{p,h})^2}{T_h \cdot T_m} \cdot \left(\frac{dT_h}{dl}\right)^2 + \frac{t_{eff,II}}{2\lambda_m \cdot O}\frac{(\dot{m} \cdot c_{p,l})^2}{T_m \cdot T_l} \cdot \left(\frac{dT_l}{dl}\right)^2 \tag{3.64}$$

Entropy generation due to flow resistance in the CFHX channels.

Consider a volume element of the flow channel as depicted in figure 3.16. In the stationary case, the mass in-flow equals the out-flow ($\dot{m}_1 = \dot{m}_2 = \dot{m}$). The second law of thermodynamics yields:

$$\dot{m}s_2 = \frac{\dot{Q}}{T} + \dot{m}s_1 + \dot{S}_i \tag{3.65}$$

Here, s is the specific entropy of the gas and $\dot{Q}$ the heat flow into the element at temperature T. In the case of a very small element, the heat absorbed by the gas equals $d\dot{Q} = \dot{m} \cdot dh$, with h the specific enthalpy. As a result, equation 3.65 gives:

$$Td\dot{S}_i = \dot{m}Tds - \dot{m}dh \tag{3.66}$$

Using the thermodynamic identity $TdS = dH - VdP$ this equation can be written as:

$$d\dot{S}_i = -\frac{\dot{m}}{\rho T}dP \tag{3.67}$$

In case of laminar flow, the pressure drop is given by:

$$dP = -\frac{C}{2}\mu\frac{\nu_m}{D_h^2}dl \tag{3.68}$$

see section 3.1.2. Using equation 3.67 and equation 3.68 we can write:

$$d\dot{S}_i = \frac{\dot{m}}{\rho T}\frac{C}{2}\mu\frac{\nu_m}{D_h^2}dl \tag{3.69}$$

The entropy production rate due to flow resistance in the CFHX channels is thus given by:

$$\left(\frac{d\dot{S}}{dl}\right)_{fr} = \frac{\dot{m}}{\rho T}\frac{C}{2}\mu\frac{\nu_m}{D_h^2} \tag{3.70}$$

In contrast to the entropy generated in the heat-exchange processes considered so far, this flow-resistance term is not directly depended on the temperature profile $\frac{dT}{dl}$ along the CFHX. Nevertheless, it is temperature dependent through T and all gas properties, which are temperature dependent.

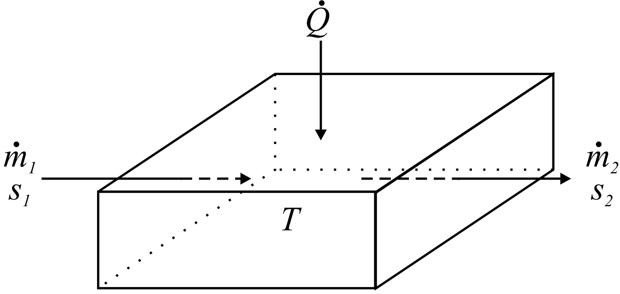

Figure 3.16: Schematic of a volume element of the flow channel.

Entropy generation due to expansion.

The available cooling power at given input Gibbs free energy is determined by the total entropy produced in the cold stage. Apart from the entropy produced in the CFHX discussed in the previous sections, entropy is also produced during the Joule-Thomson expansion. The amount of entropy produced during the throttling process depends on the temperature of the high-pressure gas leaving the CFHX ($T_{h,out}$ see figure 3.14 and 3.17). It thus depends on the temperature profile of the CFHX and is, therefore, related to entropy production terms in equations 3.48, 3.49 and 3.64. Therefore, the entropy produced in the throttling step has to be included in the CFHX optimization process. When the profile is calculated and isenthalpic expansion is presumed, the entropy generation due to expansion (with $\Delta\dot{S} = \dot{m}\Delta s$) can be determined using:

$$\Delta\dot{S}_{exp} = \dot{S}(p_L, H(p_H, T_{h,out})) - \dot{S}(p_H, T_{h,out}) \tag{3.71}$$

Here the first term on the right refers to the low-pressure gas at the same enthalpy value as the high-pressure gas before expansion (point B in figure 3.17) and the second term refers to the high-pressure gas at temperature $T_{h,out}$ (point A).

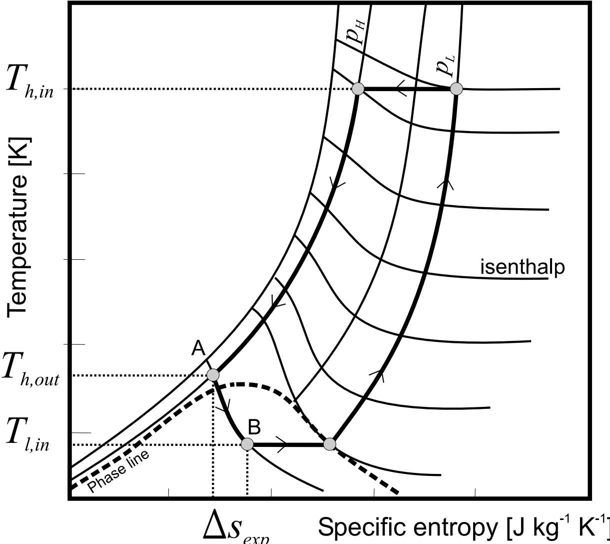

Figure 3.17: T-S diagram of a Linde-Hampson cooling cycle.

3.5.2 Optimization of CFHX dimensions

Most of the CFHX design parameters are fixed through the constraints mentioned in section 1.2 and chapter 2. These are:

- working gas: nitrogen
- high pressure: $p_H = 80$ bar
- low pressure: $p_L = 6$ bar
- environment temperature: $T_{env} = 300$ K
- cold-tip temperature: $T_{tip} = 96$ K
- mass-flow: $\dot{m} = 1$ mg·s^{-1}
- fabrication material: D263T glass
- CFHX geometry: two rectangular channels on top of each other
- emissivity of the outer surface: $\epsilon = 0.02$

However, the precise dimensions of the CFHX are still to be chosen. In general, the cross-sectional area of the CFHX material must be as small as possible to minimize heat conduction losses. Both the cover-, side-wall and the wall thicknesses are constrained by pressure requirements, availability of materials and manufacturing techniques. Cover- and side-wall thicknesses are chosen at a value of 150 μm, see figure 3.18. The wall thickness is chosen at a value of 100 μm.

The geometry of the CFHX *channels* (width, height and length, see figure 3.18) can now be optimized by minimizing the entropy production in the CFHX. As expressed in equations 3.48, 3.49 and 3.64 the temperature profile along the CFHX has to be known for the entropy production to be calculated. The BH-model will be used to calculate the CHFX's temperature profile, as was explained in section 3.3.4.

Optimization process

As a first optimization step, the entropy production is minimized for a CFHX where only the channel width is varied. The two other parameters (i.e. channel height and length) are kept constant. As an example, the five contributions to the entropy production for a CFHX with a channel height of 22 μm and a length of 20 mm are shown in figure 3.19 as a function of channel width. The channel width domain is limited to emphasize the different contributions of entropy production. However, because of this, the total entropy produc-

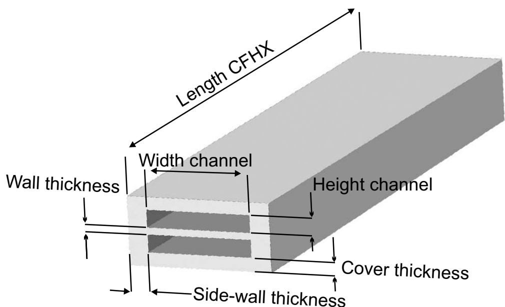

Figure 3.18: Schematic of the CFHX geometry.

tion varies only slightly in the figure. It can be seen in figure 3.19, that for the shown CFHX dimensions, mainly the conduction through the CHFX material, the expansion and the heat exchange between high-pressure gas, CHFX material and low-pressure gas (indicated with $Mat./Gas$) produce entropy. The pressure drop and conduction through the gas produce relatively much less entropy for these geometries.

The pressure drop over the restriction is assumed constant (i.e. 80 bar to 6 bar) to prevent problems with the calculation of the entropy production during expansion. Pressure drop losses for both the high-pressure (Δp_H) and low-pressure (Δp_L) lines are translated to a variation in required compression power (dP_{compr}). Here, the required compression power is defined as the change in Gibbs free energy of the gas ($\Delta G = \Delta H - T\Delta S$) when it is compressed from p_L to p_H. In the lower plot of figure 3.19, the variation in COP is shown. The COP is defined as the net cooling power divided by the total compression power: $COP = P_{net}/P_{compr}$. For zero pressure drop for both high- and low-pressure line, the compression power is: $P_{compr} = 230$ mW for $\dot{m} = 1$ mg·s^{-1}, $p_L = 6$ bar and $p_H = 80$ bar. The small circle in the upper graph gives the minimum entropy production point at a width of approximately 2.7 mm which corresponds to the COP maximum. This calculation is repeated for a range of channel heights. The top plot of figure 3.20 gives the results for 22, 30 and 38 μm.

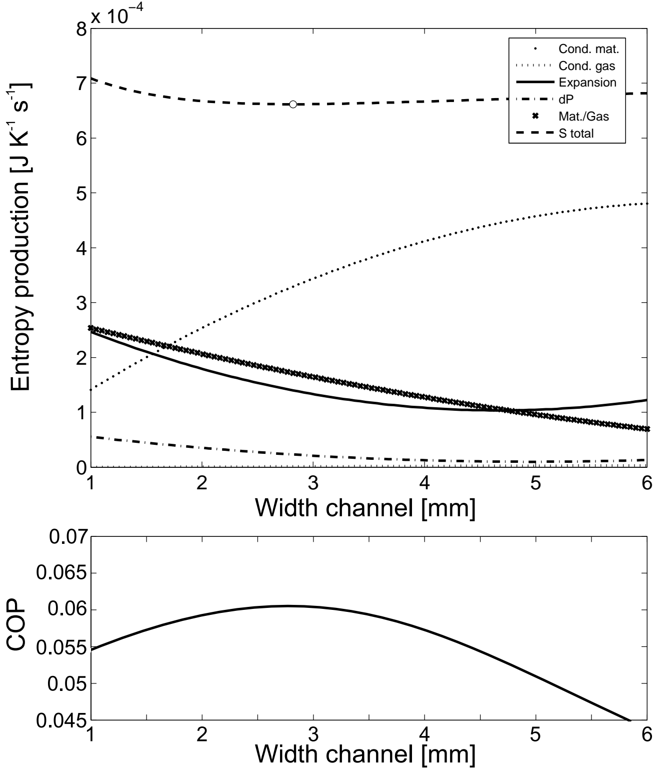

Figure 3.19: Top plot: different entropy productions for varying channel width. Length of the CFHX is 20 mm with a channel height of 22 μm. Bottom plot: corresponding COP.

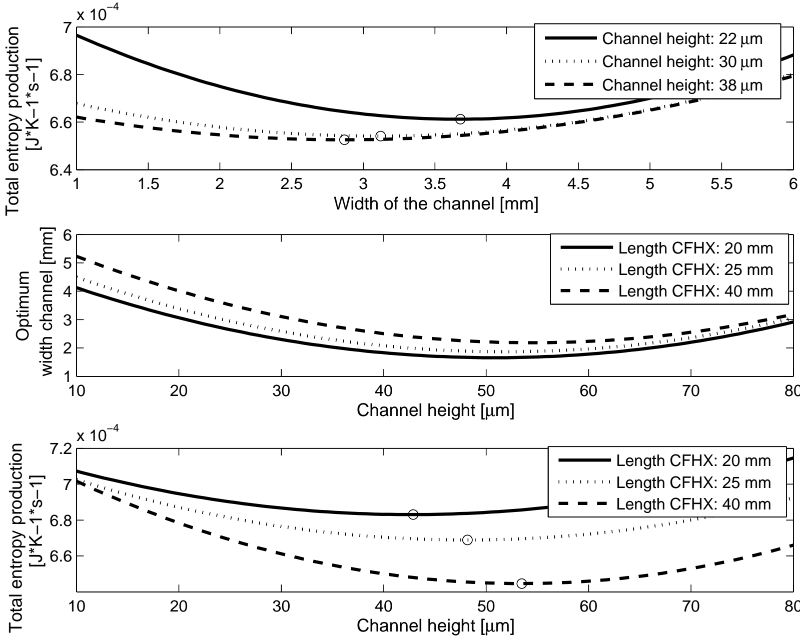

Figure 3.20: Top plot: total entropy productions for varying channel width and height for a CFHX length of 40 mm; middle plot: width as a function of height that produces minimum entropy at three values of the CFHX length; bottom plot: corresponding total entropy production. The circles give the entropy minima.

The CFHX configurations that produce a minimum of entropy (i.e. all minima of the top plot of figure 3.20) can be combined into two new graphs, see figure 3.20 middle and bottom plot. The middle graph shows the width as a function of height that produces minimum entropy with parameter the CFHX length. The lower plot gives the corresponding amount of total produced entropy where again an entropy minimum can be found. These are depicted by the little circles in the bottom plot. If, for instance, the CFHX length is 25 mm, then the channel height should be 48 μm and the channel width 2 mm. The entropy produced in that specific case is $6.7{\cdot}10^{-4}$ J$\cdot$K^{-1}s^{-1}. All minima can again be combined into a new graph, see figure 3.21. All points in this graph give a unique CFHX channel configuration (length, width and height) which produces a minimum of entropy, if one of the three parameters is chosen. Also the net cooling power, change in compression power and the COP are given. The change in compression power (ΔP_{compr}) is the extra power the compressor has to provide to compensate for the pressure drop in the high-pressure (Δp_H) and low-pressure line (Δp_L). This way the pressure difference at the restriction remains constant (80 bar).

Figure 3.21 can be used to find an optimal geometry for a CFHX, depending on the application. For a length of 37 mm, the net cooling has more or less reached its maximum value of about 14 mW. Higher lengths do not considerably increase the net cooling power nor the COP.

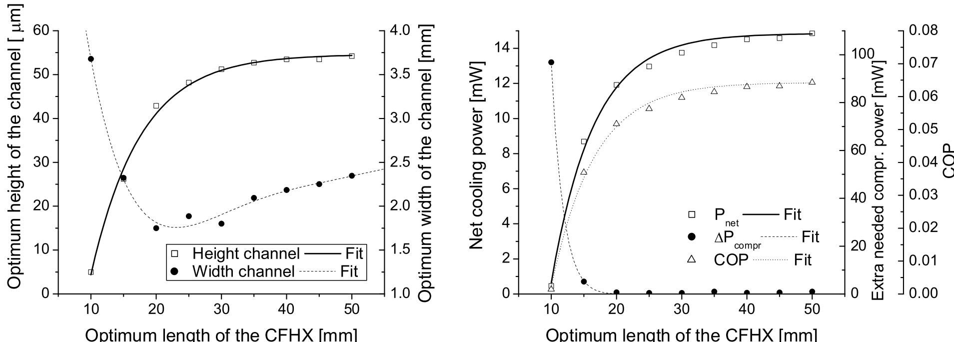

Figure 3.21: Left plot: CFHX channel dimensions which produce a minimum of entropy; right plot: corresponding net cooling power, change in compression power and the net cooling power divided by the total compression power. The dots in the graphs give the calculated points. The lines are polynomial curves fit to the calculated points. A magnification of these graphs can be found in appendix B.1.

The specifications for this geometry are:

Optimal CFHX geometry for maximum COP

P_{gross}:	14.7 mW	COP:	0.063
P_{net}:	14.0 mW	Channel width:	2.1 mm
Δp_H:	0.003 bar	Channel heigth:	53 μm
Δp_L:	0.036 bar	Length CFHX:	37 mm

where P_{gross} is the gross cooling power and P_{net}, the net cooling power which is the gross cooling power minus the heat losses.

Instead of searching for the maximum net cooling power, it is also possible to look for minimum dimensions in combination with a fixed net cooling power. In other words, we are prepared to give in some net cooling power if this leads to significantly smaller CFHX dimensions. For the micro cooler project, the goal was to find a geometry which is as small as possible, in combination with a cooling power of 10 mW. Using figure 3.21, the resulting micro cooler specifications are:

Optimal CFHX geometry for minimum size with $P_{net} = 10$ mW

P_{gross}:	14.7 mW	COP:	0.055
P_{net}:	10.0 mW	Channel width:	2.0 mm
Δp_H:	0.004 bar	Channel heigth:	35 μm
Δp_L:	0.053 bar	Length CFHX:	17 mm

By changing the net cooling power from 14 mW to 10 mW, the length of the CFHX reduces from 37 mm to 17 mm.

3.5.3 Parameter sensitivity of the optimized design

The above-determined dimensions for the micro CFHX are used in a micro cooler design which will be fabricated using MEMS technology. It is important to know the parameter sensitivity of the design, in other words how small variations of the different parameters, which could occur during the fabrication process, will influence the performance of the micro cooler. Figure 3.22 shows the relative effects of small variations in all design parameters on the net cooling power and on the extra compression power needed.

It can be concluded that the relative effect of parameter variations on the extra compression power is much stronger than the effect on the net cooling power. In particular, variations in channel height will have a large impact on pressure drop and thus on the extra compression power needed. On the other hand, one should realize that the absolute amounts of the extra compression power needed are not very large, as can be seen in the second graph of figure 3.21. The overall effect of variations in geometry on the net cooling power are minimal. Changes in wall thicknesses hardly affect pressure drops and thus also have negligible effect on the required compression power.

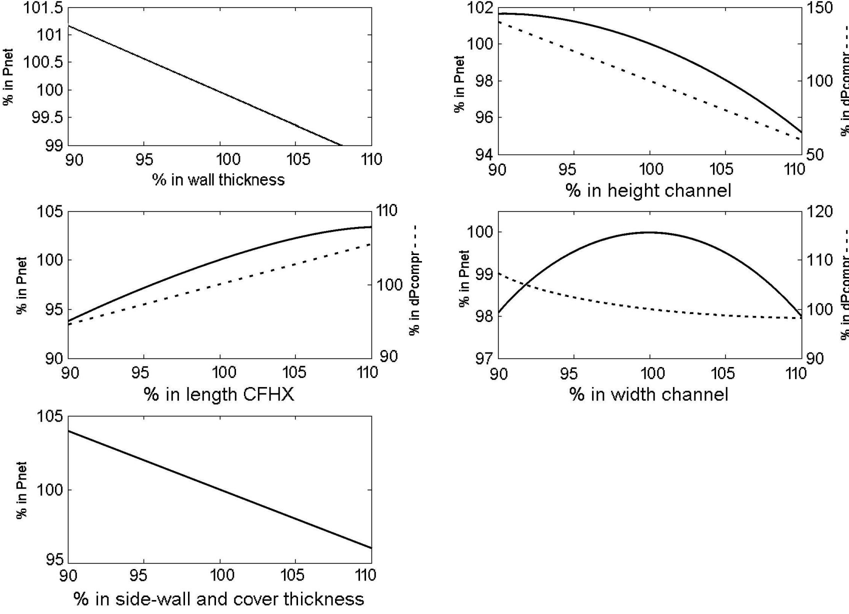

Figure 3.22: Influence of relative variations of all parameters on the net cooling power and difference in the extra compression power needed.

3.5.4 Optimum CFHX dimensions for various cooling powers in the mW range

The above-discussed optimization method is used to find optimal CFHX configurations for coolers with a variety of net cooling powers (in the milliwatt range). The results are shown in figure 3.23. The cover thickness and side-wall thickness (figure 3.18) were kept at a value of 150 μm. The wall thickness is 100 μm. To compare the different CFHX configurations, the net cooling power is chosen at a value of 95 % of the gross cooling power. The absolute values of the dimensions shown in figure 3.23 will change if another percentage is chosen. However, the shape of the different curves and resulting trends will remain the same.

It is remarkable that for a net cooling power above approximately 40 mW the optimum height of the channel becomes constant (about 37 μm). If a lower percentage of the gross cooling power is chosen, this cooling power value will decrease (e.g. for $P_{net} = 0.85 \cdot P_{gross}$, the channel height becomes more or less constant at a value of about $P_{net} = 25$ mW). Also the length reduces to a more or less constant value at larger values of the cooling power (about 31 mm). The width of the channel however, increases linearly over the whole domain. For higher cooling powers it is apparently sufficient to 'use a number of identical coolers in parallel' to increase the net cooling power. Because of the relatively high gross cooling power and the fact that the side-wall- and cover thicknesses do not increase with increasing gross cooling power, conduction losses do not affect the required net cooling power as significantly as for small cooling powers.

For smaller cooling powers conduction losses become relatively high. To reduce these,

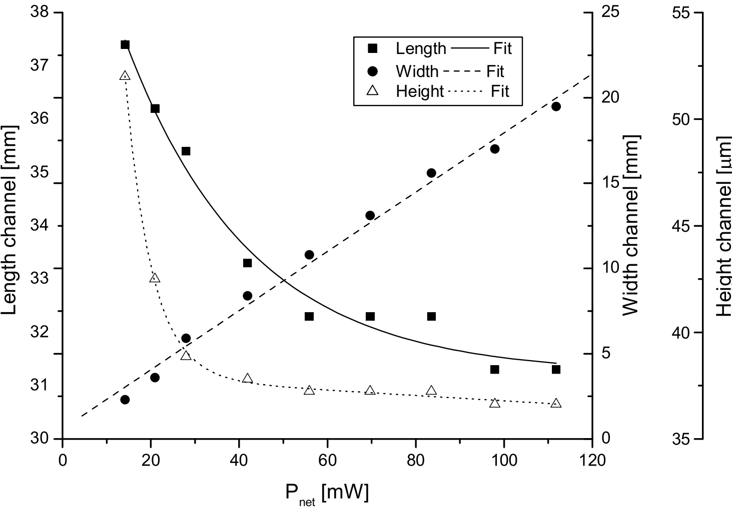

Figure 3.23: Optimal CFHX dimensions for different cooling powers. The net cooling power is chosen at 95 % of the gross cooling power. $P_{net} = 0.95 \cdot P_{gross}$. Cover thickness and side-wall thickness are 150 μm and the wall thickness is 100 μm. The dots in the graphs give the calculated points. The lines are polynomial curves fit to the calculated points.

the CFHX's length increases and the width reduces such that the net cooling power remains at the fixed 95 % of the gross cooling power, as is seen in the graph. However, the increase of the channel length combined with a width decrease, will result in a higher (entropy generation due to) pressure drop. This is compensated by drastically increasing the channel's heigth. At this point, a compromise has to be found between heat conduction losses and pressure drop losses, which is established by the minimization of entropy production.

3.6 Conclusions

Three different calculation methods to determine the temperature profile of a CFHX were investigated and compared. These methods are: the Log Mean Temperature Difference (LMTD) method, the enthalpy (Δh) method and the Bahnke-Howard (BH) method. These methods differ in solving method and the required in- and resulting output parameters. In the first two methods, heat flow through the material in longitudinal direction and radiation on the CFHX outer surface is neglected in determining the temperature profile. It was found that these heat flows can not be neglected for a micro cold stage and therefore, the BH-model was used to determine the temperature profile.

During the design of a CFHX, it is convenient to regard all losses inside the CFHX as a generation of entropy. The advantage of this approach, unlike other methods, is that the different losses can be compared and summed. Equations for the different entropy losses in a CFHX are given. During the optimization process of a CFHX, the design parameters are varied to find an optimal configuration for a certain application. Two examples are discussed in which three parameters are optimized (i.e. CFHX channel width, height and length). An optimal configuration which aims at a maximum net cooling power and a configuration that results in a CFHX with minimum dimensions are presented. The latter design is used for the realization of the cryogenic micro cooler.

A trend for the variation of all parameters is shown for Joule-Thomson cryocoolers, based on the presented MEMS design, with a cooling power in the mW-range using the optimization which aims at a maximum net cooling power. The net cooling power is chosen at a value of $P_{net} = 0.95 \cdot P_{gross}$. For powers between 40 and 120 mW it is sufficient to use a number of identical coolers in a parallel way to achieve the net cooling power. For cooling powers between 10 and 40 mW, configurations are found which result in a balance between minimum heat conduction and pressure drop losses.

References

[1] A. Bejan. *Heat Transfer.* John Wiley & Sons New York, 1993. ISBN 0-471-50290-1.

[2] L. F. Moody. Friction factors for pipe flows. *Trans. ASME*, 66:671–684, 1944.

[3] J. Nikuradse. Stromungsgesetze in rauhen Rohren. *VDI-Forschungsh*, 361:1–22, 1933.

[4] Wu Peiyi and W. A. Little. Measurement of friction factors for the flow of gases in very fine channels used for microminiature Joule-Thomson refrigerators. *Cryogenics*, 23:273–277, May 1983.

[5] X.F. Peng, G.P. Peterson, and B.X. Wang. Heat transfer characteristics of water flowing through micro channels. *Exp. Heat Ransfer*, 7:265–283, 1994.

[6] R. K. Shah and A. L. London. *Laminar flow forced convection in ducts.* Academic Press, New York, 1978.

[7] W. M. Kays and M. E. Crawford. *Convective heat and mass transfer.* McGraw-Hill, Inc., 3rd edition, 1993. ISBN 0-07-033721-7.

[8] S.M. Marco and L.S. Han. A note on limiting laminar Nusselt number in ducts with constant temperature gradient by analogy to thin-plate theory. *Trans ASME*, 77:625–630, 1955.

[9] H.L. Mo, Y.X. Zhou, T.Y. Zhu, and T.W. Guo. Forced convection of low temperature nitrogen gas in rectangular channels with small aspect ratio. *Cryogenics*, 44:301–307, 2004.

[10] X.F. Peng, B.X. Wang, and G.P. Peterson. Experimental investigation of heat transfer in plates with rectangular micro channels. *Int. Journal Heat mass transfer*, 38:127–137, 1995.

[11] Wu Peiyi and W. A. Little. Measurement of the heat transfer characteristics of gas flow in fine channel heat exchangers used for microminiature refrigerators. *Cryogenics*, 24:415–420, 1984.

[12] S.B. Choi, R.F. Barron, and R.O. Warrington. Fluid flow and heat transfer in microtubes. *Micromechanical Sensors, Actuators and Systems*, pages 123–134, 1991.

[13] C.K. Hsieh and K.C. Su. Thermal radiative properties of glass from 0.32 to 206 μm. *Solar Energy*, 22:37–43, 1979.

[14] A. Bendavida and P.J. Martina and L. Wieczorekb. Morphology and optical properties of gold thin films prepared by filtered arc deposition. *Thin Solid Films*, 354:169–175, 1999.

[15] A. Roth. *Vacuum technology.* Elsevier Amsterdam, 3nd edition, 1990. ISBN 0-444-86027-4.

[16] E. Suurmeijer and T. Mulder and J. Verhoeven. *Basisboek vacuümtechniek.* Krips, Meppel, 2nd edition, 2000. ISBN 90-9013776-9.

[17] F.P. Incropera and D.P. de Witt. *Fundamentals of heat and mass transfer.* Wiley & Sons, New York, 1990.

[18] H. Hausen and H. Linde. *Tieftemperaturtechnik: Erzeugung sehr tiefer Temperaturen, Gasverflüssingung und Zerlegung von Gasgemischen.* Springer-Verlag, Berlin, 2nd edition, 1985.

[19] The MathWorks, Inc. 3 Apple Hill Drive, Natick, MA 01760-2098, USA, http://www.mathworks.com.

[20] W. M. Kays and A. L. London. *Compact heat exchangers.* McGraw-Hill Book Company New York, 2nd edition, 1964.

[21] G. Bahnke and C. Howard. The effect of longitudinal heat conduction on periodic-flow heat exchanger performance. *Journal of engineering for powers*, 86:105–120, 1964.

[22] K.C. Ng, H. Xue, and J.B. Wang. Experimental and numerical study on a miniature Joule-Thomson cooler for steady-state characteristics. *International Journal of Heat and Mass Transfer*, 45:609–618, 2002.

[23] S. Pradeep Narayanan and G. Venkatarathnam. Analysis of performance of heat exchangers used in practical micro miniature refrigerators. *Cryogenics*, 39:517–527, June 1999.

[24] H. Xue, K.C. Ng, and J. B. Wang. Performance evaluation of the recuperative heat exchanger in a miniature JouleThomson cooler. *Applied Thermal Engineering*, 21:1829–1844, 2001.

[25] H. Nagai and et al. Development of small 2K cryocooler (II) - High efficient and low pressure drop heat exchanger. In *AIP conference proceedings*, pages 1491–1498, 2002.

[26] C. Harris, M. Despa, and K. Kelly. Design and Fabrication of a Cross Flow Micro Heat Exchanger. *Journal of Microelectromechanical Systems*, 9(4):502–508, 2000.

[27] M. E. Will and A. T. A. M. De Waele. Comparison of the performance of regenerators to counterflow heat exchangers. In *ICEC 20 conference proceedings*, Beijing, 2004.

[28] M. E. Will and A. T. A. M. De Waele. Heat exchanger versus regenerator: a fundamental comparison. *Cryogenics*, 45:473–480, 2005.

[29] A. T. A. M. De Waele, P. P. Steijaert, and J. Gijzen. Thermodynamical aspects of pulse tubes. *Cryogenics*, 37:313–324, 1997.

[30] A. T. A. M. De Waele. Optimization of pulse tubes. *Cryogenics*, 39:13–15, 1999.

[31] A. J. Organ. Thermodynamic design of Stirling cycle machines. *Proc. Inst. Mech. Engrs.*, 201(C2):107–116, 1987.

[32] A. Bejan. *Entropy generation minimization, The Method of Thermodynamic Optimization of Finite-Size Systems and Finite-Time Processes.* CRC Press New York, 1996. ISBN 0-8493-9651-4.

[33] A. Bejan. Entropy generation minimization: The new thermodynamics of finite-size devices and finite-time processes. *J. Appl. Phys.*, 79(3):1191–1218, 1996.

[34] H. Callen. *Thermodynamics and an introduction to thermostatistics.* John Wiley & Sons New York, 2nd edition, 1985. ISBN 0-471-86256-8.

[35] C.B.P. Finn. *Thermal Physics.* Chapman & Hall, 2nd edition, 1993. ISBN 0-412-49540-6.

Chapter 4

Mechanical stress compensation

The pressure inside the high-pressure micro channel is 80 bar. This relatively high pressure in combination with the thin glass channel walls can result in high mechanical stresses inside the fabrication material (D263T glass). Calculations on the stress distribution inside the material are relevant to minimize to chance of mechanical failure of the micro cold stage.

4.1 Strain and stress definition

4.1.1 Stress

If a force is applied to an object, the internal distribution of force per unit area is called the stress and is defined by:

$$\sigma = \frac{F}{A} \tag{4.1}$$

where A is the surface to which the force F is applied. As can be seen from equation 4.1 the unit of stress is N·m^{-2} or Pa. If the force is expanding the object, the stress is called tensile. The stress is called compressive if the force is in reversed direction, causing the object to be compressed. Stress acting in perpendicular direction to the surface is referred to as normal stress ($\sigma_\perp$), either tensile (positive sign) or compressive (negative sign). Stress acting in parallel direction to the surface is called shear stress ($\sigma_\parallel$). Inside an object, the stress varies in both value and direction. Using a coordinate transformation, so-called principal stresses can be defined. In the principal directions, all stresses are normal which makes analytical stress calculations easier. The definition and calculation of these stresses can be found in literature [1, 2].

4.1.2 Strain

The deformation of an object is called strain and is defined as the change in dimension of the object (δ) divided by the original dimension (D) before applying the force:

$$\epsilon = \frac{\delta}{D} \tag{4.2}$$

If the object is in tension, the strain is called tensile strain (positive). If the object is in compression, the strain is called compressive strain (negative). Materials that undergo large strains before failure (e.g. clay and steel) are classified as ductile. Materials that fail in tension at relatively low values of strain (e.g. glass, ceramic, etc.) are classified a brittle materials.

4.1.3 Relationship between stress and strain

Hooke's law gives the relationship between stress and strain and is defined as: $\sigma_{\perp} = E\epsilon$, where E [Pa] is the modulus of elasticity or Young's modulus. The same holds for the relationship between shear stress and strain: $\sigma_{\parallel} = G\gamma$, where G [Pa] is the shear modulus of elasticity, also known as the modulus of rigidity and γ is a measure of the deformation due to the shear stress $\sigma_{\parallel}$. The stress-strain relationship and fracture mechanism of glass has been investigated by different groups [2–8]. The found Young's modules for glass depends on the type of glass (e.g. for Pyrex $E \approx 64$ GPa [8], for D263T glass $E \approx 73$ GPa [7]).

4.1.4 Failure criteria

There are many failure criteria. Different ones are used to predict the failure of brittle and ductile materials. Some examples are the Mohr's theory of failure, Tresca's criterion and the Von Mises criterion [1, 2, 9, 10]. All criteria state that failure occurs when the (principle) stress exceeds a certain maximum stress. The definition of this maximum stress varies for the different criteria. The Rankine criterion [2], also known as the normal stress criterion, is often used to predict the failure of brittle materials like glass. This criterion states that failure occurs when the maximum principal stress reaches either the uniaxial tension strength σ_t, or the uniaxial compression strength σ_c,

$$-\sigma_c < (\sigma_{p1}, \sigma_{p2}) < \sigma_t \tag{4.3}$$

where σ_{p1} and σ_{p2} are the principal stresses for 2D stress. A visualization of this failure criterion can be seen in figure 4.1. Brittle materials can in general withstand higher compressive than tensile stresses. The two principal stresses should lie within the

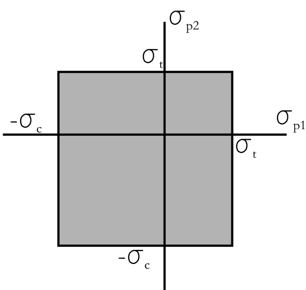

Figure 4.1: The Rankine criterion.

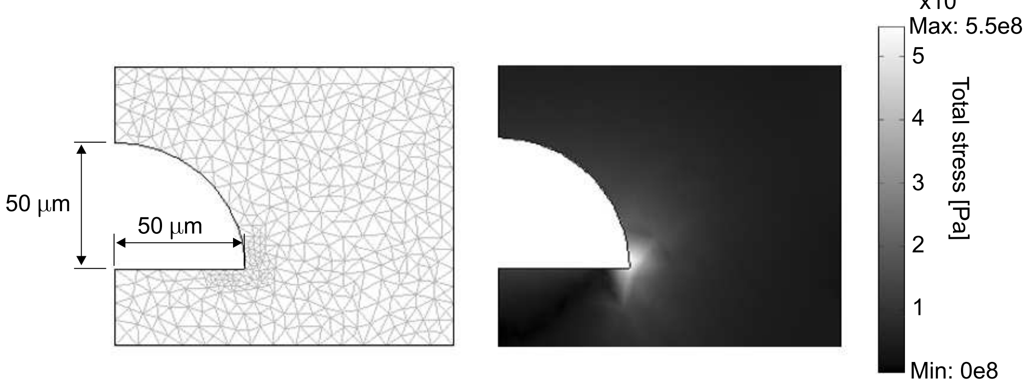

Figure 4.2: Femlab model of an isotropically etched channel with a depth of 50 μm. The pressure inside the channel is 80 bar. Left: channel geometry with on the left side the symmetry axis and the Femlab-mesh included. Right: stress distribution inside the glass. A peak value of 550 MPa is found in the channel corner.

gray zone for no failure to occur. Maximum (tensile) stress values for glass found in literature vary from σ_{max} = 50 MPa to σ_{max} = 140 MPa [1–3, 7, 11]. It is known that the dominant weakening flaw in glass is a small crack or defect which can be the location of a high-stress concentration and acts as the starting point of a failure [3, 12]. It is often the case that these defects arise during the production process of glass devices. In other words the used production process can be the cause of a mechanical failure and thus have an influence on the maximum allowable stress inside the micro structure. This will be discussed further in section 4.3.

4.2 Finite element simulation

Finite element simulations, using Femlab [13], have been done to make an estimate of the stress distribution inside a pressurized micro channel. An isotropically wet etched channel without any defects and with a depth of 50 μm is used as the geometry, see figure 4.2. The pressure inside the channel is set to 80 bar. The left figure of figure 4.2 shows the channel geometry with the chosen mesh. The right figure shows the calculated stress distribution inside the geometry. The model uses the mechanical properties of D263T glass as is stated by the manufacturer [7]. The results show extremely high stresses concentrated in the sharp corner of the pressurized channel (σ_{max} = 550 MPa). This value exceeds the maximum stress values for glass found in literature ($\sigma_{max} \approx$ 140 MPa for D263T glass) by far. However, the found results strongly depend on the specific mesh that is chosen. The smaller the mesh, the higher the peak value. This is a result of the infinitely sharp corner that is used in the computer model. In practice this corner will have a finite curvature. Because it is difficult to predict this curvature the simulation results can be used as a qualitative indication only.

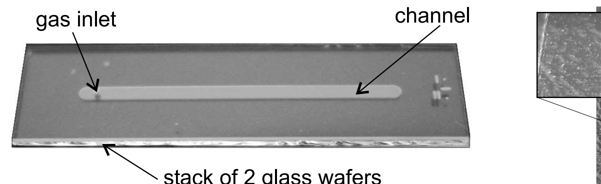

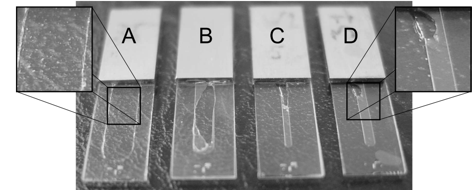

Figure 4.3: Pressure test samples. Left: single channel, the width is 780 μm. Right: various tested samples glued onto stainless steel connection plates. Samples A and B have a channel width of respectively 3000 and 2000 μm; channel C and D have a channel width of respectively 780 and 1000 μm. Samples A and B show a different failure mode than samples C and D. All samples shown failed at a certain pressure as is given in figure 4.5

4.3 Pressure tests

Clarity about the maximum allowable stresses inside processed D263T glass wafers is needed to minimize the chance of a mechanical failure of the micro cold stages. Since simulations give no clear value of the stresses involved and the maximum stress inside a glass micro structure can depend on the used production process, pressure tests were performed to determine the maximum allowable stress in thin D263T glass wafers (thickness = 175 μm). Pressure test samples were fabricated that consist of a single channel HF etched in a 175 μm thick D263T glass wafer, see figure 4.3. The channel width varies from 110 μm to 3000 μm. The channel depth is 50 μm leaving a membrane thickness of about 125 μm. Another glass wafer with a thickness of 400 μm is fusion bonded to the thin wafer. Gas pressure is applied via a micro hole (diameter 300 μm), powder blasted in the 400 μm wafer. Variability of the glass substrates thickness is standard $\pm 10\%$ according to the manufacturer's specification [7]. Etching depths are accurate to $\pm 2\%$. Variability in the channel widths is standard ± 4 μm. The channel corner has a 90° angle with the top plate which is ensured by the isotropic etching process. SEM observations have been done to ensure proper isotropic behaviour [14]. The production process of these test channels resembles the production process of the flow channels in the micro cold stage as will be discussed in chapter 5. This way, failures due to high-stress concentration at defects or small cracks induced by proces steps are taken into account.

To support the connection part, the area surrounding the powder blasted micro hole is glued between rectangular pieces of stainless steel. The total sample can then be clamped in a connection piece which contains small Viton O-rings [15], see figure 4.4. This connection piece has two gas connections because it will also be used to connect the cold stage, see section 6.1. The samples are tested in a relative pressure range of 0-120 bar until they fail. The maximum normal (a.k.a. bend) stress inside the material is defined as:

$$\sigma_{\perp,max} = \frac{p_{max} w^2}{2d^2} \tag{4.4}$$

with p_{max} the failure pressure of the sample, w the width of the channel and d the thickness of the membrane. The maximum shear stress inside the material is defined as:

$$\sigma_{\parallel,max} = \frac{p_{max} w}{2d} \tag{4.5}$$

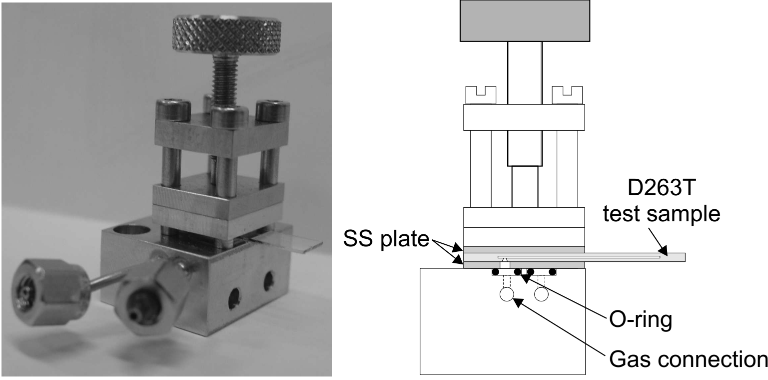

Figure 4.4: Left: picture of the sample connection. Right: schematic.

Equations 4.4 and 4.5 are derived for a uniformly distributed load on a rectangular plate clamped at both sides [1, 2]. The total stress inside the material is a combination of the two stresses. The bend to shear stress ratio is given by: w/d meaning that for the test samples the bend stress equals the shear stress for a channel width of 125 μm. Therefore, it can be concluded that the bend stress will dominate in the majority of the tested samples.

Figure 4.5 shows the results of the pressure tests for channel widths larger than 500 μm. Samples with a channel width smaller than 500 μm did not fail within the applied pressure range. These were: 2 samples with a channel width of 150 μm, 2 samples with 350 μm and 2 samples with 450 μm. The graphs show the different values of the maximum normal and shear stress, determined by substituting the found failure pressure of a sample in equations 4.4 and 4.5, with the total stress being a combination of the two. The maximum normal stress increases with increasing channel width whereas the maximum shear stress is decreasing with increasing channel width.

The graphs show that, in almost all cases, the maximum normal stress found in the experiments is equal or higher than the maximum stress value we found in literature

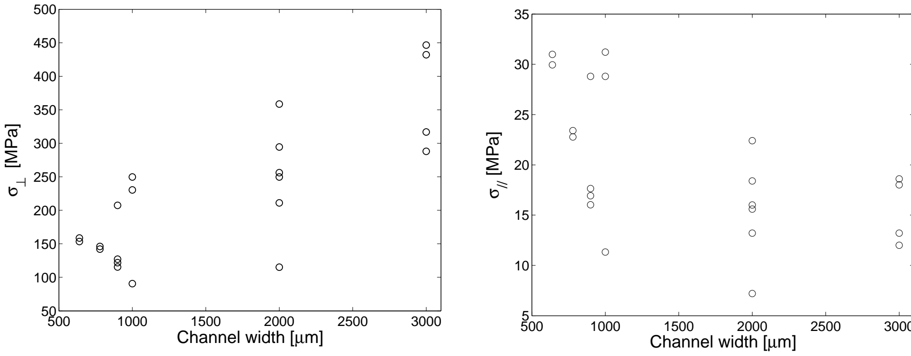

Figure 4.5: Pressure tests results. Left: maximum normal stress, right: maximum shear stress.

for D263T glass, i.e. 140 MPa [7]. The maximum found normal stress is determined at $\sigma_{\perp} = 450$ MPa and the maximum found value for the shear stress is $\sigma_{\parallel} = 31$ MPa. The total number of samples tested is 27 (i.e. the ones shown in figure 4.5 and the 6 samples with a channel width smaller than 500 μm). As was mentioned before, local defects in the glass (e.g. caused by the production process) can be a location for stress concentration and a starting point of a fracture. This property will result in a statistical distribution of the found maximum stresses for samples with the same channel width, explaining the spread in the found maximum stresses.

Non of the tested single channel samples (figure 4.5) showed a failure that indicated a rupture of the bond. In other words, all the samples failed by exceeding the maximum mechanical stress of the material, not by exceeding the maximum bond stress. The samples with a channel width between 640 μm and 1000 μm have a different failure mode than those with a width of 2000 μm and 3000 μm. The first always showed a failure where a small piece of the membrane blew off from the edge of the channel (see figure 4.3 magnification of sample D). At larger channel widths, the entire membrane was destroyed each time (see figure 4.3 magnification of sample A). As was expected, it can be concluded that for the first group shear stresses play a larger role in the failure mechanism than for the second group. The samples fail by exceeding the maximum (shear) stress at a location at the channel edge where the stress is concentrated (e.g. a wafer defect or pinhole). In the second group, the bend stress is mainly the bottleneck. Since the channels are much wider, the bend stress in the middle of the channel membrane is much higher. The membrane will bend to its maximum deflection and break from the middle, tearing the entire membrane surface.

Besides determining the maximum normal and shear stresses of the material, also the maximum bond stress was tested. The maximum bond stress of a glass-glass direct bond found in literature varies from about 10 MPa [16, 17] to 25 MPa [18]. The bond sample is designed such that the force inside the channel is divided over a large area using pillars, see left picture of figure 4.6. In this way, both the normal and the shear stress are kept at relatively low values (w is very small) and the bond stress will be the limiting factor. If we define a unit cell of such a bond sample, see figure 4.7, the maximum bond stress in the material can be defined as:

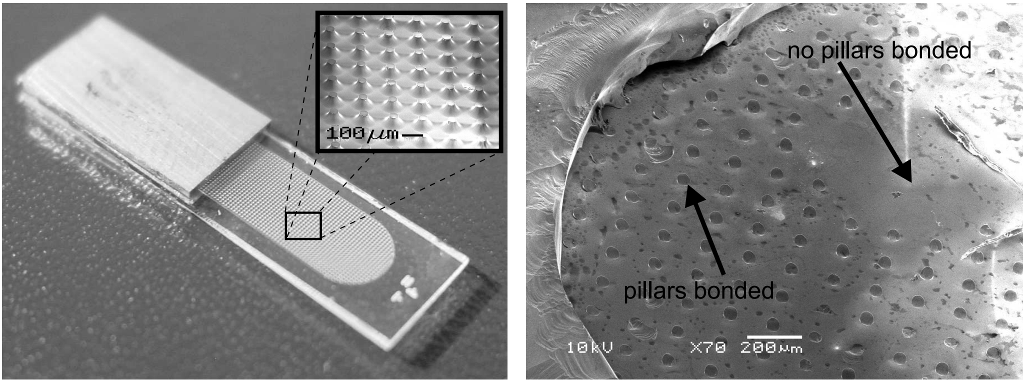

Figure 4.6: Bond test sample with SEM picture of the pillars inside the channel.

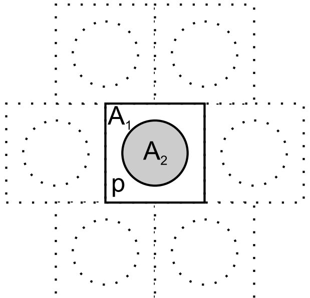

Figure 4.7: Unit cell of a bond sample.

$$\sigma_{bond,max} = \frac{p_{max} A_1}{A_2} \tag{4.6}$$

where A_1 is the channel surface and A_2 is the bonded surface.

Seven of these bond samples were tested. Six of the samples failed at relatively low pressures: 2, 5, 7, 15 and two at 17 bar which corresponds to bonding stresses of about respectively 2, 5.5, 7.5, 16 and 18 MPa. After failure these samples where inspected with a SEM. It was observed that for all of these samples, the bond quality of the pillars was very poor. There are regions where no pillars are bonded to the membrane, as can be seen in the right picture of figure 4.6. This results in much larger spans between the pillars increasing both the shear and bend stress. It is very likely that all these samples failed by exceeding the shear and/or bend stress and not the bond stress. Fortunately, one sample did not have large areas without bonded pillars. This sample failed at a pressure of 75 bar corresponding to a maximum bond stress of about 82 MPa. It can thus be concluded that if the bond is perfect, a relatively high maximum bond stress can be accomplished. However, it should also be noted that imperfections in the bond interface between the pillars and the membrane can introduce more fracture initiation points and thus may result in a lower maximum pressure because of stress concentrations.

4.4 Channel pillar configuration

All results presented in the previous paragraph are used in the design of the micro cold stage. The high- and the low-pressure channels as well as the restriction contain pillars to keep the maximum stress within limits. It is seen to it that the maximum calculated stress in the micro cooler prototype does not exceed a chosen maximum allowable stress. For the maximum allowable stress the following values were taken: $\sigma_{\perp,max} = 26$ MPa, $\sigma_{\parallel,max} = 5$ MPa and $\sigma_{bond,max} = 5$ MPa. All of these values are below the maximum found values during the pressure tests. Using these relatively low values, the cold stage should be able to withstand 80 bar.

A circular geometry is chosen for the pillars inside the gas channels to minimize the chance of process imperfections and stress concentrations. Pillar dimensions and distribution are calculated using equations 4.4, 4.5 and 4.6. Figure 4.8 shows the pillar configuration of the high-pressure channel. Because the cold stage is fabricated of glass and hence is transparent, the pillars in the lower low-pressure channel are also partly

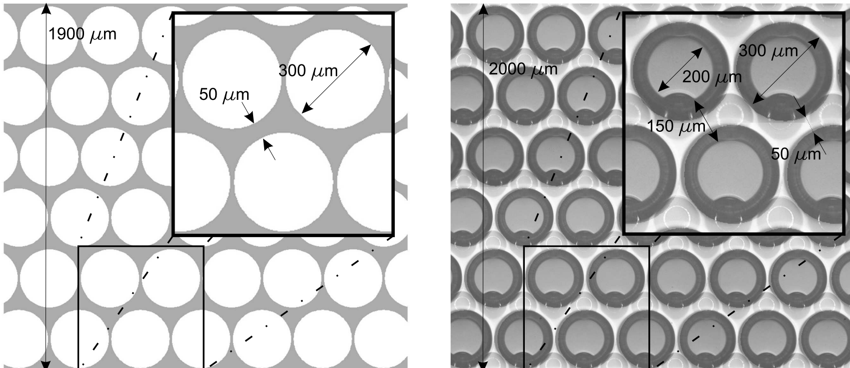

Figure 4.8: Left: the CleWin mask [19] of the high-pressure channel including dimensions. Right: photograph of a part of the cold stage. The photograph has been edited to darken the pillars inside the high-pressure channel.

visible. The figure also gives all the calculated dimensions and a photograph of the actual flow channel. The increase in total channel width and the decrease of pillar diameter by 100 μm, if the mask is compared to the photograph, is the result of the isotropic wet etch process, see section 2.2.2. The pillar configuration of the low-pressure channel is given in figure 4.9. Using these configurations, the maximum stress inside the glass should not exceed the values given above when the channels are pressurized to respectively 80 and 6 bar. The pillars of the high- and low-pressure channel are situated in an alternating way to further reduce material stresses. This way the effective thickness of the middle membrane is increased, reducing both maximum normal and shear stress.

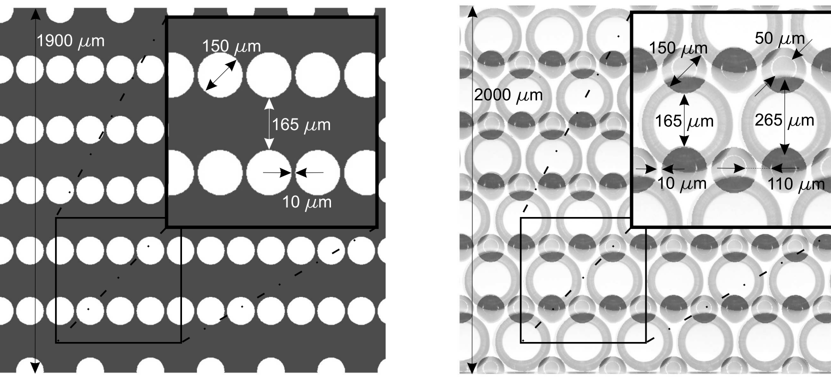

Figure 4.9: Left: the CleWin mask [19] of the low-pressure channel including dimensions. Right: photograph of a part of the cold stage. The photograph has been edited to darken the pillars inside the low-pressure channel.

4.5 Restriction design

As was explained in section 2.3, a relatively wide and shallow flow channel is chosen to serve as a flow restriction. In section 3.4, it was mentioned that the mass flow ($\dot{m}$) through the restriction can be described by:

$$\dot{m}(T) = \frac{1}{12}\frac{wh^3}{l}\int_{p_L}^{p_H}\frac{\rho(p,T)}{\mu(p,T)}dp \tag{4.7}$$

If we use the known values of p_L (6 bar), p_H (80 bar) and $\dot{m}$ (1 mg·s^{-1}) and choose a relatively large restriction width of 1 mm, the height and length are calculated at respectively: 300 nm and 140 μm, using equation 4.7. Also the restriction contains pillars to compensate for mechanical stresses, see figure 4.10. This figure shows several masks (low- and high-pressure pillars and evaporator mask, all in gray-scale) with the mask of the restriction in black. The length of the restriction in the mask is 220 μm. First, this mask is used with a BHF etch to accurately get a restriction height of 300 nm. Next, the high-pressure channel mask is used to HF etch a channel of 50 μm deep. In the same step, the restriction length is reduced to 140 μm as a result of the isotropic etch. Further details on the production process will be discussed in the next chapter. The mass flow through the restriction, at constant pressure difference, depends on the restriction temperature, as can be seen in equation 4.7. Plots of the mass flow versus the restriction temperature for the described restriction can be found in appendix A.

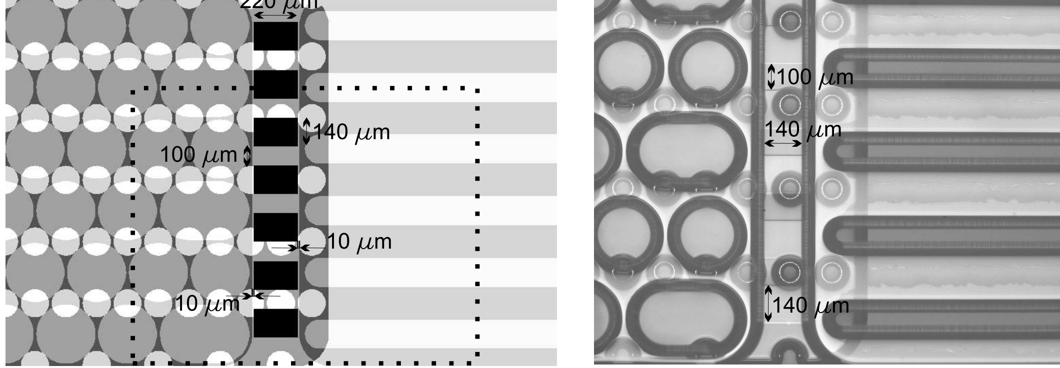

Figure 4.10: Left: the CleWin mask [19] of the cold stage with the restriction mask black. Right: photograph of the squared part in the left schematic. Clearly visible is the cold-stage restriction (300 nm high).

4.6 Conclusions

Local defects in a glass structure (e.g. caused by the production process) can be a location for stress concentration and a starting point of a fracture. The maximum allowable stresses inside processed D263T glass wafers are determined to minimize the chance of a mechanical failure of the micro cold stages. The maximum found normal stress is determined at $\sigma_{\perp} = 450$ MPa and the maximum found value for the shear stress is $\sigma_{\parallel} = 31$ MPa. The maximum bond stress is found at 82 MPa. The high- and the low-pressure channels as well as the restriction contain pillars to keep the maximum stress within limits.

References

[1] J, M. Gere, S. P. Timoshenko. *Mechanics of materials.* Cheltenham, 1999. ISBN 0-7487-3998-X.

[2] W. D. Pilkey. *Formulas for stress, strain, and structural matrices.* Wiley, New York, 1994. ISBN 0-471-52746-7.

[3] K.K. Phani and A.K. Maitra. A cumulative flaw distribution function for predicting failure of glass. *Materials Science and Engineering*, 93:L5–L9, 1987.

[4] M.V. Swain and J.T. Hagan. Indentation plasticity and the ensuing fracture of glass. *J. Phys. D: Appl. Phys.*, 9:2201–2214, 1976.

[5] P.K. Gupta and C.R. Kurkjian. Intrinsic failure and non-linear elastic behavior of glasses. *Journal of Non-Crystalline Solids*, 351:2324–2328, 2005.

[6] D.G. Holloway. The fracture of glass. *Physics Education*, 3:317–322, 1968.

[7] Schott. 555 Taxter Road, Elmsford, NY 10523, USA, http://www.us.schott.com/.

[8] Corning. Koolhovenlaan 12, NL-1119 NE Schiphol-Rijk, The Netherlands, http://www.corning.com.

[9] P. Cornetti, N. Pugno, A. Carpinteri, and D. Taylor. Finite fracture mechanics: A coupled stress and energy failure criterion. *Engineering Fracture Mechanics*, 73:2021–2033, 2006.

[10] Q.M. Li. Strain energy density failure criterion. *Int. Journal of Solids and Structures*, 38:6997–7013, 2001.

[11] P. Heller, J. Vervest, H. Wilbrink. *Vademecum voor de Glastechniek.* Kluwer Technische Boeken B.V. Deventer, 1992.

[12] M.G. Britton. Glass as an engineering material. *Phys. Technol.*, 12:258–262, 1981.

[13] Comsol multiphysics. 1100 Glendon Avenue, Los Angeles, CA 90024, USA, http://www.comsol.com/.

[14] Micronit Microfluidics BV. Hengelosestraat 705, 7521 PA Enschede, The Netherlands, http://www.micronit.com/.

[15] Eriks, Hassinkweg 16, 7556 BV, Hengelo, http://www.eriks.nl/.

[16] A. Sayah, D. Solignac, T. Cueni, and M.A.M. Gijs. Development of novel low temperature bonding technologies for microchip chemical analysis applications. *Sensors and Actuators*, 84:103–108, 2000.

[17] Zhi-Xiong Xiao et al. Silicon-glass wafer bonding with silicon hydrophilic fusion bonding technology. *Sensors and Actuators*, 72:46–48, 1999.

[18] F. Pigeon, B. Biasse, and M. Zussy. Low-temperature Pyrex glass wafer direct bonding. *Electronic letters*, 31:792–793, May 1995.

[19] WieWeb software. Achterhoekse molenweg 76, 7556 GN Hengelo, The Netherlands http://www.wieweb.com/.

Chapter 5

Micro cold-stage fabrication

Eight different prototype designs are specified using the results of chapter 2, 3 and 4. The production process is defined and has 7 lithography steps and roughly 100 process steps.

5.1 Prototype design specifications

In section 2.3 a basic design of the micro cold stage, containing no specific dimensions, was presented. Through the minimization of entropy principle, as was discussed in section 3.5, CFHX dimensions have been optimized to have minimum dimensions in combination with a fixed net cooling power of 10 mW, see paragraph 3.5.2. The found optimal design is adjusted in such a way that the micro structure can withstand the applied high pressure using the findings of chapter 4. Both the high- and the low-pressure channels as well as the restriction are provided with pillars to suppress high mechanical stresses inside the fabrication material, see section 4.4 and 4.5.

Since the channels contain pillars, the pressure drop in the flow channels will be higher than the calculated pressure drop in section 3.5. In the worst case, these pillars will also have a negative effect on the heat transfer between high- and low-pressure channel, because they increase the heat resistance between the two channels. However, the pillars increase the heat transfer surface between the high- and low-pressure channel which leads to an increase of CFHX effectiveness. The general effect of the pillars is difficult to predict or to implement into the Matlab [1] model presented in section 3.3.3. It was seen in section 3.5.3, that the relative effect of parameter variations is the strongest on the pressure drop. To compensate for the influence of the pillars on the pressure drop, the height of the channels is increased from 35 μm to 50 μm. The optimum configuration for that height as plotted in figure 3.21 is:

CFHX design specifications

P_{gross}:	14.7 mW	Length CFHX:	25 mm
P_{net}:	12.6 mW	Cover thickness:	150 μm
Channel width:	2.0 mm	Wall thickness:	100 μm
Channel heigth:	50 μm	Side-wall thickness:	150 μm

Besides this 'optimal' design, seven other designs, all based on it, are fabricated. This is done to verify the used optimization model and to investigate the influence of different

Table 5.1: Design parameters of the different cold stages. First two dimensions apply to both the high- and the low-pressure channels. The CFHX channel depth is 50 μm for all designs.

Prototype number	1	2	3	4	5	6	7	M1	M2
CFHX channel width [mm]	2.0	2.0	2.0	2.0	2.0	4.0	5.0	4.0	2.0
CFHX channel length [mm]	25	15	35	25	35	25	35	25	35
Mass flow [mg·s^{-1}]	1.0	1.0	1.0	2.0	2.0	2.0	3.0	2.0	1.0
Δp_H no pillars [Pa]	240	133	355	456	678	235	413	235	600
Δp_L no pillars [Pa]	2842	1527	4253	5202	7917	2782	4921	2782	3500
P_{gross} theory [mW]	14.7	14.7	14.7	29.5	29.5	29.5	44.2	29.5	9.3
P_{net} calculated [mW]	12.6	7.8	13.6	20.0	24.1	25.5	39.6	25.5	5.5

design parameters like the dimensions of the CFHX and the value of the mass flow. The CFHX channel depth is 50 μm for all designs. All relevant design parameters of the prototypes are given in table 5.1. M1 and M2 represent the first stage and the second stage of the two-stage cooler, respectively. The high-pressure value for all prototypes is 80 bar and the low-pressure value is 6 bar, except for cold stage M2 which has a high pressure of 60 bar and a low pressure of 1 bar. In the multistage cooler, the first stage (M1), which has N_2 as a working gas, pre-cools the second stage (M2), which has Ne as a working gas, at a temperature of 97 K. This is needed because Ne has a maximum inversion temperature of 213 K, see table 1.1. Doing so, the second stage reaches a calculated tip temperature of 27 K which is the boiling temperature of Ne at 1 bar [2]. The tip temperature of all other stages is calculated at 97 K which is the boiling temperature of N_2 at 6 bar.

Figure 5.1 depicts a three dimensional schematic, a cross-section and a picture of a cold stage. The cold stage is surrounded by a supportive ring for protection and to simplify handling. This ring is thermally separated from the cold stage. Besides protective purposes, this ring can in later stage be used as a part of a integrated micro vacuum chamber, see chapter 7.

Figure 5.2 shows a cross-section of a cold stage. The dimensions shown are the same for all single-stage prototype designs presented in table 5.1. The wafer thicknesses of the three wafers are chosen in such a way that they agree with both design demands and availability. Bottom, middle and top wafer thickness are chosen at a thickness of respectively 400 μm, 145 μm and 175 μm which results in a total stack thickness of 720 μm. The width of the slit which separates the cold stage from the supportive ring is

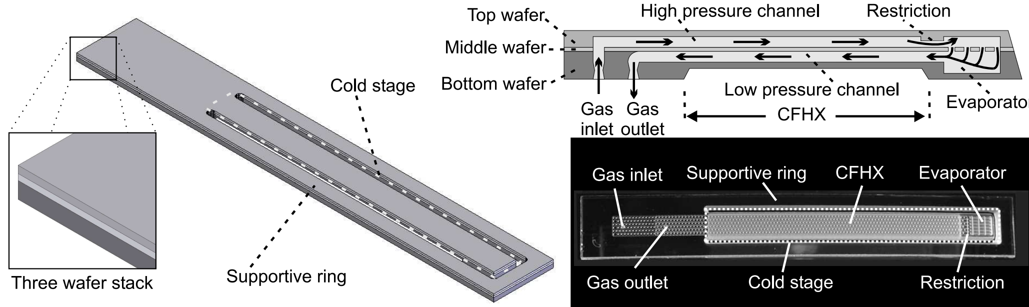

Figure 5.1: Left: 3D schematic of a cold stage. Right top: schematic cross-section of a cold stage. Right bottom: picture of a cold stage.

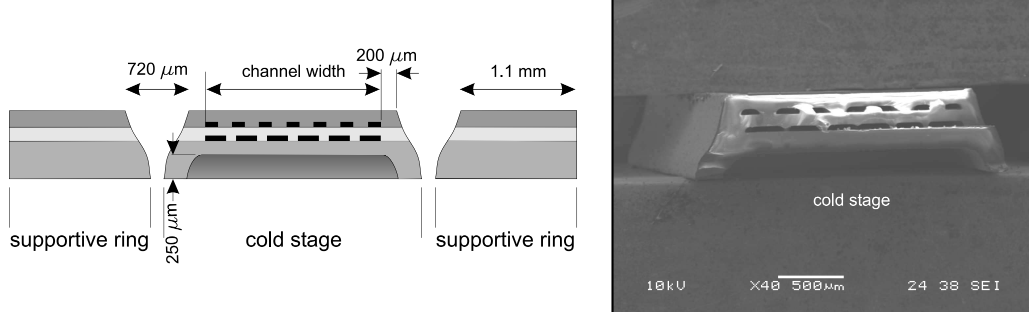

Figure 5.2: Left: schematic cross-section of a cold stage. Right: SEM picture of a cold stage.

chosen at 720 μm, see figure 5.2. Doing so, there should be no problem penetrating the entire stack using the standard powder blast ratio of 1:1. Taking the known accuracy of the powder blasting process used by Micronit [3] into account ($\pm$ 50 μm), the side-wall thickness, which was chosen at a original value of 150 μm in section 3.5.2, is increased to 200 μm. This way the chance of rupturing the gas channel is decreased. A cavity with a depth of 250 μm is powder blasted in the bottom wafer to agree with the dimensions chosen in section 3.5.2 and therefore to reduce parasitic heat loss. At either side a thin wall of about 200 μm is left to increase mechanical strength of the device. The supportive ring has a width of approximately 1.1 mm.

5.2 Process scheme

The micro cryogenic cold stage consists of a stack of three D263T glass wafers [4]. The production process has 7 lithography steps and roughly 100 process steps. Special procedures were developed by Micronit [3] for the handling and processing of the extremely thin wafers. The production process is shown step by step on the following pages. Next to schematics of the cross-sections, 3D models of the cold stage are shown. The orientation of the wafer (bottom up or down) is indicated left to the 3D view. Schematics and detailed (SEM) pictures of the fabricated cold stages can be found in appendix C.

A total of 22 cold stages in 9 different designs (i.e. the ones mentioned in table 5.1 and a design identical to number 5 but with bigger channel pillars) were machined on a single wafer. A batch of 6 wafer stacks is processed at the same, hence 132 micro cold stages in total. Each wafer undergoes a 2 mask process. An overview of the used masks, containing these different designs, can also be found in appendix C.

The production process can be summarized as follows: evaporator slits (A, see next page) are powder blasted in the bottom wafer (thickness 400 μm) which have a depth of about 250 μm. Simultaneously, gas in- and outlet holes (diameter 270 μm) are powder blasted half way through the bottom wafer (B). They meet the holes (C) blasted from the bottom side. Also in this step, the bottom wafer's thickness is locally reduced to about 150 μm to minimize heat conduction through the CFHX (D).

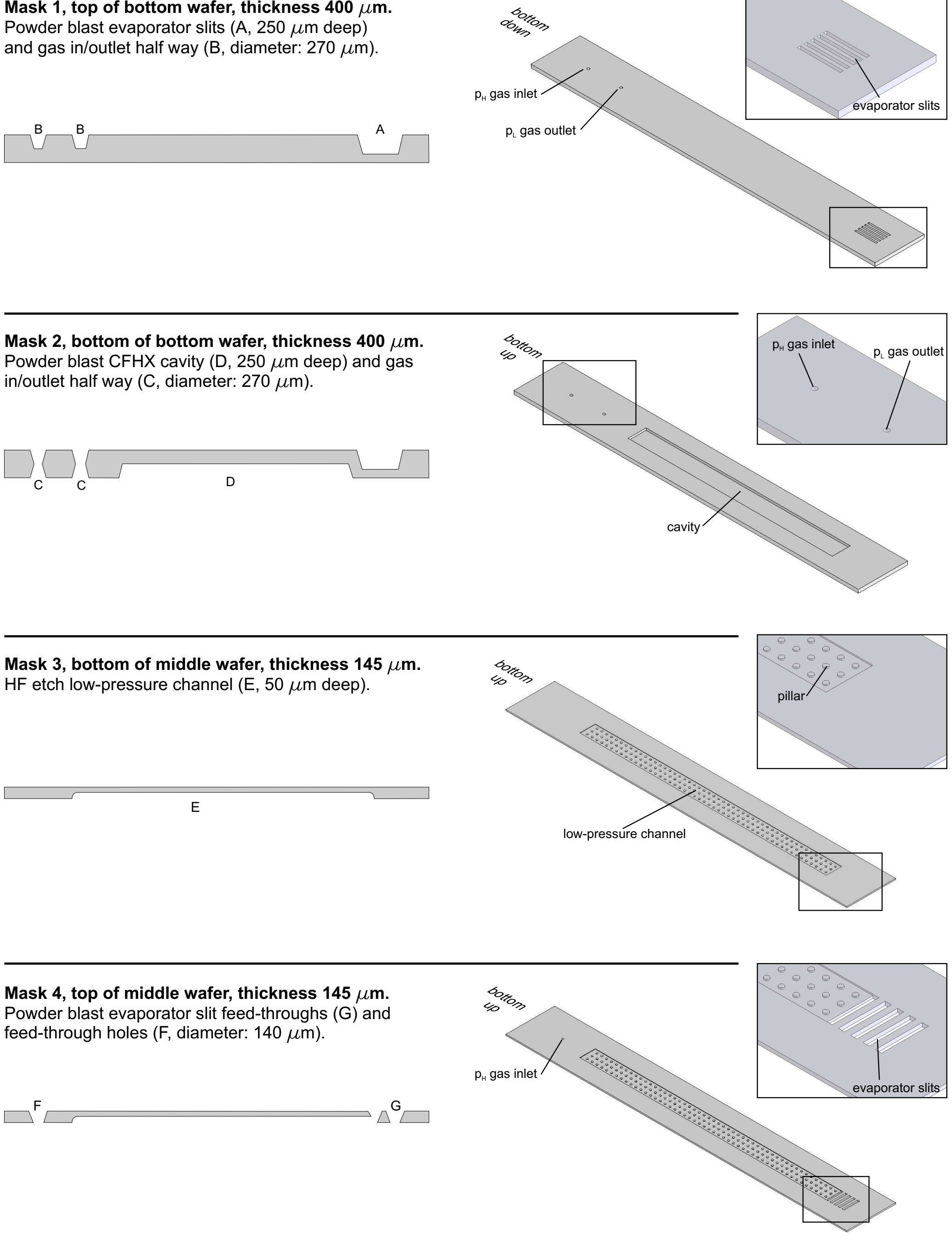
Mask 1, top of bottom wafer, thickness 400 μm.
Powder blast evaporator slits (A, 250 μm deep) and gas in/outlet half way (B, diameter: 270 μm).
B
B
A
bottom down
pH gas inlet
pL gas outlet
evaporator slits
Mask 2, bottom of bottom wafer, thickness 400 μm.
Powder blast CFHX cavity (D, 250 μm deep) and gas in/outlet half way (C, diameter: 270 μm).
C
C
D
bottom up
pH gas inlet
pL gas outlet
cavity
Mask 3, bottom of middle wafer, thickness 145 μm.
HF etch low-pressure channel (E, 50 μm deep).
E
bottom up
pillar
low-pressure channel
Mask 4, top of middle wafer, thickness 145 μm.
Powder blast evaporator slit feed-throughs (G) and feed-through holes (F, diameter: 140 μm).
F
G
bottom up
pH gas inlet
evaporator slits

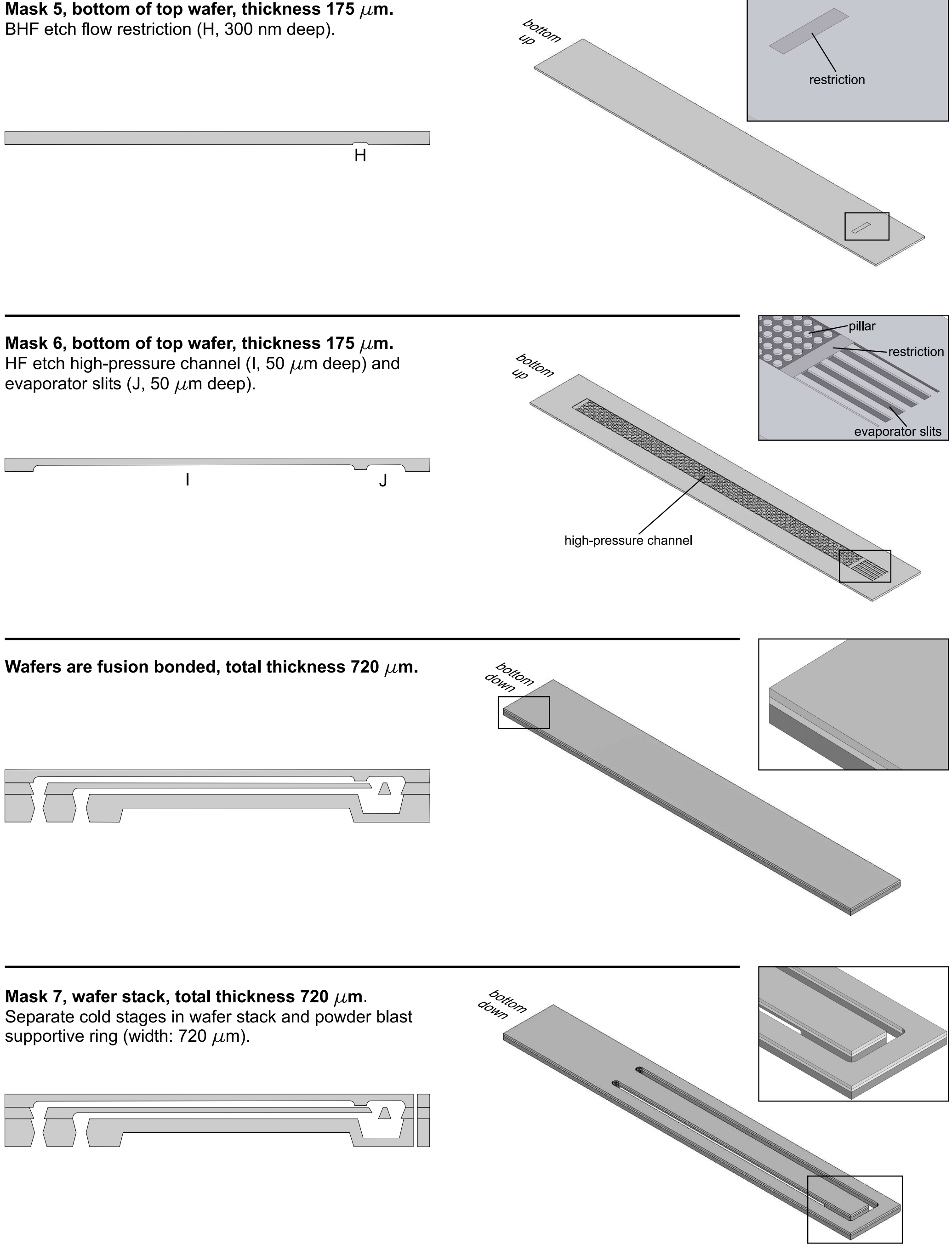

Mask 5, bottom of top wafer, thickness 175 μm.
BHF etch flow restriction (H, 300 nm deep).

Mask 6, bottom of top wafer, thickness 175 μm.
HF etch high-pressure channel (I, 50 μm deep) and evaporator slits (J, 50 μm deep).

Wafers are fusion bonded, total thickness 720 μm.

Mask 7, wafer stack, total thickness 720 μm.
Separate cold stages in wafer stack and powder blast supportive ring (width: 720 μm).

The low-pressure channel (depth 50 μm) is HF etched (E) in the middle wafer (thickness 145 μm) leaving a thin wall of only about 95 μm between the high- and low-pressure sides. The low-pressure channel is supported by pillars with a diameter of 50 μm. Feed-through holes (F) with a diameter of 140 μm and slit feed-throughs for the evaporator (G) are powder blasted in the middle wafer.

In the top wafer (thickness 175 μm), the flow restriction with a height of 300 nm is BHF etched (H). Next, the high-pressure gas channel with a depth of 50 μm (I) and a part of the evaporator (J) is HF etched. The high-pressure channel contains a high density of micro pillars (diameter 200 μm) for support.

Next, the three wafers are fusion bonded to one stack. Alignment of the various plates before fusion bonding was performed using a mask aligner. Fusion bonding parameters for the pressure test samples, described in section 4.3, and the cold-stage samples were the same. Finally, the gaps between the actual cold stages and the protective rings are powder blasted. In this step, the different samples are also separated from each other. After separation, a gold thin film of about 200 nm is sputtered on the cold stages to serve as a reflective shield.

5.3 Prototypes

As was mentioned in the previous section, the production process started with a batch of 6 wafers with a total of 132 micro cold stages. After processing 12 micro cold stages over 6 different design without any defects survived, resulting in a process yield of about 9%. Micronit is confident that this yield can be increased considerably in a next process run. The fabricated micro cold stages are:

Prototype number	**1**	**2**	**3**	**4**	**5**	**6**	**7**	**M**
Number of cold stages	3	2	0	2	1	3	0	1

Unfortunately none of the prototypes numbers 3 and 7 survived the production process. Nevertheless, there are enough samples to verify the operation of the micro cold stage and compare the measurements with the model. Figure 5.3 shows 3 different fabricated prototypes.

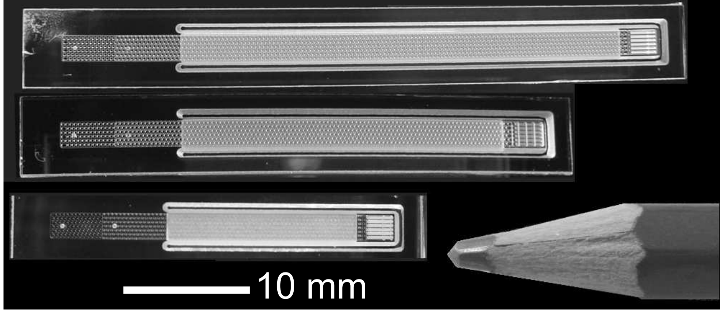

Figure 5.3: Micro cold-stage prototypes. From top to bottom: cold stages number 5, 1 and 2.

5.4 Conclusions

The found optimal design is adjusted in such a way that the micro structure can withstand the applied high pressure. Besides this 'optimal' design, seven other designs, all based on it, are fabricated. The production process is defined and has 7 lithography steps and roughly 100 process steps. The process started with a batch of 6 wafers with a total of 132 micro cold stages. After processing 12 micro cold stages over 6 different design without any defects survived, resulting in a process yield of about 9%.

References

[1] The MathWorks, Inc. 3 Apple Hill Drive, Natick, MA 01760-2098, USA, http://www.mathworks.com.

[2] Cryocomp, version 3.01. Horizon Techonologies, http://www.htess.com/cryocomp.htm.

[3] Micronit Microfluidics BV. Hengelosestraat 705, 7521 PA Enschede, The Netherlands, http://www.micronit.com/.

[4] Schott. 555 Taxter Road, Elmsford, NY 10523, USA, http://www.us.schott.com/.

Chapter 6

Measurements

Cool-down measurements are done to characterize the different cold stages. The net cooling power and the cool-down time are determined. The measurements are compared to the results of the used models described in chapter 3.

6.1 Measurement setup

Measurements on the micro cold stages are performed with the setup shown in figure 6.1. High-purity nitrogen (6.0) gas [1] is supplied from a gas bottle and the high pressure is regulated to 80 bar using a Bronkhorst pressure controller [2]. The inlet mass flow can either be controlled or measured by a mass flow controller (MFC) [2]. The gas is directed through a getter stabilized zeolite filter [3] for further cleaning. The cleaned gas flows through the micro cold stage which is situated inside a vacuum chamber. The vacuum chamber has a glass window so the micro cold stage can be inspected during operation. At the low-pressure side, the pressure is measured using a Druck pressure sensor [4] and the

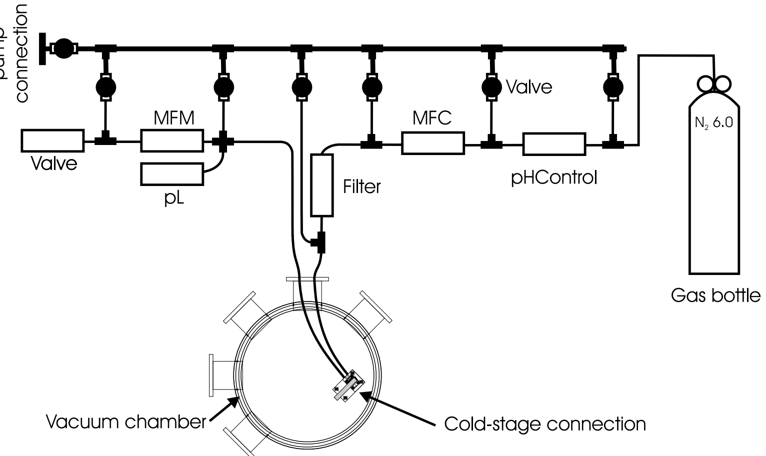

Figure 6.1: Schematic of the measurement setup.

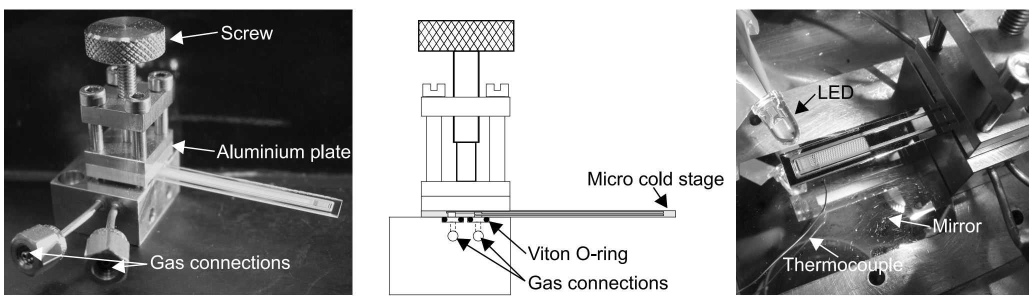

Figure 6.2: Cold stage connection.

outflow is measured using a mass-flow meter (MFM) [2]. A valve at the end maintains an absolute pressure of 6 bar preventing air from the lab to flow into the system. The upper part of the tube system (i.e. the thicker lines in the schematic of figure 6.1) are used for cleaning the system by connecting it to a vacuum pump and pumping the system. This part can be separated from the flow line by means of valves.

The cold stage is connected to the measurement setup via a connection part, see figure 6.2. This part was also used during the pressure tests described in section 4.3. The powder blasted gas in- and outlet of the micro cold stage are placed on top of two small Viton O-rings [5]. The glass device is fixed mechanically by tightening the screw in top. This plug and play system is tested to be leak tight up to 120 bar. The temperature of the cold tip is measured using an Omega E-type thermocouple [6], see figure 6.2 and 6.3. The thermocouple, with a wire diameter of 250 μm, pushes against the evaporator part using its spring force. To minimize parasitic heat loss, no heat sink paste is used between the cold tip and the thermocouple, see figure 6.3.

A mirror situated below the cold stage is used for the placement of the thermocouple and inspection of the cold-stage bottom during operation. A SMD (Surface Mounted Device) resistor which is glued on the cold tip, can be used as a heater to measure the cooling power. The measurement data is processed using a PC equipped with a National Instruments Data Acquisition card and a custom written Labview [7] program. The parasitic heat load on the cold tip because of the thermocouple, the two manganin wires and the SMD resistor is calculated and depends on the chosen emissivity of the manganin wire and resistor surface. Also included in the calculation of this extra loss is the fact

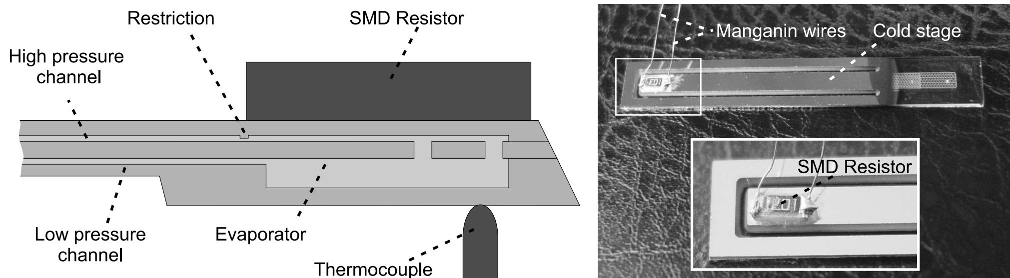

Figure 6.3: Left: on scale schematic of the cold tip with the thermocouple and a SMD resistor. Right: photograph of a cold stage with a SMD resistor.

that bottom of the cooler has a rougher surface than expected because of the powder blasting process. This can increase its emissivity considerably above 0.02. No MLI is used, so the cold stage is directly surrounded by the 300 K vacuum chamber surface. The thermocouple is provided with a thin layer of gold, decreasing its emissivity to ≈ 0.02 [8]. The manganin wires, however, are equipped with a thin plastic isolating layer and the resistor's surface is meanly ceramic. The emissivity of this plastic and ceramic layer is estimated at a best case of 0.2 and a worst case of 0.8, resulting in a total parasitic heat loss due to the measurement setup and rough bottom surface between 6 mW and 10 mW.

6.2 Cooler characterization measurements

6.2.1 Cool down

First measurements were done with micro cold stage number 4 (see table 5.1). This specific cold stage is designed to have a mass flow of about 2 mg$\cdot$s^{-1} making its cooling power relatively large (if compared to cold stage 1) and the cool-down time relatively short. Also clogging of the restriction during cool down (see section 6.3) has less influence, so it is easier to perform multiple tests. Figure 6.4 shows a typical cool-down curve of cold stage 4. On the left, two graphs give the temperature versus time of the cold tip and the mass flow through the system. On the right, the cold-tip temperature against the mass flow is plotted. The right plot also shows two theoretical curves for a restriction height of 305 nm which is the actual (measured) height of the restriction, and a height of 280 nm. The variation of the flow with temperature is caused by the temperature dependence of the gas density and viscosity, see equation 3.41 and appendix A.1.

First of all, it can be seen that the micro cold stage works. It cools down from 300 K to about 100 K in about 800 seconds. At $t \approx 800$ s, the mass-flow curve starts to fluctuate which is an indication that liquid nitrogen is being formed inside the evaporator. It can be seen that the cold stage does not reach the predicted 96 K. The cold-tip temperature is measured with a thermocouple that is connected to the outside of the evaporator, see figure 6.3. It is calculated that the heat resistance of the thin layer of glass and the connection between the thermocouple and the cold stage can easily give a temperature

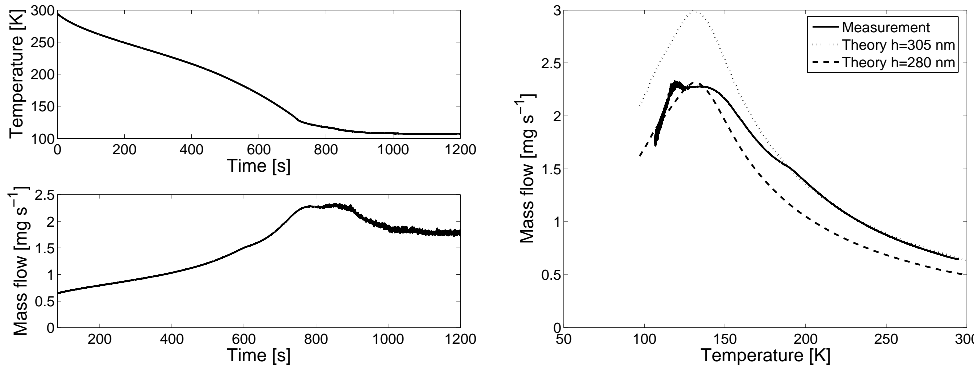

Figure 6.4: Measurement of the cool down of cold stage number 4.

difference of about 15 K. After 1000 s, the cold stage stabilizes at constant tip temperature and mass flow.

In the right graphs it can be seen that the experimental mass-flow curve coincides with the theoretical curve for temperatures above 180 K. At around that temperature, the curve shows a small decrease of the slope. This is an indication that the restriction is getting partly clogged. The clogging of the cold stages will be discussed extensively in section 6.3. Despite this partial clogging, the cold stage further cools down and "follows" another theoretical $\dot{m}$ versus T curve of a somewhat smaller depth. A layer of less than 10 nm height on the surface of the restriction already accounts for the measured effect. It results in a decrease of the mass flow and thus of cooling power. Below a measured TC temperature of about 120 K liquid nitrogen is formed inside the evaporator (flow is fluctuating). This means that there is a large temperature gradient between the measurement point and the evaporator. In addition there is a temperature gradient between evaporator and restriction since the flow is at its maximum, so its temperature should be about 130 K (see figure 6.4) while the evaporator is 96 K (the boiling temperature of N_2 at 6 bar). The liquid nitrogen in the evaporator further cools the restriction, thus affecting the flow as depicted in figure 6.4. The final mass flow through the system is less than the calculated flow of 2 mg$\cdot$s^{-1} because of the clogging.

6.2.2 Cooling power

The net cooling power at N_2(l)-temperature is determined using the SMD resistor, see figure 6.3. When the cold stage has cooled down, the electric power dissipated in the resistor is increased to the point where the cold-tip temperature starts to rise. Figure 6.5 shows a cooling power measurement of cold stage 4. After cool down, the temperature of the cold tip stabilizes at about 108 K and the mass flow at about 1.9 mg$\cdot$s^{-1}.

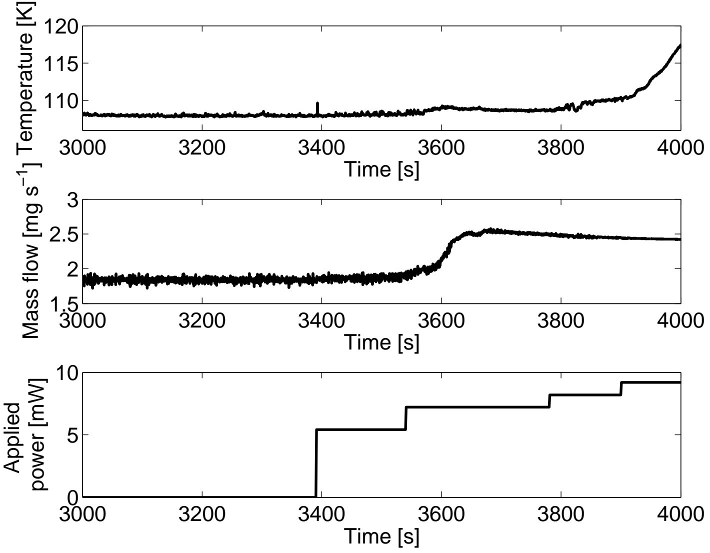

Figure 6.5: Cooling power measurement of cold stage number 4.

At t = 3390 s, the power of the resistor is set to 5 mW. This has no significant influence on the tip temperature. Also the mass flow stays constant and keeps fluctuating meaning liquid nitrogen is still being produced. After 150 seconds (t = 3540 s), the power is increased to 7 mW.

Again the tip temperature remains more or less constant. However, the mass flow curve shows an increase in flow from 1.9 mg·s^{-1} to about 2.5 mg·s^{-1}. It is likely that the resistor power increases the temperature locally at the restriction which increases the flow as can be seen in the theoretical graphs of figure 6.4. An increase in flow results in an increase in cooling power. The cold tip therefore has enough cooling power to keep the evaporator at a low temperature. The resistor power is kept constant for about 4 minutes. Within this period (t $\approx$ 3700 s to $\approx$ 3770 s), the mass flow reduces slightly which is an indication of clogging, see section 6.3. At t $\approx$ 3780 s, the power is increased to 8 mW. Now the cold tip temperature increases slightly, meaning that the applied power is at the break even point with the available cooling power. If the applied power is further increased to 9 mW (at t $\approx$ 3900 s) the tip temperature increases abruptly. Also the fluctuation in the mass flow disappears meaning no more liquid nitrogen is being produced. Using this measurement, the net cooling power of cooler number 4, exclusive parasitic heat loss due to the measurement setup, is estimated at 7.5 mW. Compensating for this parasitic loss, see section 6.1, the cooling power is estimated at a minimum of 13.5 mW and a maximum of 17.5 mW. This is still less than the calculated cooling power of 20 mW, see table 5.1. This difference is probably due to defects of the reflective shield of the cooler, which increase the emissivity. For these first measurements vacuum grease was used to increase heat conduction from the cold tip to the thermocouple. In later measurements the thermocouple was connected without the use of grease.

The method described above is used to measure the cooling power of all fabricated micro cold stages. The results of the measurements are shown in table 6.1. All calculated net cooling powers lie in the compensated net cooling power domain, except for coolers number 4 and 6. The difference in cooling power for number 4 was explained above. The resistor of cooler 6 was not correctly glued to the cooler's tip resulting in a higher surface area increasing the radiative heat load which explains the found difference in cooling power.

It can be concluded from these measurements that all fabricated single cold stages work. Also, the estimated net cooling powers agree fairly well with the calculated amounts. However, due to the influence of the measurement setup, see section 6.1, it is hard to give an accurate value for the net cooling power. Nevertheless, the results are satisfying and it can be concluded that the static BH-model described in section 3.3.3 gives a reliable prediction of the cooling power of a micro cold stage.

Prototype number	**1**	**2**	**4**	**5**	**6**
CFHX channel width [mm]	2.0	2.0	2.0	2.0	4.0
CFHX channel length [mm]	25	15	25	35	25
Mass flow [mg·s^{-1}]	1.0	1.0	2.0	2.0	2.0
P_{gross} theory [mW]	14.7	14.7	29.5	29.5	29.5
P_{net} calculated [mW]	12.6	7.8	20.0	24.1	25.5
P_{net} measured [mW]	3	1	7.5	16	13
P_{net} compensated [mW]	11 $\pm$ 2	9 $\pm$ 2	15.5 $\pm$ 2	24 $\pm$ 2	21 $\pm$ 2

Table 6.1: Design parameters and measured cooling powers of the different cold stages.

6.2.3 Cool-down time and comparison with the dynamic model

The dynamic model [9] presented in section 3.4 is used to predict the cool-down time of cooler number 4. As was seen in the previous section, the clogging effect has an influence on the mass flow through the system which reduces the available cooling power. This affects the cool-down time of the cold stage. To compare a measurement with the dynamic model, a measurement was done and the measured mass flow is used as an input parameter in the dynamic model. Also a correction is made for the parasitic heat losses induced by the measurement setup. Figure 6.6 shows the results of both measurement and model. As can be seen both the calculated and measured cool-down time are about 950 s. Also both profiles coincide to a great extent. The difference in final temperature is (again) due to the temperature gradient between evaporator and measurement point. Also, it has to be said that the influence of parasitic heat loss due to the measurement setup (thermocouple, heater and manganin wiring) on the model is considerable. Relatively small changes in these parameters can have a large influence on the calculated results. Therefore, the dynamic model can be used as a guideline for cool-down calculations.

6.3 Clogging

6.3.1 Clogging phenomenon

As was mentioned in the previous sections, clogging of the restriction has a critical influence on the operation of the micro cold stage. The measurements shown in section 6.2 show relatively little influence of this clogging effect. However, many measurements have been done where the clogging is much more severe. It is seen that often during the first cool-down cycles, the cold stage clogs to such an extent that the tip does not cool down to N_2(l)-temperature.

In the measurement setup, high-purity nitrogen gas 6.0 is supplied from a gas bottle,

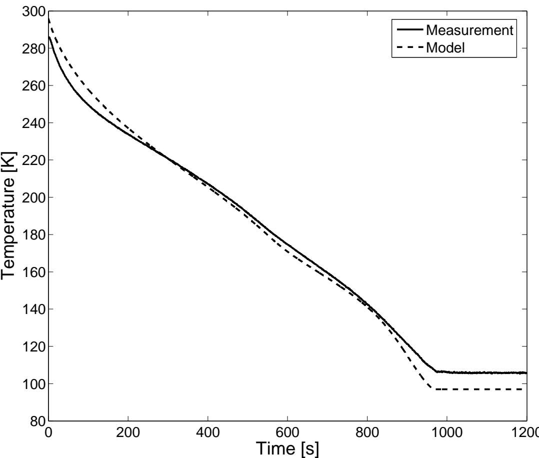

Figure 6.6: Measurement comparison to dynamic model calculations. The solid line represents the measurement and the dashed line shows the model.

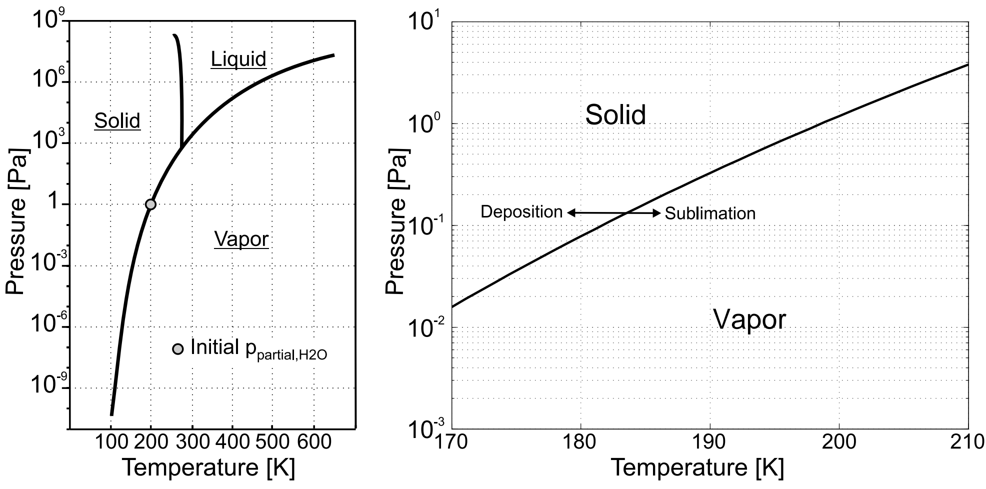

Figure 6.7: Left: phase diagram of pure water. Data above 200 K is taken from [10]. Data below 200 K is calculated using the Clausius-Clapeyron equation [11]. Right: magnification of a smaller domain of the phase diagram.

see figure 6.1. According to the data sheet [1], the gas is contaminated with water, oxygen, carbon hydrates, carbon monoxide, carbon dioxide and hydrogen all with impurity levels in the ppm range. According to the specifications of the getter stabilized zeolite filter [3], the outlet contamination should be below 1 ppb. Therefore, it is expected that the contamination in the cooler is determined by the amount present at start-up. To minimize this initial contamination in the system, the setup is cleaned by pumping and heating. Through calculation [12, 13], the initial pressure inside the cold stage was estimated at about 1 Pa. In many of our experiments, the temperature at which the restriction starts to clog appeared to lie around 200 K. From the relevant fluids, water is the only one that has a phase transition around that temperature at about 1 Pa. Figure 6.7 shows the phase diagram of pure water. It can be seen that water changes its phase in the deposition from vapor to solid at about 200 K and 1 Pa. The clogging phenomenon is investigated thoroughly to realize stable operation of the micro cold stages in future applications.

6.3.2 Uncontrolled clogging at relative high partial water pressure

Since the channel height of the restriction is only 300 nm, it can clog abruptly if the deposition temperature at the local partial pressure of water is reached. A measurement in which the restriction is severely clogged is shown in figure 6.8. During the first stage of the cool-down process (A to B in figure 6.8), the mass flow increases with decreasing tip temperature according to the theory which is also shown in the right graph. At a measured temperature of about 204 K the mass flow drops drastically (point B). At this point, apparently the restriction has reached the deposition temperature of water which now changes its phase from vapor to solid. The decrease of mass flow caused by the clogging, directly leads to a decrease in cooling power. At point C, the parasitic heat load

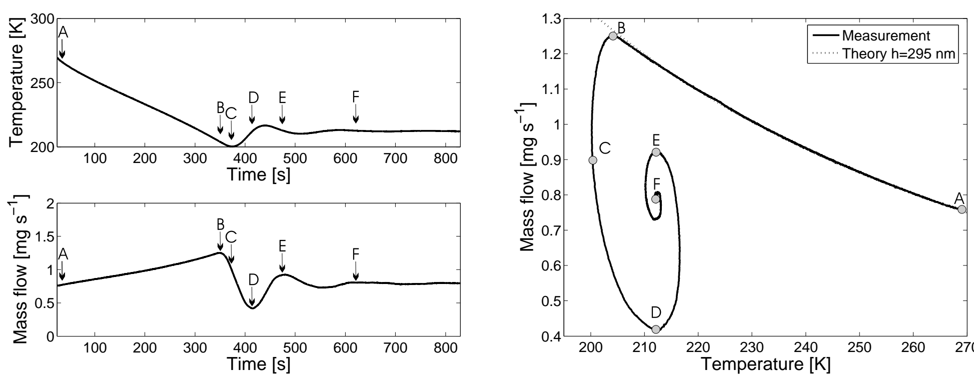

Figure 6.8: Measurement of a cool-down cycle of cold stage 4.

exceeds the cooling power and the cold stage warms up (C to D). When the temperature of the restriction reaches the sublimation temperature again, the contamination returns to the vapor phase and the restriction partly de-clogs, increasing again the mass flow (D to E). The increase of the flow goes hand in hand with an increase of cooling power. At some point, the cold stage has gained enough flow to cool down again. However, at this point this decrease in temperature again results in deposition of water. This process continues to an equilibrium (F) in which the limited cooling power caused by the restricted mass flow equals the parasitic heat load on the tip.

The partial pressure of water inside the nitrogen gas, in this experiment, can be determined using the measured deposition/sublimation temperature and the phase diagram of water shown in figure 6.7. However, during this measurement the deposition temperature in point B, which is about 204 K, does not seem to agree with the measured deposition/sublimation temperatures in the points D, E and F, which are about 212 K. This difference can be explained as a result of the changing temperature gradient between the measured thermocouple (TC) temperature and the actual temperature near the restriction, see figure 6.3. The cooled low-pressure gas flows through the evaporator at a relatively high speed (in the order of meters per second) particularly cooling the end of the evaporator where the gas is forced from the top channel to the lower channel, inducing high heat transfer between gas and wall. Therefore, the actual restriction temperature will be higher in point B than the measured TC temperature. A temperature difference of 8 K is plausible according to calculations. Since the net cooling power is decreasing from point B to D, the temperature gradient over the evaporator will fade. After point D the evaporator temperature varies slightly with changing mass flow and finally comes to an equilibrium (see figure 6.8). The temperature gradient over the evaporator stabilizes and the final temperature is about 212 K. According to the phase diagram the partial pressure of water at this temperature is about 4.7 Pa which is the same order of magnitude as the initial partial pressure mentioned in section 6.3.1.

6.3.3 Uncontrolled clogging at relative low partial water pressure

As shown in the previous section, if the partial pressure of water is about 5 Pa ($\approx$ 0.6 ppm), the restriction gets clogged and the mass flow is reduced to such an extent that the cold tip does not cool down to liquid nitrogen temperature. In the measurement shown in figure 6.9, the contamination of water has been reduced by pumping, flushing and heating, to enable cool down of the cold tip to liquid nitrogen temperature. The experimental mass-flow versus temperature curve corresponds to theory (i.e. a measured restriction height of 295 nm for this specific cold stage, see right graph of figure 6.9) for temperatures above 200 K. At around that temperature ($p_{partial,H_2O} = 1$ Pa ≈ 0.1 ppm), the mass-flow versus temperature curve shows a small decrease of the slope compared to theory. This is an indication that the restriction is getting partly clogged (point A). A layer of a few nanometers on the surface of the restriction already accounts for the measured effect. It results in a decrease of the mass flow and thus of cooling power. Nevertheless, the cool down continues and below about 120 K, the mass flow starts to fluctuate (point B). This mass-flow fluctuation indicates that liquid is being formed inside the evaporator. It also means that there is a relatively large temperature gradient from the evaporator to the flow restriction since at 6 bar nitrogen boils at 96 K. The liquid nitrogen in the evaporator further cools the restriction, thus affecting the flow as depicted in figure 6.9. In the left graph of this figure, it can be seen that the measured temperature does not reach the predicted 96 K but is about 110 K. This temperature is measured with a thermocouple connected to the outside of the evaporator. The temperature difference of 14 K is caused by the thermal resistance formed by the thin layer of glass and the connection between the thermocouple and the cold stage.

From point C, the cold tip stays in a semi stable situation with constant flow and temperature. In this phase, there is a constant temperature gradient over the CFHX from about 100 K at the cold tip to 300 K at the warm end, see right plot in figure 6.10. The coldest part of the CFHX with a temperature below 200 K now acts as a water filter. Here, water molecules deposit on the CFHX wall and because of the relative large CFHX volume (the flow channel is 50 μm high and 2 mm wide), this does not affect the mass flow. The partial pressure of water inside the nitrogen gas is reduced from 1 Pa at 200 K to about 10^{-10} Pa at 100 K which corresponds to a contamination of only about

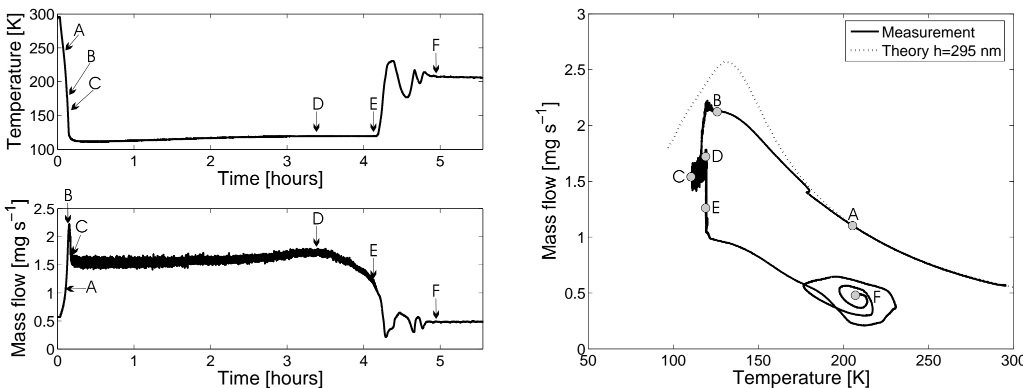

Figure 6.9: Cool down measurement of cold stage number 4.

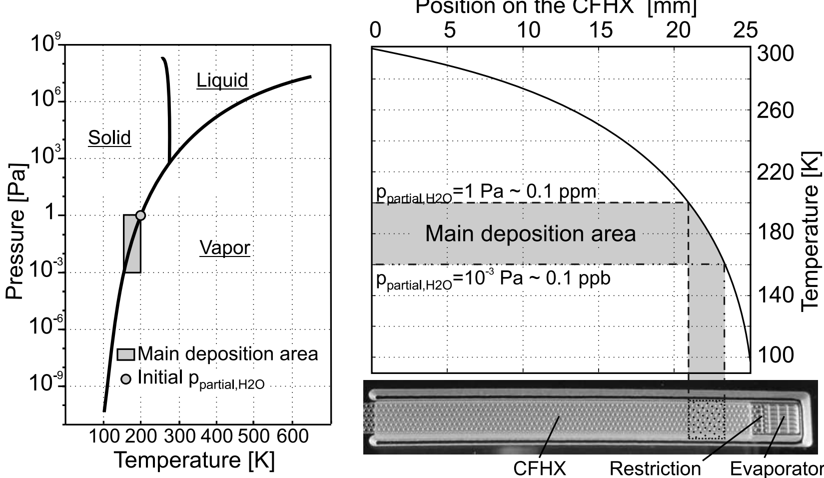

Figure 6.10: Left: phase diagram of water. Right: calculated temperature profile of the CFHX and a schematic representation of the main deposition area. Right bottom: photograph of a cold stage.

10^{-11} ppm, in other words nearly zero, see figure 6.10. A large portion of the water, about 99.9%, deposites in the CFHX area with a temperature between 200 and 160 K (main deposition area, see figure 6.10). From this point, the water contamination inside the nitrogen gas has decreased by a factor of 10^3 (i.e. from 1 Pa to 10^{-3} Pa). From point C to D in figure 6.4, the temperature of the cold tip increases slightly because of condensation of residual air molecules in the vacuum space at the outside of the cooler. The surface of the cold stage is covered with a reflective gold layer of which the emissivity increases.

During a long period of time (in this experiment 3 hours from point C to D) nearly all water molecules deposit inside the main deposition area creating a thin layer of ice crystals on the CFHX surface. As this layer grows thicker, at some point the cohesion between the

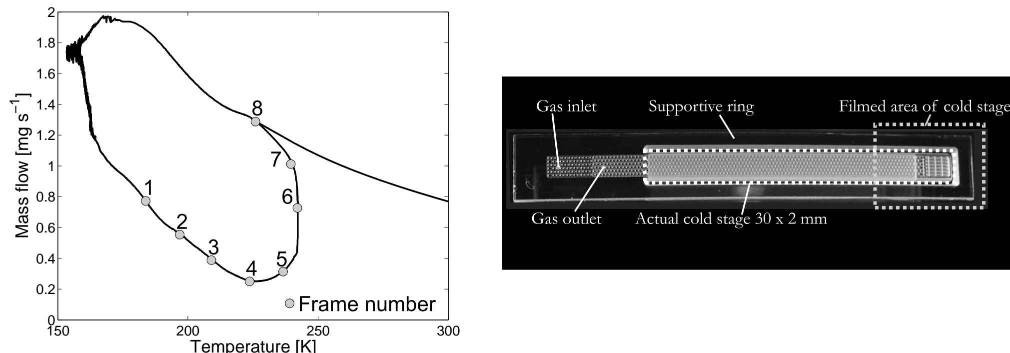

Figure 6.11: Left: measurement data of movie shown in figure 6.12. Right: photograph of a cold stage.

crystals becomes that weak that they disconnect and diffuse through the CFHX forced by the flow. When they reach the restriction, they get stuck inside and block the flow (point D to E). The mass flow decreases and as a result the cooling power drops. At a certain point (t = 4.2 hours, point E), the cooling power can no longer compensate for parasitic heat losses and the tip temperature increases. Due to this temperature increase, the mass flow decreases further and the cold tip heats up again converging to a stable situation (F) as was seen in the previous section.

In a similar experiment, a cold stage was used without a gold layer on the outside so that it was possible to look inside the glass cooler during operation. The measurement data of this experiment is shows in figure 6.11. Figure 6.12 shows eight frames of a video that was taken during cool down, showing the deposited water inside the cooler. In this experiment, as in the previous one, most of the water deposits in the main deposition area of the CFHX during a long period of time. As a result of the clogging of the restriction, the mass flow drops and the cold stage warms up (point 1). In the corresponding frame no solid water can be seen in the filmed area. As the evaporator warms up, the temperature gradient over the CFHX decreases and the main deposition area moves toward the cold tip. This is visualized in figure 6.12 by subtracting frame 1 from frame 2. At 2, the temperature of the evaporator has increased to such an extent that this transition zone enters the evaporator. The evaporator temperature rises further to point 3. Now a large

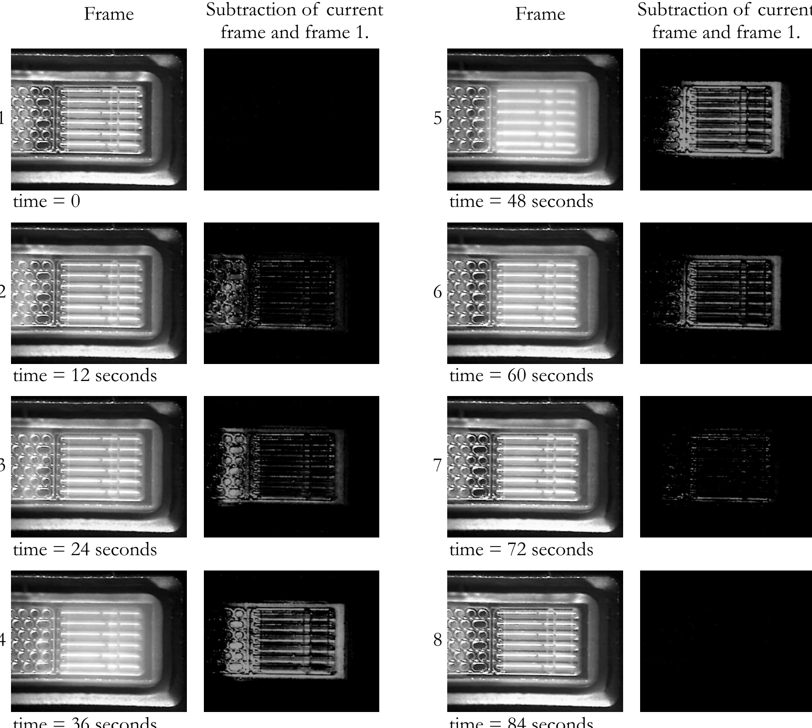

Figure 6.12: Eight different frames of a movie taken from the tip of the cold stage during operation. Next to every frame a subtraction of the current frame and frame 1 is depicted. The measurement data of each frame can be found in figure 6.11.

amount of solid water has moved from the CFHX into the evaporator. The clogging of the restriction has now reached a maximum (point 4, flow is minimum). A cloud of deposited water can now be seen in the movie frame. From 5 to 6 and 7, the evaporator reaches the sublimation temperature and the deposited water transitions back to vapor and is dragged away with the flow. The system now contains no more solid water molecules and the mass flow has returned to its original value so the cold stage can cool down again (point 8). In contrast to the measurement shown in figure 6.9, a stable end situation is not reached. This is because there is no reflective shield on the evaporator, increasing the local parasitic heat loss and therefore the end-point temperature would lie above the local sublimation temperature of water.

6.3.4 Clogging at controlled temperature

Another measurement was done with the restriction kept at a constant set-point temperatures while it clogged, see figure 6.13. This way the temperature of the restriction remains about constant as does the local partial pressure. Measurements are done at 6 different set-point temperatures. A temperature correction on the measured (TC) temperature is made to estimate the actual restriction temperature. Doing so, it is possible to find clogging times, total water volume which deposits and the volume that actually deposits inside the restriction. All found data is given in table 6.2. The initial partial water pressure is calculated using the transition temperature below which water does deposit in the restriction and above which it does not. This temperature is approximately 201 K which gives a partial pressure of about 1 Pa.

The clogging time given in table 6.2 is defined as the time between the point where the temperature reaches the set clogging temperature to the point where this temperature rises again. The water inside the nitrogen gas will deposit inside the CFHX (and is thus filtered out) to a level determined by the partial pressure that is determined by the set-point temperature, also given in table 6.2. This explains the increasing clogging time with decreasing restriction temperature. During the clogging time an estimation of the total water volume deposited in the cold stage can be made using the clogging time, the partial water pressure and the measured mass flow. The lower the clogging temperature,

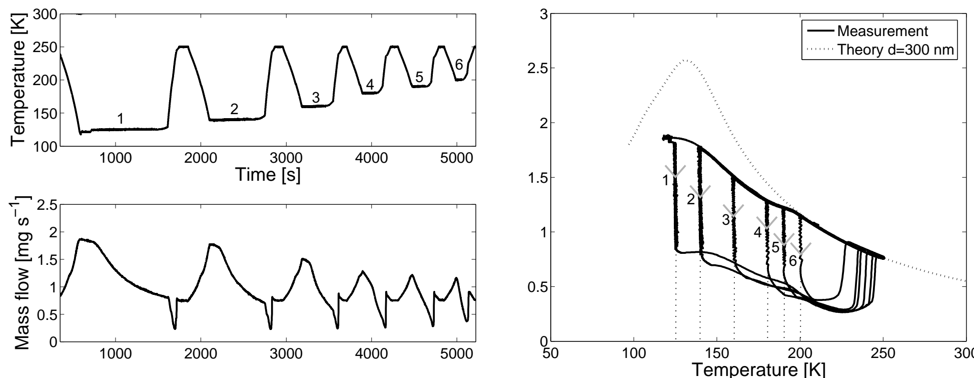

Figure 6.13: Measurement data of clogging cycles at constant set-point temperature

the larger the filter area and clogging time and hence the higher the water volume that is deposited inside the cold stage. It is assumed that water is deposited inside the restriction in a uniform way, leaving mono layers of water molecules at the restriction walls. These mono layers reduce the restriction height which in the calculations is derived from the measured mass flow. This way the clogged volume of the restriction is calculated. As may be expected, this volume is more or less constant for all 6 different clogging temperatures (about $1.4 \cdot 10^3$ μm^3, see table 6.2). The ratio between the total water volume deposited and water volume deposited inside the restriction obviously increases if the restriction temperature approaches the deposit temperature of the initial partial water pressure which is about 201 K.

If we now compare the measurement done at a clogging temperature of 113 K (the closest to N_2(l) temperature) with the measurement done in the previous section, see figure 6.9, a few differences catch the eye. First of all the difference between clogging times seems rather large. In figure 6.9 the clogging time takes several hours whereas in measurement 1 of table 6.2 it only takes about 16 minutes. In the first case, where there is no temperature control, liquid nitrogen is being produced inside the evaporator. Since there is no forced heat load on the cold tip this liquid nitrogen will fill the evaporator and enter the low-pressure line of the CFHX, see figure 6.3. As a result, a part of the high-pressure line, situated in front of the restriction will also cool down to the same temperature as the restriction. Since the temperature of this CFHX part is more or less constant, also the partial pressure of water will be constant. In other words, it acts as a high-efficiency water filter increasing the clogging time. In the case of measurement 1 of table 6.2 the temperature is controlled (just) above liquid nitrogen temperature. Therefore, the temperature decreases constantly from the high-pressure CFHX line to the location of the restriction. Hence, the restriction is always the coolest point, filtering the water to the corresponding partial pressure and clogging the restriction in a higher tempo.

Another unexpected difference is the difference in cool-down curve which is odd since we expect more or less the same amount of water contamination inside nitrogen gas. The mass flow of figure 6.9 decreases less during the cool down and comes to a higher value. This difference can be explained due to a very small difference in initial partial water pressure and thus clogging temperature which for that matter is impossible to measure with this setup. If both measurements are compared, the contamination of the measurement in figure 6.9 is ≈ 0.6 Pa (using a corrected temperature of about 193 K) and the contamination of the measurement in figure 6.13 is ≈ 1.3 Pa (using a corrected temperature of about 201 K). Though this difference seems very small, it is already

Clogging cycle number:	**1**	**2**	**3**	**4**	**5**	**6**
Measured set-point temp. [K]:	125	140	160	180	190	200
Corrected set-point temp. [K]:	113	130	150	172	183	194
Partial H_2O pressure [Pa]:	$8 \cdot 10^{-9}$	$2 \cdot 10^{-6}$	$3 \cdot 10^{-4}$	0.02	0.1	0.6
Clogging time [min]:	16.1	9.7	4.5	2.8	3.2	1.5
μm^3 of H_2O dep.:	$5.7{\cdot}10^4$	$3.4{\cdot}10^4$	$1.1{\cdot}10^4$	$0.8{\cdot}10^4$	$0.7{\cdot}10^4$	$0.2{\cdot}10^4$
μm^3 of H_2O dep. in restr.:	$1.5{\cdot}10^3$	$1.4{\cdot}10^3$	$1.3{\cdot}10^3$	$1.3{\cdot}10^3$	$1.4{\cdot}10^3$	$1.4{\cdot}10^3$
Fraction dep. in restriction:	0.03	0.04	0.11	0.16	0.20	0.61

Table 6.2: Clogging data taken from the measurement shown in figure 6.13. The fifth row gives the total volume of H_2O particles deposited during the clogging event. The next row gives the H_2O volume deposited in the restriction. The last row gives the ratio between these two. The total volume of the restriction is about $4.2{\cdot}10^4$ μm^3.

enough to account for the measured difference in mass flow during the cool-down curve. In other words it is seen that a slight difference in measured clogging temperature and thus estimated $p_{partial,H_2O}$ has a relatively large impact on the cool-down curve.

6.3.5 Clogging prevention

The clogging of MEMS based micro coolers was investigated. Water molecules deposit inside the CFHX and deposited ice crystals migrate to the flow restriction, thus blocking the flow and reducing the cooling power. As a result, the cold tip warms up and the water deposition area moves to the evaporator part. In future, these micro coolers will be combined with small compressors thus establishing closed-cycle micro refrigerators. By carefully pumping and purging these devices prior to closing, the amount of residual water can be limited. The remaining water will be trapped in the CFHX and can be sublimated back to vapor as described above. A small heater at the cold tip can be applied to force this process. We anticipate that in a few steps all water present in the system can be moved through the cold stage and collected at the warm end by adequate filtering. In this respect, the application of sorption compressors is very attractive [14–16].

6.4 Multi-stage micro cooler

6.4.1 Design and measurememts

Multi-staging is needed in JT-based coolers, if a cryogenic temperature much lower than about 80 K is desired. Although the design of a multi-stage cold tip is beyond the scope of this project, one was fabricated and tested. However, its design is not optimized like was done with the single stage micro cooler. In a multi-stage cooler two separate Linde-Hampson cycles [17, 18] are thermally connected at the so-called pre-cooler point, see figure 6.15. The cooling power of the first stage is used to pre-cool the high-pressure gas of the second stage to the first stage's cold tip temperature. This improves the available gross cooling power at the second cold tip by creating a larger enthalpy difference in the gas, see figure 1.1. In general, the gas which is used in the second stage has a maximum inversion temperature (see section 1.2 [11]) which lies below room temperature so pre-cooling is necessary to obtain a cooling effect at the second stage. The fabricated micro multi-stage cold tip works with nitrogen and neon gas. The first stage is identical to N_2 single stage number 6. Dimensions and cycle parameters are given in table 6.3.

Figure 6.14 shows a picture of the fabricated cooler. Tests are done using the setup shown in figure 6.15. As can be seen, there is no filter used in the neon cycle. It is expected that all contaminant gases in the neon gas will freeze or deposit inside CFHX I, the pre-cooling part and/or CFHX II.

	Channel width [mm]	Channel length [mm]	Mass flow [mg·s^{-1}]	P_{gross} [mW]	P_{net} [mW]	T_{tip} [K]
First stage, CFHX	4.0	25	2.0	30	25	97
Second stage, CFHX I	2.0	25	1.0	-	-	-
Second stage, CFHX II	2.0	10	1.0	9	5	27

Table 6.3: Design parameters of the multi-stage micro cold tip. The depth of all channels is 50 μm. Height of the restriction of both stages is 300 nm.

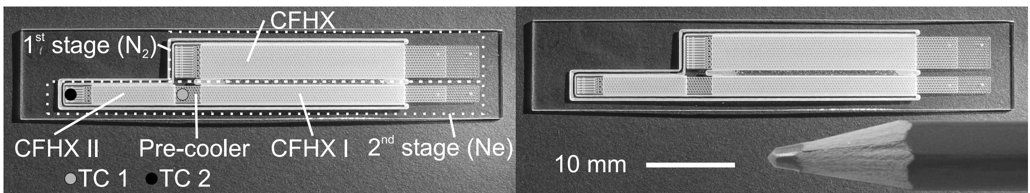

Figure 6.14: Multi-stage micro cryogenic cooler.

First measurements done with the 2-stage micro cold stage showed that the cold tip is not able to cool down to cryogenic temperatures by itself. Calculations done on the multi-stage design included only simulations of the cold tip at cryogenic temperature (i.e. the 1st stage at 97 K and the 2nd at 27 K) in a stationary situation. However, at the initialization, the entire micro cooler is at ambient temperature. If the gas flow is initialized, only the N_2-stage has a cooling power since for Ne, the gas expansion is above its inversion temperature. In other words, the N_2-stage has to cool down both the 1st and 2nd stage and has to compensate for the parasitic heat losses of both stages. Measurements showed that the fabricated multi-stage cooler was not able to do this.

To overcome this problem, the cold tip is surrounded by a cooled radiation shield to reduce radiation losses. The shield is cooled by liquid nitrogen. A measurement done, including this shield, is shown in figure 6.16. Although the operation of the micro cold stage is of course influenced by the radiation shield, some interesting observations are made. The fluctuation in the mass flow graph of the first stage shows that the N_2-stage cools down to liquid nitrogen temperature. However, the pre-cool temperature of the neon gas which is measured at point TC 1, see figure 6.14, stagnates at about 140 K. This means there is a relatively high heat resistance from the first stage cold tip to the pre-cooler. The consequence is that Ne in the second stage is not pre-cooled at the expected 100 K, as was done during calculations, but at this much higher temperature. This has a large influence on the specification of CFHX II and thus on the cooling power of the

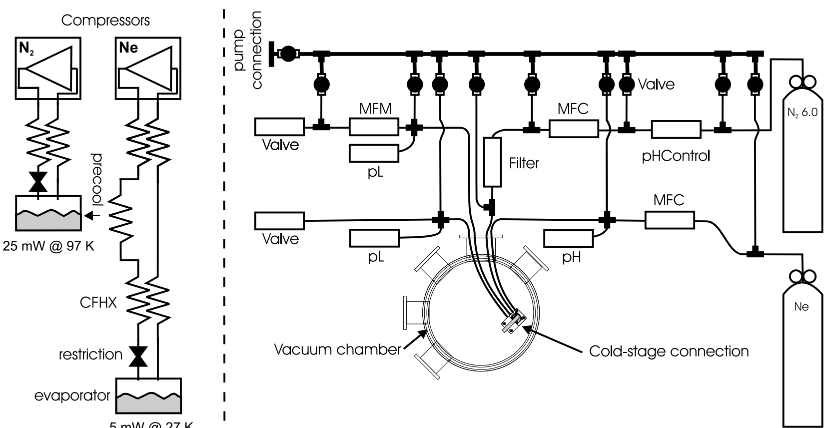

Figure 6.15: Left: schematic of the multi-stage cold stage. Right: measurement setup for multi-stage measurements.

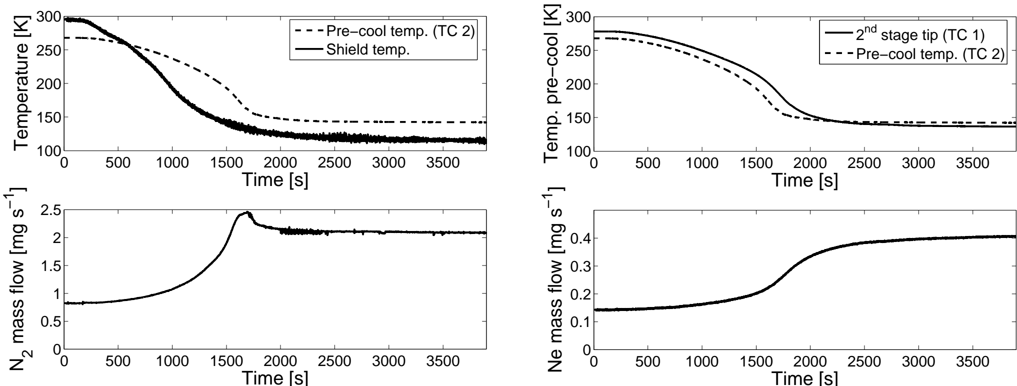

Figure 6.16: Multi-stage measurement. The second stage tip temperature is measured at point TC 1 and the pre-cool temperature is measured at point TC 2, see figure 6.14.

second stage. Nevertheless, the neon gas is pre-cooled below its inversion temperature of 213 K so it shows some cooling effect, see figure 6.16. It can be seen that the temperature of the 2nd stage cold tip drops below the pre-cool temperature although it is not much. The Ne mass flow stabilizes at a value about 0.4 mg·s^{-1}. As was expected the 2nd stage shows no sign of clogging. All gas contaminations are frozen/deposited inside CFHX I, the pre-cooler and/or CFHX II.

6.4.2 Multi stage recommendations

Design optimization.
As was mentioned before, the design of the presented multi-stage cooler was not optimized. An optimization study, similar to the one presented in section 3.5, should be done to reach maximum COP in combination with minimum cold stage dimensions. The tricky thing is, as was seen during the measurements, that the multi-stage cooler should not only be simulated during its (final) cold and stable situation, but also the cold-down behavior should be investigated. The 1st stage has to be powerful enough to cool down both itself and the second stage below the inversion temperature of the gas used in the 2nd stage.

Fabrication process.
During the fabrication process of the presented multi-stage cold tip, the CFHX of the 1st stage was not separated from CFHX I of the 2nd stage. This is, according to Micronit [19], due to lithography problems with the current mask. Because of this thermal connection between the two CFHXs, extra parasitic heat loss (conduction and radiation) is induced. Also the temperature profiles of both the CFHXs are influenced by one another which can have a negative effect on the CFHX specifications. This problem can be solved by using a different mask design and/or adjusting the powder blasting process for this specific step.

Temperature gradient from cold tip to the pre-cooler.
As was seen in the measurements presented above, the temperature gradient from the 1st stage cold tip to the pre-cooler part is considerable and can go up to about 40 K. This has a large influence on temperature profile and thus on the losses in CFHX II. Also a lot less enthalpy chance of the neon gas is achieved which directly results in less gross cooling power at the 2nd stage cold tip. The multi-stage cooler has to be provided with a good thermal link from 1st stage cold tip to the 2nd stage pre-cooling point so that the neon is pre-cooled to about 100 K. This can, for example, be done by depositing a "thick" layer of metal (e.g. copper) from cold tip to pre-cooler or bonding a piece of silicon at this spot.

Influence of measurement setup.
It was seen that, during the measurements of the single stages, the measurement setup had an influence on the operation of the cold stages. The effect of the setup appeared to be even bigger for the measurements done with the multi-stage cooler. The parasitic heat load from the different thermocouples, TC 1 and TC 2 in figure 6.14, often seemed to be very high. The heat load of the thermocouples in cold and stable situation is estimated at, TC 1: 3.5 mW and TC 2: 5 mW. For TC 2, the heat load approaches the total available calculated net cooling power. One of the solutions for this problem is to heat sink the thermocouples to a cold platform. This way the heat load can be minimized. Another, maybe more elegant solution, is to integrate the fabrication of temperature sensors in the cold-stage construction process. Instead of using gold as a reflective shield, platinum could be used. Inside the thin platinum layer, tiny resistors can be etched and used as temperature sensors.

6.5 Conclusions

Five different designs of single-stage micro coolers were tested. All of the tested designs cooled down to liquid nitrogen temperature. Cooling power measurements indicate that the micro cold stages suffer from parasitic heat loads induced by the measurement setup. Results show that the expected cooling powers are located within the measured net cooling power domain. It can be concluded that the static BH-model, that was used, gives a reliable prediction of the net cooling power of a micro cold stage.

Critical in the micro cooler's operation is the deposition of water molecules that migrate to the restriction and block the flow. This clogging phenomenon was investigated thoroughly and provided significant insight into the way this clogging develops, and opens possibilities to realize stable operation.

References

[1] Hoek Loos. http://www.hoekloosonline.nl/xgis/pib/Stikstof60scientific.pdf.

[2] Bronkhorst High-Tech B.V., Nijverheidsstraat 1A, 7261 AK, Ruurlo, The Netherlands, http://www.bronkhorst.nl.

[3] Saes Getters. Viale Italia 77, 20020 Lainate (Milan), Italy, http://www.saesgetters.com/.

[4] Druck Ltd., Fir Tree Lane, Groby, Leicester, LE6 0FH, England, http://www.druck.com.

[5] Eriks, Hassinkweg 16, 7556 BV, Hengelo, http://www.eriks.nl/.

[6] Omega Engineering, Inc., One Omega Drive, Stamford, Connecticut 06907-0047, USA, http://www.omega.com.

[7] National Instruments Corporation, 11500 N MoPac Expwy, Austin, TX 78759-3504, USA, http://www.ni.com.

[8] A. Bendavida and P.J. Martina and L. Wieczorekb. Morphology and optical properties of gold thin films prepared by filtered arc deposition. *Thin Solid Films*, 354:169–175, 1999.

[9] J. Koning. *Cryogenic micro cooling, a study into dynamic modeling & wafer level vacuum packaging*. University of Twente, 2006. M.Sc. thesis.

[10] Cryodata Inc. http://www.cryodata.com.

[11] C.B.P. Finn. *Thermal Physics*. Chapman & Hall, 2nd edition, 1993. ISBN 0-412-49540-6.

[12] A. Roth. *Vacuum technology*. Elsevier Amsterdam, 3nd edition, 1990. ISBN 0-444-86027-4.

[13] E. Suurmeijer and T. Mulder and J. Verhoeven. *Basisboek vacuümtechniek*. Krips, Meppel, 2nd edition, 2000. ISBN 90-9013776-9.

[14] G. Wiegerinck. *Improving sorption compressors for cryogenic cooling*. PhD thesis, University of Twente, 2005.

[15] J. F. Burger, H. J. M. ter Brake, H. Rogalla, and M. Linder. Vibration-free 5 K sorption cooler for ESA's Darwin mission. *Cryogenics*, 42:97–108, February 2002.

[16] G.F.M. Wiegerinck, J.F. Burger, H.J. Holland, E. Hondebrink, H.J.M. ter Brake, and H. Rogalla. A sorption compressor with a single sorber bed for use with a Linde-Hampson cold stage. *Cryogenics*, 46:9–20, 2006.

[17] H. J. M. ter Brake. *Cryogenic systems for superconducting devices*, volume 365, pages 561–639. Kluwer Academic Publishers, Dordrecht, 2000. ISBN 0-7923-6113-X.

[18] G. Walker. *Cryocoolers, part 1: Fundamentals*. Plenum Press, New York, 1983.

[19] Micronit Microfluidics BV. Hengelosestraat 705, 7521 PA Enschede, The Netherlands, http://www.micronit.com/.

Chapter 7

Micro vacuum packaging

The micro cold stage needs a vacuum environment to minimize heat losses due to convection via the surrounding gas. All measurements described in the previous chapter were done using a conventional, relatively large vacuum chamber. If the micro cooler is to be turned into a 'stand-alone' commercial product, it would be convenient to integrate the cold stage with a micro vacuum package and the device to be cooled.

7.1 Micro vacuum package requirements

The requirements of such a package are as follows.

The vacuum package has to:

- create a vacuum surrounding for the designed micro cold stage and the device to be cooled
- realize a low enough chamber pressure thereby minimizing heat conduction through the surrounding gas
- maintain this vacuum during the life-time period of the cold stage
- be integrable with the cold stage production process
- include electrical feed-throughs to apply power and do measurements on the device to be cooled

7.2 Vacuum and gas sources

The word vacuum comes from the Latin word vacuus, meaning "empty". In practice, a chamber with perfect "emptiness" does not exist. Different gas sources result in a finite pressure inside the chamber. The pressure inside a (vacuum) chamber which is sealed from ambient pressure, may rise due to physical leaks in the chamber wall. Even if the chamber is hermetically sealed and no such leaks exist, the pressure may still rise over time. This is because of processes that let gases and vapors get into the chamber. These processes are subdivided into vaporization, desorption, diffusion and permeation [1], see figure 7.1.

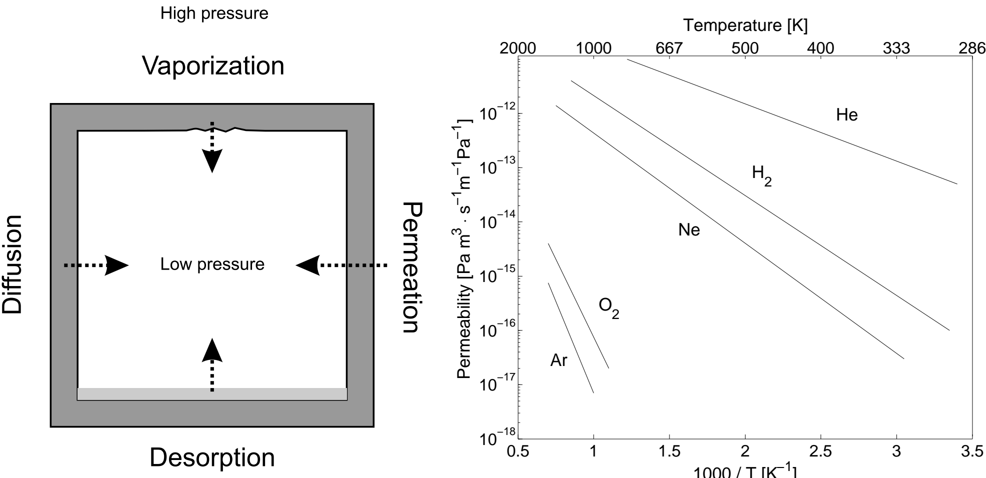

Figure 7.1: Left: potential sources of gases and vapors in a sealed vacuum system. Right: permeability of several gases through silicon oxide glasses vs. the reciprocal temperature. Data taken from ref. [2].

7.2.1 Vaporization

Vaporization is the gas flow caused by sublimation of the solid chamber wall. Sublimated molecules can return to the solid state when arriving at the surface. In equilibrium, the rate at which the wall vaporizes, is equal to the rate at which molecules return to the solid state at the surface. In this case, vaporization causes no more pressure increase in the chamber. In general, the vapor pressures of solids [3–5] at room temperature are many orders of magnitude smaller than the desired vacuum pressure (typically $p < 10^{-3}$ mbar). Therefore, vaporization plays no role in the design process and is thus neglected.

7.2.2 Desorption

Desorption is the release of adsorbed gases and vapors from the interior walls of the chamber. The adsorbed gases can have different origins. When the chamber wall has been exposed to a gaseous environment before closing, gases and water vapor are adsorbed on the wall. Desorption is also the final stage of the diffusion and permeation process, see paragraph 7.2.3 and 7.2.4. In UHV (ultra high vacuum) applications, a vacuum chamber is often heated during pumping, to increase the desorption rate and thus remove gases from the chamber walls.

7.2.3 Diffusion

Diffusion is an outgassing process caused by gases solved in the vacuum chamber wall. Gas molecules migrate through the solid wall due to a concentration gradient in the material. They are forced to travel from the bulk of the material to the surface where they desorb. Like desorption, the diffusion date increases with increasing temperature [6]. As will be explained in section 7.6, the vacuum package walls will be made of glass and silicon. Since the diffusion rate through semiconductors is in general a factor 10^3 smaller than through

Gas	Volume %	Partial pressure [mbar]
N_2	78.084	$0.78{\cdot}10^3$
O_2	20.946	$0.21{\cdot}10^3$
Ar	0.9340	$9.3{\cdot}10^0$
CO_2	0.0350	$0.35{\cdot}10^0$
Ne	0.001818	$18{\cdot}10^{-3}$
He	0.000524	$5.2{\cdot}10^{-3}$
CH_4	0.000170	$1.7{\cdot}10^{-3}$
Kr	0.000114	$1.1{\cdot}10^{-3}$
H_2	0.000055	$0.55{\cdot}10^{-3}$

Table 7.1: Composition of dry air. The amount of H_2O is highly variable, typically 1 %. Data taken from ref. [9].

glasses [7], the diffusion of gas through the silicon wafer is neglected during the package design.

7.2.4 Permeation

Permeation is a three-stage process, which consists of the adsorption of gases at the outer surface of the wall, the diffusion through the wall, and finally the desorption at the interior surface. The permeabilities of several gases through silicon oxide glasses like Pyrex 7740 have been plotted in the right graph of figure 7.1. Permeability increases with increasing temperature and with decreasing molecular diameter [1].

For glass, helium permeation will be the major source of gas permeation, considering the partial pressures of the gas components in air, shown in table 7.1 and the permeation rates shown in figure 7.1. No data is available on the permeability of N_2 through glass, but since its molecular diameter is slightly larger than the diameter of an oxygen molecule (0.31 nm vs. 0.29 nm), it is assumed that nitrogen permeation plays no role. The rate of helium permeating into the micro vacuum chamber (volume ≈ 0.1 cm^3) is estimated at about $4 \cdot 10^{-9}$ mbar·cm^3·s^{-1} (pressure partial difference is 0.52 Pa, chamber surface is about $5 \cdot 10^{-4}$ m^2 and the permeation distance is about $0.6 \cdot 10^{-3}$ m) which equals a permeation rate of about $1 \cdot 10^{-2}$ mbar / 26 days. Although it takes it relatively long time, the partial helium pressure inside the vacuum package will ultimately become equal to the partial helium pressure in the surrounding air which is about $5 \cdot 10^{-3}$ mbar.

To limit (helium) permeation a Ti coating can be deposited on the inner surface [8]. This has two functions, the Ti can serve as a diffusion barrier, thereby limiting the diffusion and permeation and Ti is capable of gettering other residual gases, in particular H_2O and O_2, see next section.

7.3 Required chamber pressure

The micro cold stage needs a vacuum environment to minimize heat losses due to convection via the surrounding gas. To make an estimate of the required pressure inside the chamber, equation 3.22 can be used:

$$P_{mol.cond} = \overline{\alpha}\lambda_m pA(T_h - T_c) \tag{7.1}$$

Figure 7.2 shows the calculated loss versus the chamber pressure using an estimation of $\overline{\alpha}$, λ_m and the calculated CFHX temperature profile and cooler's area A, see section 3.3.3. As can be seen, for chamber pressures above 10^{-2} mbar the loss is larger than the net cooling power of the cold tip which is about 10 mW. It can be concluded that the chamber pressure has to be below 10^{-3} mbar to reduce losses to an acceptable value.

7.4 Gettering

In order to reach low pressures and to maintain a long-life vacuum, getters can be used. A getter serves as a pump, adsorbing the residual gases in a system. Strong chemical bonds between the getter material and the adsorbed gas particles prevent desorption. Hence, for many gases, the process is irreversible, depending on the type of getter material used and the gases involved.

Getters need activation to initialize the sorbing process by heating up the getter material. The activation temperature differs per getter, but is usually a several hundred degree Celsius. During activation, the chemically bonded gas particles at the getter surface diffuse into the bulk. Reactivation after getter saturation is possible, though limited.

Previous work done on the fabrication of a micro vacuum package shows that if no getter material is used the final chamber pressure is in the order of several mbar [10] or

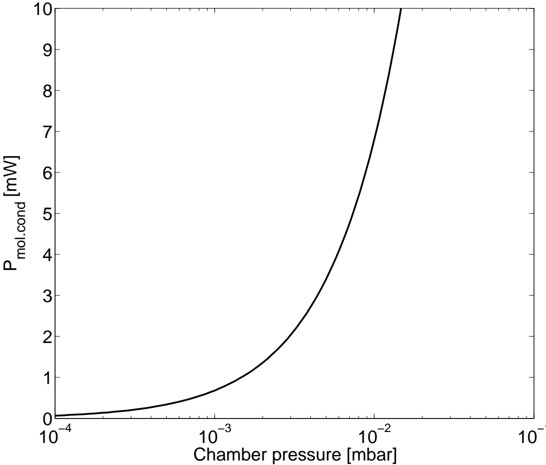

Figure 7.2: Estimated heat load versus vacuum chamber pressure.

higher [11]. This indicates that inclusion of a getter material is essential for attaining the low pressure needed. By using a getter material, pressures of $1 \cdot 10^{-2}$ mbar down to $1 \cdot 10^{-5}$ mbar have been reported [10–14].

The bonding process, as was described in section 2.2.5, can be used to fabricate a hermetically sealed vacuum package. During the bonding process, the system is heated to several hundred degrees Celsius, depending on the type of bonding used. Getter activation will occur at temperatures of $300-500$ ℃ which means that if the getter is included during bonding, activation occurs. Two options exist to prevent the activated getter getting in contact with atmospheric pressure.

The first possibility is to insert the getter after the bonding process through a vent. This has been done by Lee et al. [12]. After getter insertion, the vent is closed by anodically bonding a capping glass on top of the vent at a pressure of about $1 \cdot 10^{-6}$ mbar. The final attained pressure in the cavity was about $1 \cdot 10^{-4}$ mbar. A drawback of this method is the additional process steps involved for sealing the package.

A more elegant method is directly sealing the cavity during the bonding step. The incorporated getter is activated during the bonding process. The process takes place in a vacuum environment and the produced gases are gettered by the getter [10, 11, 13, 14]. Before sealing, the vacuum package should be heated in a vacuum environment, thereby desorbing the physically sorbed gases on both the wafer stack and the getter material. This is a crucial step, as Henmi et al. [11] have shown. If the package is not heated up before closing, a cavity pressure of 6.6 mbar was measured after bonding. Desorption of the getter and wafers prior to anodic bonding lead to pressures of $1.3 \cdot 10^{-5}$ mbar.

7.5 Pirani pressure sensor

Since the goal is to design a very small vacuum chamber, it is difficult to use commercial pressure sensors to measure the pressure inside the chamber. It is therefore obvious to also design and fabricate a pressure sensor which fits inside and can be integrated with the micro vacuum package.

In the molecular flow regime ($Kn \gg 1$, see section 3.2.2), the thermal conductivity of a gas is proportional to the pressure. The absolute pressure can therefore be determined indirectly by measuring the thermal conductivity of a gas. This is usually done by suspending a hot element, a so-called Pirani-sensor, in the vicinity of a heat sink. Two modes are commonly used to operate the Pirani pressure sensor. The first is the constant-power mode, in which the power dissipated in the sensor is at a constant level and the element's temperature is a measure for the pressure. The other method is the constant-temperature mode, where the element's temperature is kept constant and the power needed for this serves as a measure for the pressure.

Since the vacuum chamber is designed to insulate a micro cooler, it is desirable to make a pressure sensor with the same dimensions as a micro cooler. By doing so, the chamber's lay-out doesn't need a drastic redesign to suit the micro cooler. Also, in this way it will be easier to prove that the chamber will be at a sufficiently low pressure when integrated with an actual micro cooler, since the volume to surface ratio remains approximately the same.

The micro cooler consists of a stack of three glass wafers. Therefore, a sensor made in the plane of a glass wafer would meet the compatibility requirement, since the vacuum chamber can be built around the pressure sensor in the same way as that it could be built

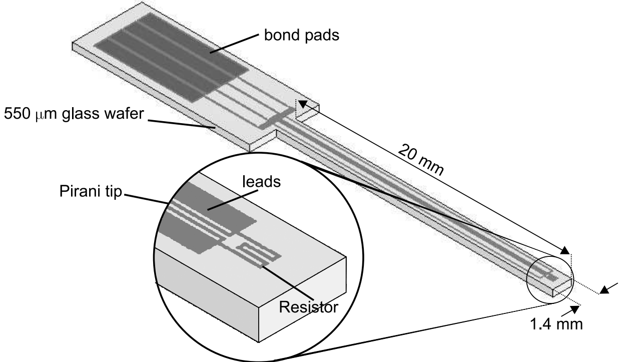

Figure 7.3: 3D schematic of the designed Pirani sensor.

around a micro cooler.

The general design of the developed pressure sensor is a glass cantilever on which a heating and sensing resistor is deposited, see figure 7.3. The cantilever is of about the same size as a micro cooler. Since the beam is relatively long, thin and narrow and because it is made out of glass, it serves as a thermal resistance between the tip and the chamber wall, from where it is suspended. Therefore, conduction losses are relatively small. The sensor itself is a resistor at the end of the cantilever, of which the resistance is determined by a four-point resistance measurement.

To predict whether the sensors operates in the correct pressure range and to determine design dimensions, a simulation [15] has been programmed in Matlab [16]. In the model, the temperature gradient between the hot tip and the supported side of the cantilever is assumed constant. Figure 7.4 shows the relative change of the sensor resistance at different chamber pressures at a constant input power of 5 mW and the sensor design

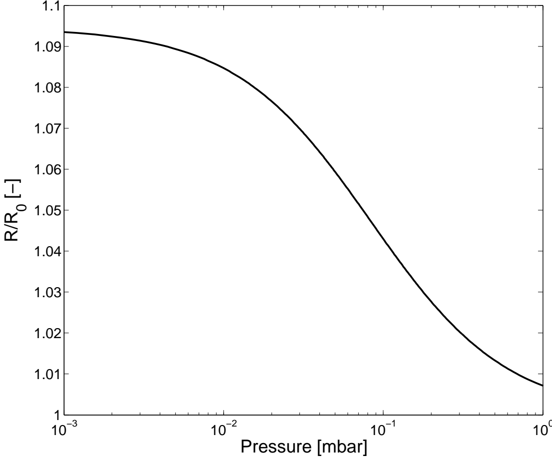

Figure 7.4: Simulated pressure sensor response at 5 mW heating power.

shown in figure 7.3.

As can be seen, according to the simulation, the pressure sensor is most sensitive between 10^{-1} and 10^{-2} mbar, but pressures down to 10^{-3} mbar should still be measurable.

7.5.1 Electrical feedthrough technology

Electrical feedthroughs are needed to apply power to the Pirani sensor and to read-out the four-point measurement. The feedthrough technology is also relevant if the micro cooler and the device to be cooled are to be integrated with the vacuum package. The device will also need power or measurement read-out lines.

Electrical feedthroughs can either be embedded in a wafer by placing them in an etched trench, or by depositing a lead of limited height on the bonding surface. The former method involves several problems regarding hermeticity. Not only lies the height of the metal fill within tight limits, due to mask underetching of Pyrex, long flat slopes along the metal strip are formed [17].

The second method involves less process steps. The metal lead is deposited on the glass wafer. The silicon wafer, with a thin SiO_2 insulation layer, is anodically bonded on top. At the bonding temperature, the metal lead expands while the glass, being the most ductile material used, deforms. Thereby the gap along the lead is filled. When cooling down, the metal contracts at a higher rate than the glass, but since the glass can withstand these loads, a hermetic seal is formed [18]. To guarantee hermeticity of the seal, this type of electrical feedthrough is limited by the step height of the conductor. According to Rogers et al. [19], the maximum height lies in the order of 60 nm. If too thick electrical leads are used, a phenomenon called 'tenting' occurs, see figure 7.5, where long voids are formed along the lead. The voids affect the hermeticity and cause considerable leakage. To minimize the risk on tenting, it is preferable to have sharp 'spikes' at several places along the lead, see picture (c) of figure 7.5. At the tips of these spikes, the change of forming a compression seal is larger and hermetic feedthroughs with a thickness up to 100 nm have been reported [17]. The electrical feedthroughs, fabricated for the micro vacuum packages, consist of a 38 nm Pt film with a 10 nm Ta adhesion layer.

To prevent an electrical short circuit, the silicon wafer needs to be covered with a thin oxide layer. For good bonds, the thickness of this layer should not exceed 460 nm [20]. Furthermore, SiO_2 has a breakdown voltage of $8 - 11$ MV·cm^{-1} [21], which should be taken into account when designing the electrical feedthroughs.

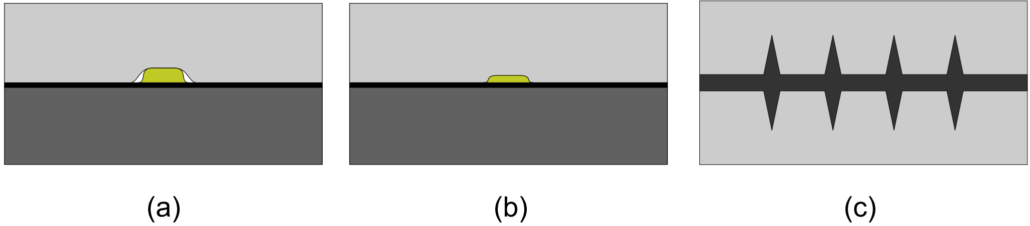

Figure 7.5: (a): Cross-sectional view of lateral electrical feedthrough. The bottom wafer is made of silicon, with a SiO_2-layer grown on top. The top wafer is glass. Tenting occurs along the metal feedthrough; (b): Same as (a) but now a hermetic seal is formed. (c): Top view of spikes along a lateral electrical feedthrough to prevent tenting.

7.6 Packaging design and fabrication

The vacuum chamber design is a stack of three wafers, of which the middle one is a 550 μm thick double side polished Corning Pyrex® 7740 [22] borosilicate glass wafer containing the pressure sensor, see figure 7.6. To prevent contact between the pressure sensor and the wall, the top and bottom wafer both hold a powder blasted cavity. The bottom wafer is a 1100 μm thick borofloat glass wafer from Louwers® [23]. A cavity with a depth of approximately 500 μm is powder blasted into the surface. The bottom wafer is fusion bonded to the middle wafer in a bonding press, which applies 11 metric tons. The result is shown in the top left picture of figure 7.7.

The top wafer is a 550 μm thick silicon wafer with an approximately 100 μm deep cavity. In this way, the Pirani pressure sensor is at a typical distance of $d = 100$ μm from the wall, hence $Kn \gg 1$ for pressures below $1 \cdot 10^{-1}$ mbar. Therefore the pressure sensor can operate in the molecular flow regime as long as the pressure is under about $1 \cdot 10^{-1}$ mbar.

The silicon wafer is covered with a 200 nm thick layer of SiO_2 in order to prevent an electrical short between the feedthroughs on the middle wafer, while keeping the possibility of good anodic bonds [20]. The top wafer also has a hole to make the bonding pads accessible from the outside.

After the two glass wafers are fusion bonded to each other, the silicon wafer and the stack of glass wafers are mounted in the anodic bonder and are separated from each other using spacers. In this way the vacuum cavities are still in contact with the surroundings and can therefore be pumped. The getter chambers are supplied with 125 μm thick ST122 getter strips from SAES® [24], see figure 7.6.

After mounting the wafers, the anodic bonder is closed and pumped down to $1 \cdot 10^{-4}$ mbar, also evacuating the vacuum cavities. Subsequently, the whole stack is heated to 200℃ for 90 minutes, to get rid of the physisorbed molecules on the getter and the adsorbed molecules on the cavity wall. This step is crucial for optimal getter activation, as Henmi et al. [11] have shown. The desorption of gases causes the pressure to rise, but after 90 minutes the pressure reaches $1 \cdot 10^{-4}$ mbar again.

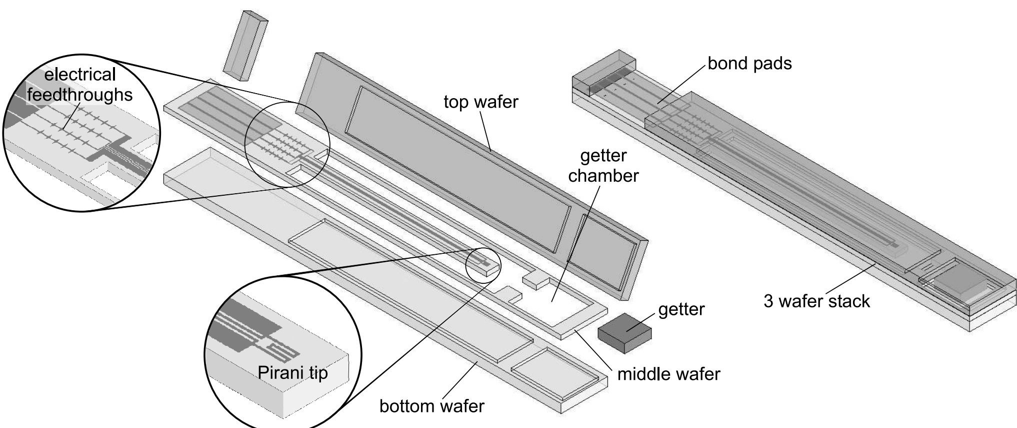

Figure 7.6: 3 dimensional schematic of of the micro vacuum chamber. Left: exploded view, right: assembly.

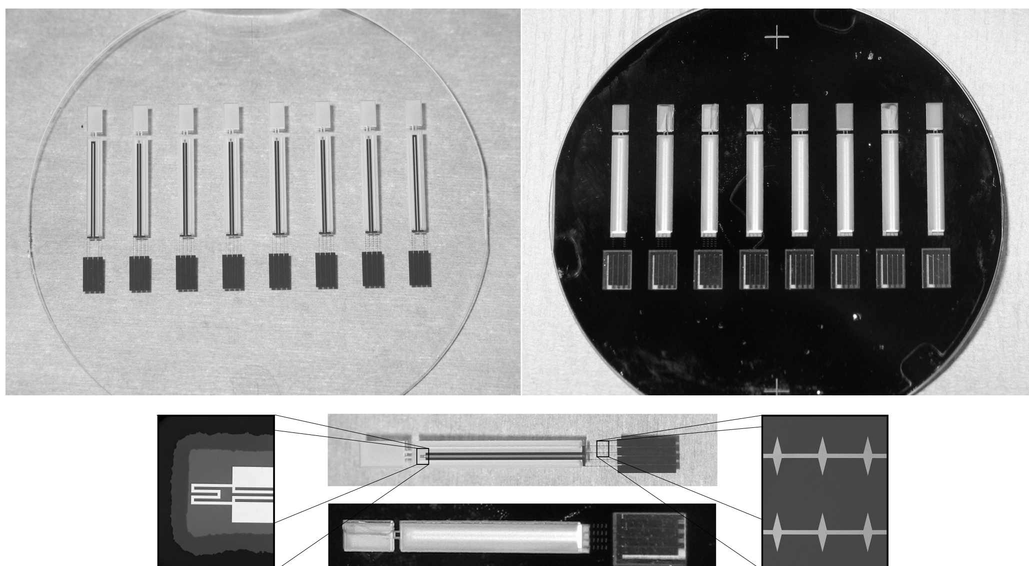

Figure 7.7: Top left: 2 glass wafer stack containing eight Pirani sensors. Top right: 3 wafer stack containing eight micro vacuum packages. Bottom: magnifications of a single vacuum package, the Pirani sensor tip (left) and the spikes on the electrical feedthroughs (right).

Subsequently, the spacers are removed and contact is made between the silicon wafer and the glass stack. Now the temperature is increased to 400℃ and anodic bonding is performed. After this, the temperature is raised to 500℃ to fully activate the getter. After 10 minutes the stack starts cooling down to room temperature and the vacuum package is ready, see right top picture of figure 7.7. For more details on the whole fabrication process, see [15].

The wafer stack contains three types of packages that differ in the electrical feedthrough design. There is one package without spikes on the leads, two with blunt spikes and one with sharp spikes, see figure 7.8. Of the latter two, each has five spikes on either side of an electrical lead. The other design parameters are equal for all cavities.

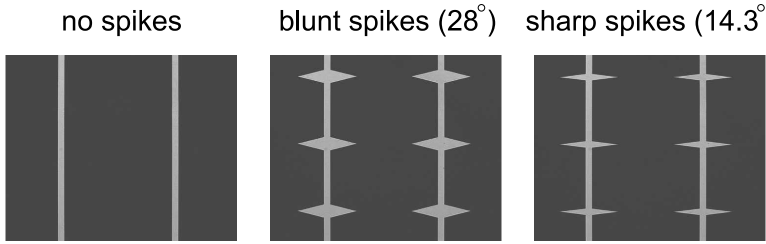

Figure 7.8: Photos of the electrical feedthroughs. In all cases the lead width is 50 μm.

7.7 Measurements

Measurements on the Pirani pressure sensor and the vacuum package are carried out with the setup shown in figure 7.9. The wafer stack is placed inside a large vacuum chamber of which the pressure can be regulated by means of a valve. In this way it is possible to calibrate the Pirani pressure sensors used to measure the pressure inside the packages, see section 7.7.1. The resistance of the Pirani pressure sensor is determined by a four-point measurement. The voltage across the hot element on the sensor's tip is directly measured, whereas the current is determined by measuring the voltage across a 100 Ω precision resistor. Data is processed using a PC equipped with a National Instruments Data Acquisition card and Labview [25].

7.7.1 Sensor calibration

Pirani sensors calibration is done with a sensor on the wafer whose cavity is in direct contact with the surrounding vacuum chamber. A hole is powder blasted in the getter space so the silicon and glass walls around the Pirani sensor are not affected. This is done to have identical geometry around each pressure sensor and thereby, at equal pressure, the same value of Kn for each package within the wafer stack. The cavity pressure of the calibration sensor can be adjusted by adjusting the pressure in the large chamber.

The relative change in sensor resistance will be used as a measure for the chamber pressure. Since $\frac{R}{R_0}(T)$ is the same for all Pirani sensors, a calibration of the sensor which is in direct contact with the environment, is used to make an estimate of the pressure inside the other packages.

The Pirani sensors are operated in constant-power mode. The dissipated power is calculated by measuring the current I_p through and voltage V_p across the sensor. The input power is kept constant for changing sensor temperatures. The response of the Pirani sensor in the "open" device using 5 mW input power, is plotted in figure 7.10. The figure shown is in very good agreement with the simulated graph shown in figure 7.4.

In order to determine the repeatability and the difference between sensors from the same batch, multiple measurements have been carried out with several sensors. The error margins resulting from these measurements are also depicted in figure 7.10.

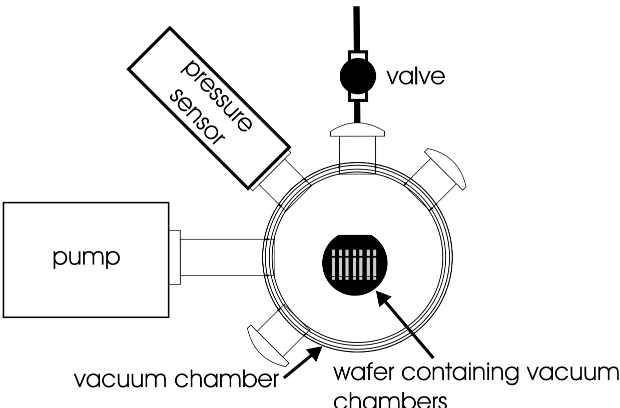

Figure 7.9: Setup used for sensor calibration and cavity pressure measurement.

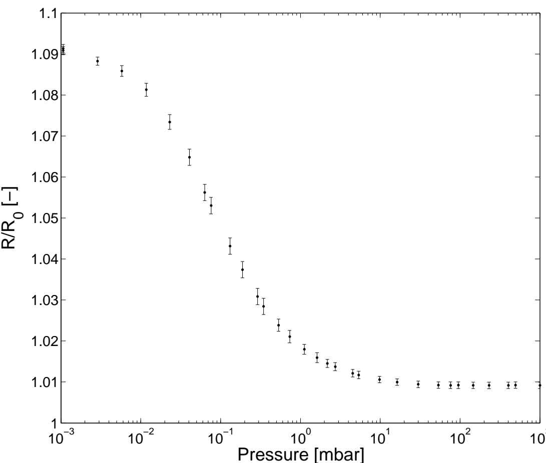

Figure 7.10: Pirani sensor response at 5 mW input power.

7.7.2 Package pressures

Cavity pressures of several packages have been determined by measuring $\frac{R}{R_0}$. The results are shown in figure 7.11. As can be seen, none of the packages is hermetic. After a certain period of time, which varies from package to package, the pressure starts to rise. After package closure, the pressure remains constant for some time, or is at least below the lower limit of the sensor's range. The constant low pressure can be attributed to the active getter, which sorbs the incoming gases. After a while, sorbing slows down and eventually getter saturation occurs, allowing the pressure to rise.

Once the pressure starts rising, the increase is linear, as can be seen in the right graph of figure 7.11. This is as expected, since the pressure difference between cavity and atmosphere is roughly constant. All cavity volumes are approximately 0.1 cm^3, therefore, the absolute leak rate of all four packages can be determined, using the slopes of the linear fits:

Measurement	a	b	c	d
Leak rate	$5.8 \cdot 10^{-7}$	$1.4 \cdot 10^{-7}$	$1.1 \cdot 10^{-7}$	$3.0 \cdot 10^{-8}$

with the leak rate in [mbar·cm^3·s^{-1}]. In order to get some feeling for these numbers, we can extrapolate the pressure increase in the cavities. If linear increase is assumed, chamber d) reaches atmospheric pressure in approximately 100 years. In reality, leak rates will decrease in time due to decreasing pressure difference between cavity and surroundings, even prolonging this period. However, only about 10 hours are needed to increase the pressure to about $1 \cdot 10^{-2}$ mbar.

All cavities are equipped with a getter of which the area is approximately $2.1 \cdot 10^{-1}$ cm^2. Combining this with the different times the pressures start increasing, the sorbed quantities before getter saturation vary from $5.2 \cdot 10^{-2}$ to $1.9 \cdot 10^{-1}$ mbar·cm^3·cm^{-2}. This approximately coincides with the maximum sorbed quantity CO according to the getter data sheet, see appendix D.1. The figure shown in appendix D.1 is the only sorbing data

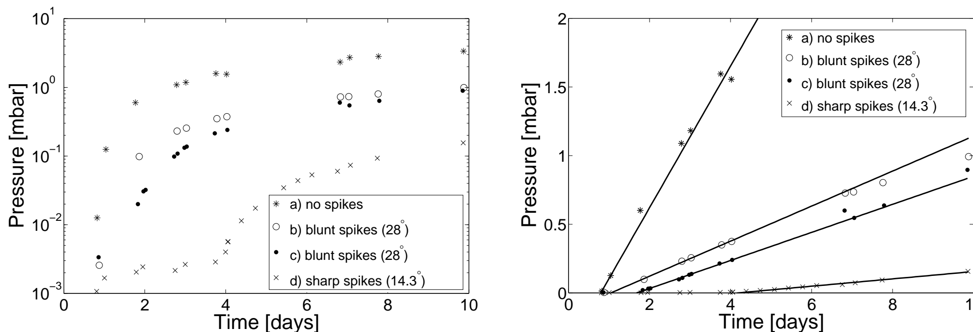

Figure 7.11: Left: Pressure development in time for the different vacuum packages plotted logarithmically. Right: Pressure development in time of plotted linearly.

available on the ST122 getter, but it is likely that the sorption curves of the diatomic gases N_2 and O_2 resemble the CO sorption curve.

Apart from these four packages, micro vacuum chambers have been fabricated without the addition of a getter. Directly after closure, all these cavities had pressures above 10 mbar, the upper limit of the Pirani pressure sensor. Therefore, it is shown that a getter is required in this fabrication process, to reach the low pressures needed. This was as expected, since Henmi et al. [11] reached a cavity pressure of $1.3 \cdot 10^2$ mbar using anodic bonding without including a getter.

The measured leak rates are several orders of magnitude higher than the helium permeation rate calculated in section 7.2.4. Helium permeation through a 600 μm thick Pyrex 7740 glass wafer at room temperature, was determined to be $4 \cdot 10^{-9}$ mbar·cm^3·s^{-1}. Also, after several days, the cavity pressures are above the partial pressure of helium in air, see table 7.1. Hence, helium permeation is not the dominant cause of the pressure increase.

It is plausible that the pressure increase is caused by tenting, which has been discussed in section 7.5.1. As shown in figure 7.11, the package without spikes, leaks the most. Also, it appears that the sharper the spikes, the smaller the leak. The latter could be due to easier formed compression bonds at sharper corners, as less material needs deformation. Since all design parameters, except for the electrical feedthroughs, are identical for each package, it is assumed that leakage is primarily caused by tenting.

7.8 Conclusions

A micro vacuum package, designed to create a vacuum environment for a micro cooler, is designed and fabricated. The chamber volume is about $\approx$ 0.1 cm^3. Calculations show that in order to provide sufficient vacuum insulation, the pressure inside the chamber should stay below about 10^{-3} mbar. Chamber pressures in the order of 10^{-3} mbar or below have been reached. However, due to physical leaks no long-life vacuum has been established. The package with the smallest leak had a leak rate of about $3 \cdot 10^{-8}$ mbar·cm^{3}s^{-1} and showed getter saturation after approximately 4 days. It is expected that tenting along the electrical feedthroughs is causing the leaks.

References

[1] J.F. O'Hanlon. *A user's guide to vacuum technology.* New York; Chichester: Wiley, 1980. ISBN 0-471-01624-1.

[2] W.A. Rogers, R.S. Buritz, and D. Alpert. Diffusion coefficient, solubility, and permeability for helium in glass. *Journal of applied physics*, 25:868–875, 1953.

[3] E. Suurmeijer and T. Mulder and J. Verhoeven. *Basisboek vacuümtechniek.* Krips, Meppel, 2nd edition, 2000. ISBN 90-9013776-9.

[4] A. Roth. *Vacuum technology.* Elsevier Amsterdam, 3nd edition, 1990. ISBN 0-444-86027-4.

[5] S.G. Davis, D.F. Anthrop, and A.W. Searcy. Vapor pressure of silicon and the dissociation pressure of silicon carbide. *Journal of chemical physics*, 34:659–664, 1961.

[6] W.G. Perkins. Permeation and outgassing of vacuum materials. *Journal of Vacuum Science and Technology*, 10:543–556, 1973.

[7] A. Gerlach, W. Keller, J. Schultz, and K. Schumacher. Gas permeability of adhesives and their application for hermetic packaging of microcomponents. *Microsystem Technologies*, 7:17–22, 2001.

[8] S.H. Choa. Reliability of MEMS packaging: vacuum maintenance and packaging induced stress. *Microsystem Technologies*, 11:1187–1196, 2005.

[9] NASA, Earth fact sheet. http://nssdc.gsfc.nasa.gov/planetary/factsheet/earthfact.html.

[10] D. Sparks, S. Massoud-Ansari, and N. Najafi. Reliable vacuum packaging using nanogetters^{TM} and glass frit bonding. In *Proceedings SPIE*, volume 5354, pages 70–78, Jan. 2004.

[11] H. Henmi, S. Shoji, Y. Shoji, K. Yoshimi, and M. Esashi. Vacuum packaging for microsensors by glass-silicon anodic bonding. *Sensors and Actuators A*, 43:243–248, 1994.

[12] D.J. Lee, Y.H. Lee, J. Jang, and B.K. Ju. Glass-to-glass electrostatic bonding with intermediate amorphous silicon film for vacuum packaging of microelectronics and its application. *Sensors and Actuators A*, 89:43–48, 2001.

[13] Y.T. Cheng, W.T. Hsu, K. Najafi, C.T.C. Nguyen, and L. Lin. Vacuum packaging technology using localized aluminum-silicon-to-glass bonding. *Journal of microelectromechanical systems*, 11:556–565, 2002.

[14] B. Lee, S. Seok, and K. Chun. A study on wafer level vacuum packaging for MEMS devices. *Journal of micromechanics and microengineering*, 13:663–669, 2003.

[15] J. Koning. *Cryogenic micro cooling, a study into dynamic modeling & wafer level vacuum packaging.* University of Twente, 2006. M.Sc. thesis.

[16] The MathWorks, Inc. 3 Apple Hill Drive, Natick, MA 01760-2098, USA, http://www.mathworks.com.

[17] K.M. Hiltmann, B. Schmidt, H. Sandmaier, and W. Lang. Development of micromachined switches with increased reliability. In *Transducers '97*, pages 1157–1160, Chicago, June 1997.

[18] T. Corman. *Vacuum-sealed and gas-filled micromachined devices.* PhD thesis, School of Electrical Engineering & Royal Institute of Technology, Stockholm, 1999. ISBN 91-7170-482-5.

[19] T. Rogers and J. Kowal. Selection of glass, anodic bonding conditions and material compatibility for silicon-glass capacitive sensors. *Sensors and Actuators A*, 46–47:113–120, 1995.

[20] T. Corman, P. Enoksson, and G. Stemme. Low-pressure-encapsulated resonant structures with integrated electrodes for electrostatic excitation and capacitive detection. *Sensors and Actuators A*, 66:160–166, 1998.

[21] www.SemiconFarEast.com. http://www.semiconfareast.com/oxidebreakdown.htm.

[22] Corning. Koolhovenlaan 12, NL-1119 NE Schiphol-Rijk, The Netherlands, http://www.corning.com.

[23] Louwers glass and ceramic technologies. Energieweg 3A, 5527 AH Hapert, The Netherlands, http://www.louwers.nl.

[24] Saes Getters. Viale Italia 77, 20020 Lainate (Milan), Italy, http://www.saesgetters.com/.

[25] National Instruments Corporation, 11500 N MoPac Expwy, Austin, TX 78759-3504, USA, http://www.ni.com.

Chapter 8

Conclusions and recommendations

8.1 Micro cold stage

8.1.1 Conclusions

The objective to fabricate a cryogenic recuperative micro cooler by means of MEMS technology only is accomplished. MEMS fabrication techniques are highly suitable for the construction of JT cooler parts in micro dimensions. The high fabrication accuracy and possibility of batch processing open the opportunity to mass produce micro cold stages with a constant quality and predictable specifications at relatively low cost.

The geometric design of the micro cold stage is optimized for both maximum COP and minimum size with constant net cooling power. This is done by treating all losses in the cold stage (i.e. thermal losses and pressure drop losses) as a production of entropy. The theoretical optimal geometry is found by minimizing the total produced entropy of the cold stage. It was found that variations in the geometric design parameters of this optimal design, mainly have an influence on the calculated pressure drop. The theoretical optimal design is adjusted to compensate for the increased pressure drop in the channels as a result of the use of micro pillars inside inside the channels. These pillars highly reduce the change of mechanical failure of the cold stage. The dimensions of the final "optimal" design are: 28 mm x 2.2 mm x 0.8 mm.

Besides the optimal design of a micro cold stage with a net cooling power of 10 mW, also the optimal design for relatively larger cooling powers was investigated. It is found that for a net cooling power above approximately 40 mW the optimum height of the channel becomes constant (about 37 μm). Also the length reduces to a constant value at larger values of the cooling power (about 31 mm). The width of the channel however, increases linearly over the whole domain. Hence, for higher cooling powers it is sufficient to "use a number of identical coolers in a parallel way" to increase the net cooling power.

Five different designs of single stage micro coolers, see table 8.1, were tested. All of the tested designs cooled down to liquid nitrogen temperature. Cooling power measurements indicated that the micro cold stages suffer from parasitic heat loads induced by the measurement setup. This heat load is calculated and strongly depends on the chosen

surface emissivities of the used thermocouple, wiring and the heater. Both a minimum and maximum value is estimated and found to be respectively 6 mW and 10 mW. The measured net cooling powers of the different cold stages are compensated for this heat load, see table 8.1.

Table 8.1: Cold stage prototype, measurement results.

Prototype number	**1**	**2**	**4**	**5**	**6**
CFHX channel width [mm]	2.0	2.0	2.0	2.0	4.0
CFHX channel length [mm]	25	15	25	35	25
Mass flow [mg·s^{-1}]	1.0	1.0	2.0	2.0	2.0
P_{net} calculated [mW]	12.6	7.8	20.0	24.1	25.5
P_{net} compensated [mW]	11 ± 2	9 ± 2	15.5 ± 2	24 ± 2	21 ± 2

Results show that most of the expected cooling powers are located within the measured net cooling power domain. For two cold stages, numbers 4 and 6, the measured power is less than the expected value. This is due to unintentional variations in the measurement setup, for example grease stains on the reflective shield or a larger resistor surface. It is clear that the measurement setup has a large influence on the determination of the net cooling power which results in a large uncertainty. Some recommendations are made on this issue in the next section. Nevertheless, the results are certainly satisfying and it can be concluded that the static BH-model, that was used, gives a reliable prediction of the net cooling power of a micro cold stage.

A dynamic model was presented that gave a good estimate of the cool-down time of a micro cold stage. The measurements are in agreement with the cool-down curve calculated with the model. However, again the influence of parasitic heat loss due to the measurement setup is considerable. Relatively small changes in these parameters can have a large influence on the calculated results.

8.1.2 Recommendations

Clogging

A critical issue in the operation of the micro cooler is clogging caused by the deposition of water molecules. The clogging problem can be subdivided into two separate issues.

In the first place clogging of the cold stage during initialization (cool down) due to relatively high partial water pressure contamination. Even though a gas filter is installed in the setup which reduces the contamination level below 1 ppb, the cold tip can still clog during initialization. This is because of a higher local initial partial water pressure inside the system located after the filter. This partial water pressure is about 5 Pa corresponding to about 0.5 ppm. Before initialization the system has to be heated, pumped and flushed to reduce contamination as much as possible. Additionally, the dead volume between filter and cold stage should be as small as possible. This way the absolute amount of contamination is highly reduced. In this case a cold stage with integrated getter filter would be ideal. If the cold tip gets clogged during cool down, the restriction temperature has to be increased above the sublimation temperature so the contaminants leave the system. This procedure can be and was automated in the measurement setup and should be repeated until the cold tip cools down to liquid nitrogen temperature.

The second clogging issue is clogging of the cold stage after a 'long' period of time at relatively low partial water pressure contamination. The partial water pressure at the location of the restriction during operation is calculated at about 10^{-10} Pa corresponding to about 10^{-11} ppm. However, during measurements it is seen that the cold stage still clogs after a few hours because of ice crystals which migrate from the CFHX to the flow restriction, thus blocking the flow and reducing the cooling power. This is an intrinsic problem with an open-loop cycle. The system is continuously supplied with new nitrogen gas from a gas bottle. Because of this, the system is also fed with a constant level of contaminant gas. If the gas cycle is turned into a closed cycle, e.g. using a sorption compressor [1–3], the gas can be re-used and filtered every cycle. This way the contamination level drops continuously enabling the micro cooler to operate for long periods of time.

Measurement setup

As is mentioned before, the thermocouple, the wiring and the heater cause a large heat load on the cold tip which can go up to 90% of the net cooling power. Several possibilities on alternative temperature measurements, not described in this thesis were investigated [4].

One of the most promising possibility found, is a wireless temperature measurement through phosphorescence [5–8]. In summary: a thin layer of phosphor mixed with a binder is deposited on the cold stage. This phosphor consists of a ceramic doped with rare-earth ions like Eu^{+3}, Nd^{+3} or Dy^{+3}. The dopant ions emit strong phosphorescence when exited by UV radiation using e.g. a laser pulse. After activation, de-excitation by a photon emission in the phosphor occurs. The lifetime and intensity of the photons is temperature dependent. The temperature of the substrate surface is thus measured by either measuring the decay time of a selected emission line or measuring of the intensities of one or two emission lines [9]. Unfortunately, due to difficulties with the availability of the measurement equipment [10], this method could not be used in practice during this project.

Another solution to reduce the influence of the measurement setup is to integrate a temperature sensor and a heater in the cold stage production process. A widely used temperature sensor at cryogenics temperatures is the platinum resistance [11, 12]. The gold reflective shield of the cold stage can be replaced by a reflective shield of platinum. A platinum resistance can than be etched inside the thin layer and function as a temperature sensor as well as a heater.

Even smaller?

The smallest cooler fabricated during this project has the dimensions: 18 mm x 2.2 mm x 0.8 mm and a net cooling power of about 8 mW. In the optimization study, it is shown that for the same design parameters (i.e. $\dot{m} = 1$ mg·s^{-1}, wall thickness = 100 μm, etc), the length of the CHFX can be reduced to about 10 mm, giving a total cold-stage length of about 13 mm. The calculated net cooling power is then about 0.5 mW (COP is about 0.002). The main loss at these small lengths is heat conduction. At constant length and constant temperature difference, this loss can only be reduced by either reducing the cross-sectional area of the cooler or changing the fabrication material. The cross-sectional area can be reduced by using thinner wafers and/or reducing the wafer thickness by means of

powder blasting as was done in the presented production process. This will of course have an influence on the mechanical strength of the device and on the yield of the production process. Another option is to use another material with a lower heat conduction coefficient to fabricate the cold stage. However, there is no obvious choice what this material should be.

Multistage micro cooler

The design of the presented multi-stage cooler was not optimized. An optimization study, similar to the one presented in section 3.5, should be done to reach maximum COP in combination with minimum cold-stage dimensions.

The CFHX of the 1st stage must be separated from CFHX I of the 2nd stage by adjusting the mask design and/or the powder blasting process for this specific step.

The multi-stage cooler has to be provided with a good thermal link from 1st stage cold tip to the 2nd stage pre-cooling point so that the neon is pre-cooled to about 100 K. This can, for example, be done by depositing a "thick" layer of metal (e.g. copper) from cold tip to pre-cooler or bonding a piece of silicon at this spot.

The influence of the measurement setup on the operation of the cold stages should be minimized. This can for example be done by integrating the fabrication of temperature sensors in the cold-stage construction process. Instead of using gold as a reflective shield, platinum could be used. Inside the thin platinum layer, tiny resistors can be etched and used as temperature sensors.

8.2 Micro vacuum package

8.2.1 Conclusions

A micro vacuum package, designed to create a vacuum environment for a micro cooler, is designed and fabricated. The chamber volume ($\approx$ 0.1 cm^3) is encapsulated in a stack of three wafers. The bottom and middle wafer are made of glass and the top wafer of silicon. The pressure inside the chamber is measured via a specially designed thin film Pirani sensor which is deposited on a small cantilever powder blasted in the middle wafer. The dimensions of this cantilever approximate the dimensions of a typical micro cooler. Calculations show that in order to provide sufficient vacuum insulation, the pressure inside the chamber should stay below about 10^{-3} mbar. Chamber pressures in the order of 10^{-3} mbar or below have been reached. However, due to physical leaks no long-life vacuum has been established. The package with the smallest leak had a leak rate of about $3 \cdot 10^{-8}$ mbar·cm^{3}s^{-1} and showed getter saturation after approximately 4 days. It is expected that tenting along the electrical feedthroughs is causing the leaks.

8.2.2 Recommendations

To prevent leaks due tenting, the height of the electrical feedthroughs should be reduced. The fabricated electrical feedthroughs consist of a 38 nm Pt film with a 10 nm Ta adhesion layer. Although this is well below the 60 nm maximum height determined by Rogers et al. [13], decreasing the thickness of the film results in a higher chance of a hermetic seal. Also decreasing the leads width can be considered.

Providing the electrical feedthroughs with spikes is highly recommended. Leaks seem to reduce if sharper spikes are used. It should also be investigated if the number of spikes used has an influence on the chamber pressure.

Although during the presented measurements permeation was not an issue, for long-life vacuum it can be limited by depositing a thin Ti coating on the inner surface of the vacuum enclosure.

References

[1] G. Wiegerinck. *Improving sorption compressors for cryogenic cooling.* PhD thesis, University of Twente, 2005.

[2] J. F. Burger, H. J. M. ter Brake, H. Rogalla, and M. Linder. Vibration-free 5 K sorption cooler for ESA's Darwin mission. *Cryogenics*, 42:97–108, February 2002.

[3] G.F.M. Wiegerinck, J.F. Burger, H.J. Holland, E. Hondebrink, H.J.M. ter Brake, and H. Rogalla. A sorption compressor with a single sorber bed for use with a Linde-Hampson cold stage. *Cryogenics*, 46:9–20, 2006.

[4] L. G. Rubin. Cryogenic thermometry: a review of progress since 1982. *Cryogenics*, 37:341–356, July 1997.

[5] Andrew M. Leach, Radislav A. Potyrailo, and Gary M. Hieftje. Design and characterization of a radioluminescent temperature sensor. *Analytica Chimica Acta*, 412:47–53, May 2000.

[6] F. Anghel, C. lliescu, K.T.V. Grattan, A.W. Palmer, and Z. Y. Zhang. Fluorescent-based lifetime measurement thermometer for use at subroom temperatures (200-300 K). *Rev. Sci. Instrum.*, 66:2611–2614, 1995.

[7] Yong Wook Lee and Byoungho Lee. High resolution cryogenic optical fiber sensor system using erbium-doped fiber. *Sensors and Actuators A: Physical*, 96:25–27, January 2002.

[8] S. W. Allison and G. T. Gillies. Remote thermometry with thermographic phosphors: Instrumentation and applications. *Rev. Sci. Instrum.*, 68:2615–2650, 1997.

[9] A. C. Edge, G. Laufer, and R.H. Krauss. Surface temperature-field imaging with laser-induced thermographic phosphorescence. *Applied Optics*, 39:546–553, February 2000.

[10] Luxtron Corporation, Vinkeveen, The Netherlands, http://www.luxtron.com.

[11] A. L. Zahariev, D. A. Dimitrov, and J. K. Georgiev. Characteristic stabilization of thin film platinum thermometers during thermal cycling between 5 K and 300 K. *Cryogenics*, 36:631–634, August 1996.

[12] D. A. Dimitrov, J. K. Georgiev, A. L. Zahariev, and I. Bivas. Estimation of thin-film platinum thermometer precision in the range 13.8-273.16 K and common mathematical description above 70 K. *Cryogenics*, 36:599–603, August 1996.

[13] T. Rogers and J. Kowal. Selection of glass, anodic bonding conditions and material compatibility for silicon-glass capacitive sensors. *Sensors and Actuators A*, 46–47:113–120, 1995.

Chapter 9

Outlook

9.1 Integration

One of the future goals is to integrate the micro cold stage with the device to be cooled and a micro vacuum chamber, see figure 9.1. This way a "stand alone" device is created which has to be connected to a compressor, see next section. The device consists of a stack of five bonded wafer, three for the cooler and two to create a vacuum chamber. The device which has to be cooled is connected to the cold tip and thin film electronic leads are deposited on top of the micro cooler to provide electronic connections. The electronic feedthroughs include a high density of sharp spikes to ensure a hermetic seal. The vacuum chamber is provided with a getter material to establish a pressure below 10^{-3} mbar which is maintained during the micro cooler's life-time. A thin Ti coating is deposited on the inner surface of the vacuum enclosure to limit (He) permeation.

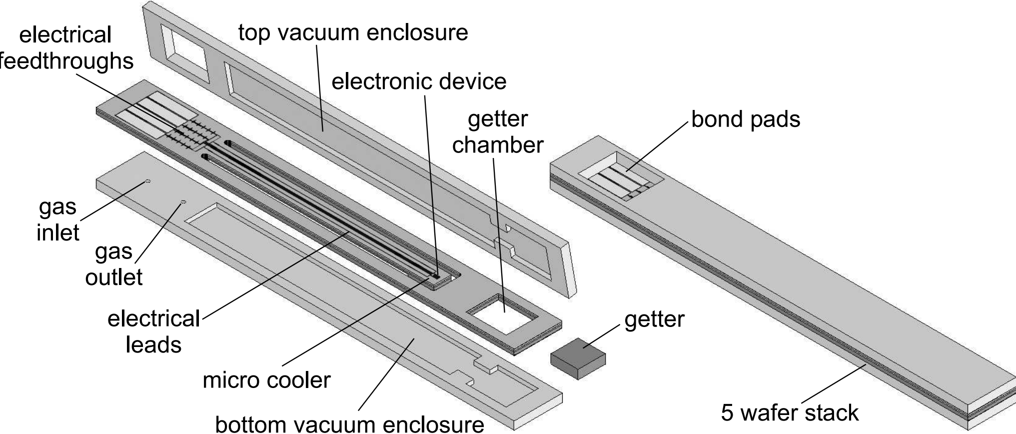

Figure 9.1: 3 dimensional schematic of the integrated device. Left: exploded view, right: assembly

9.2 Compressor

The cold stage is designed in such a way that it can be combined with a sorption compressor [1–3]. Doing so, a system is realized which has no mechanically moving parts and is potentially vibration free. The cooling device can be integrated with a micro sorption compressor to realize a total micro system. Ideally, this system only needs an electronic power supply to operate, see left picture of figure 9.2. However, such a micro sorption compressor does not (yet) exist.

Another solution for the compressor is to connect a series of micro cold stages to one relatively big (sorption) compressor, see right picture of figure 9.2. The micro coolers are distributed over a large area and cool the electronic devices on the spot. They are connected to a grid of low- and high-pressure tubing which is provided with gas by the compressor.

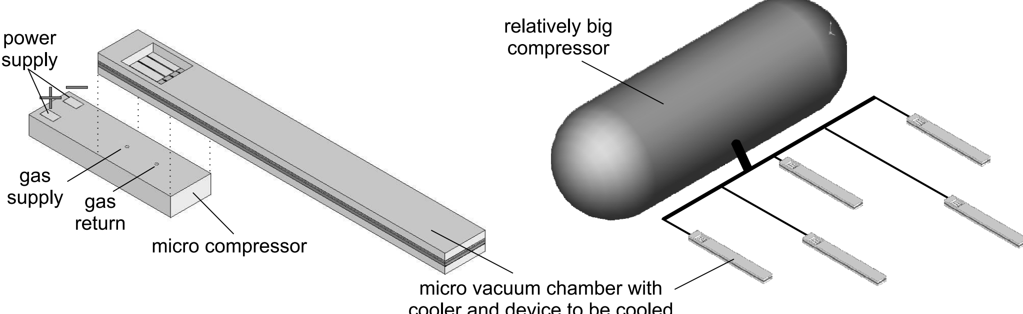

Figure 9.2: Left: integrated micro cold stage combined with micro compressor. Right: multiple micro cold stages combined with one relatively large compressor.

References

[1] G. Wiegerinck. *Improving sorption compressors for cryogenic cooling.* PhD thesis, University of Twente, 2005.

[2] J. F. Burger, H. J. M. ter Brake, H. Rogalla, and M. Linder. Vibration-free 5 K sorption cooler for ESA's Darwin mission. *Cryogenics*, 42:97–108, February 2002.

[3] G.F.M. Wiegerinck, J.F. Burger, H.J. Holland, E. Hondebrink, H.J.M. ter Brake, and H. Rogalla. A sorption compressor with a single sorber bed for use with a Linde-Hampson cold stage. *Cryogenics*, 46:9–20, 2006.

Appendix A

Gas and cycle properties

References

[1] Cryodata Inc. http://www.cryodata.com.

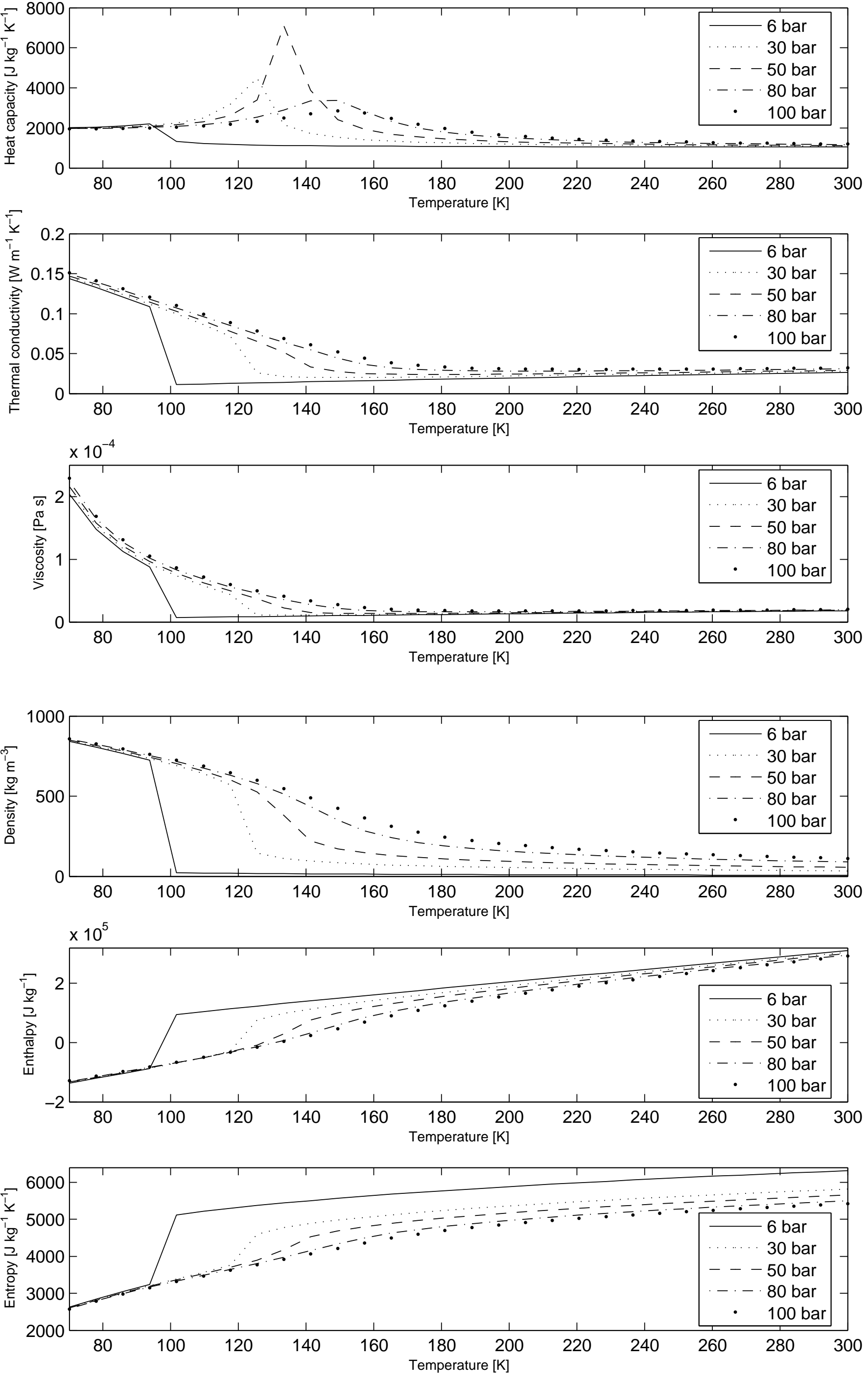

Figure A.1: Gas properties of nitrogen gas. Data taken from [1]

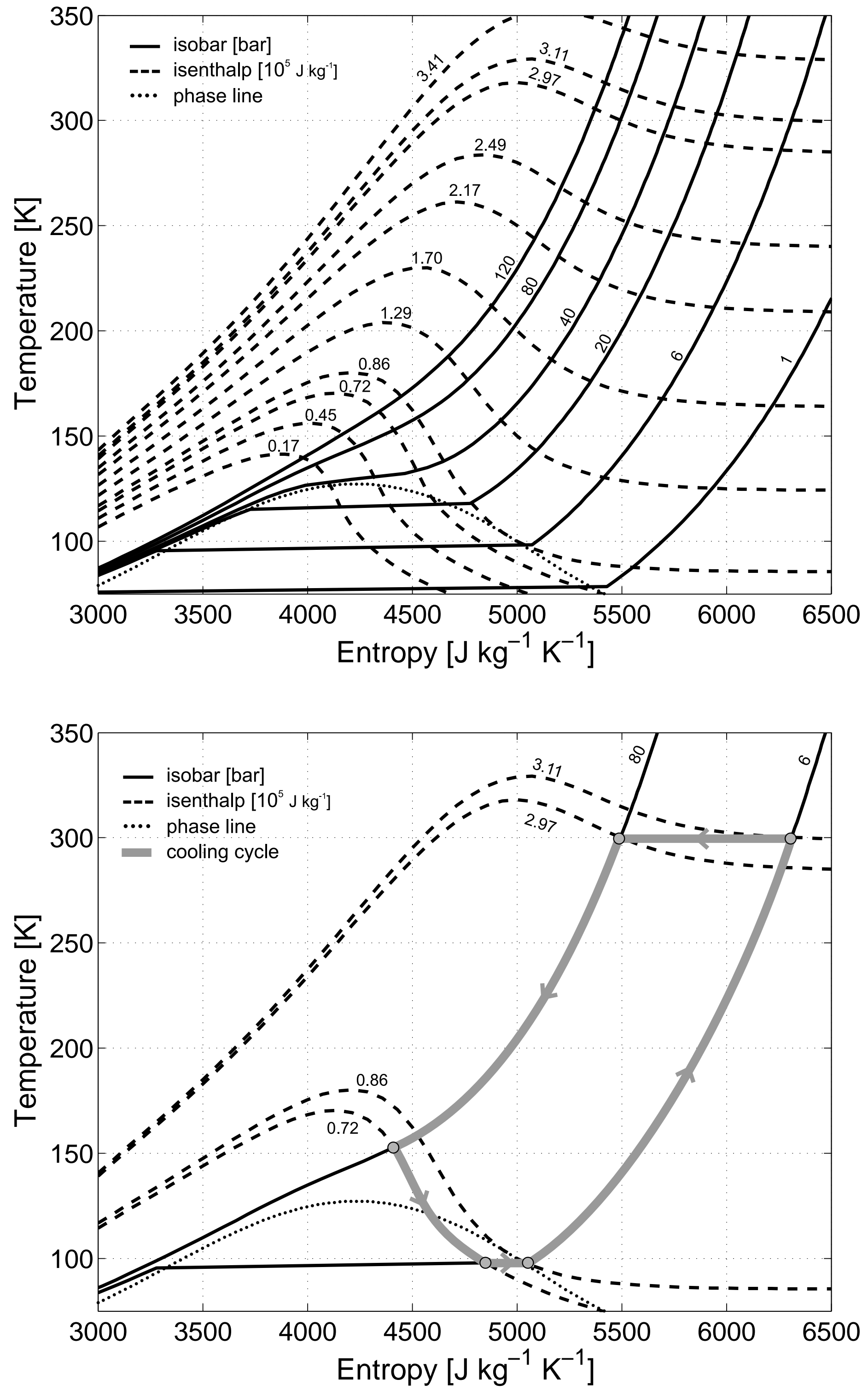

Figure A.2: Top plot: T-s diagram for nitrogen. Bottom plot: T-s diagram for nitrogen with the micro cold stage cycle high-lighted. Data taken from [1]

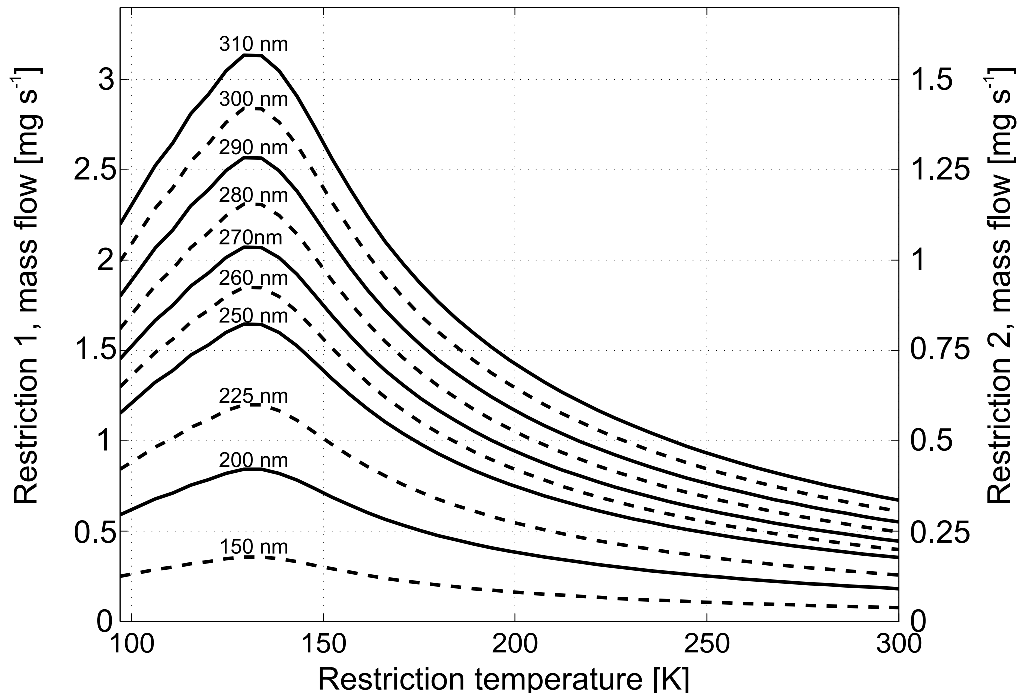

Figure A.3: Mass flow versus restriction temperature for different restriction heights. Restriction 1: width is 1 mm and the length is 0.07 mm. Restriction 2: width is 1 mm and the length is 0.14 mm.

Appendix B

Optimization graphs

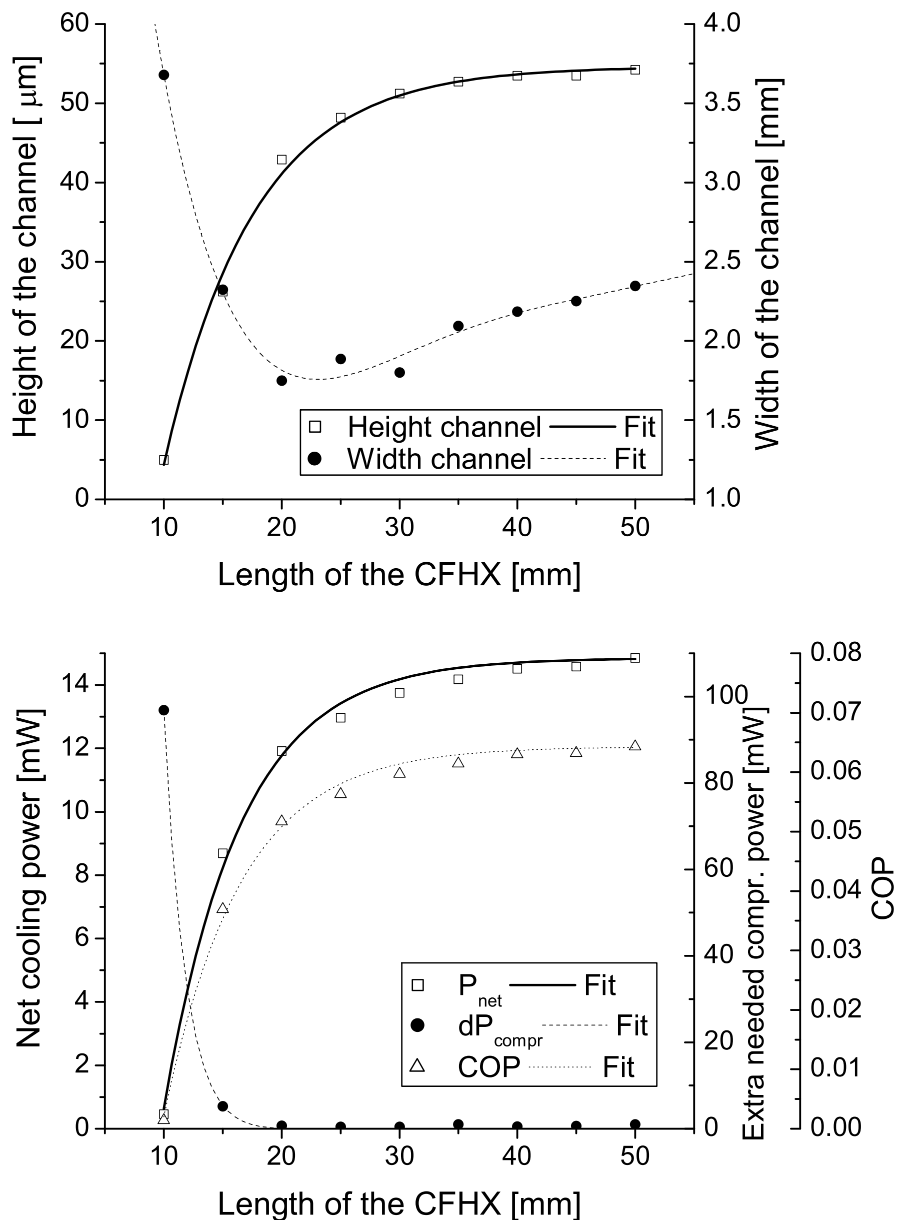

Figure B.1: Magnification of optimization results of section 3.5.2.

Appendix C

Fabrication details

10 x 10 cm wafer mask layout

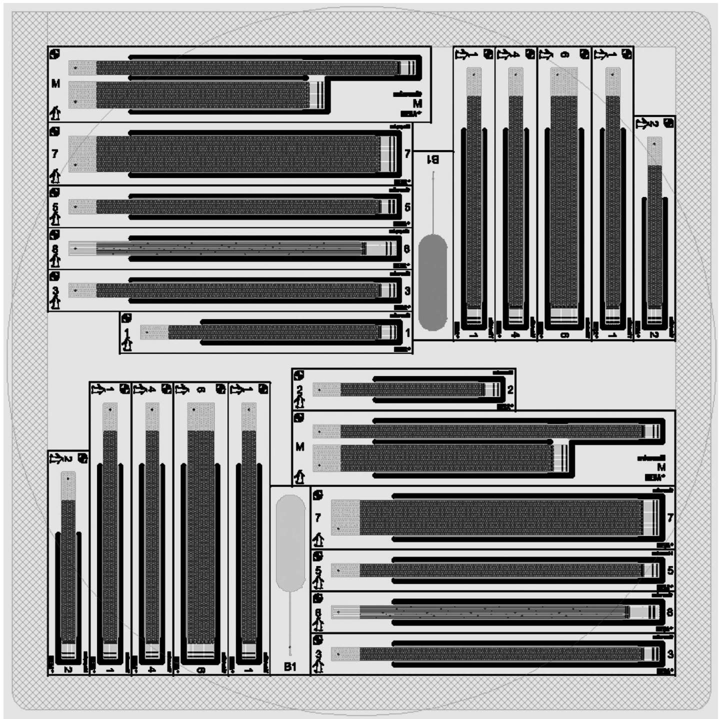

Magnification of separate masks
of cooler #1

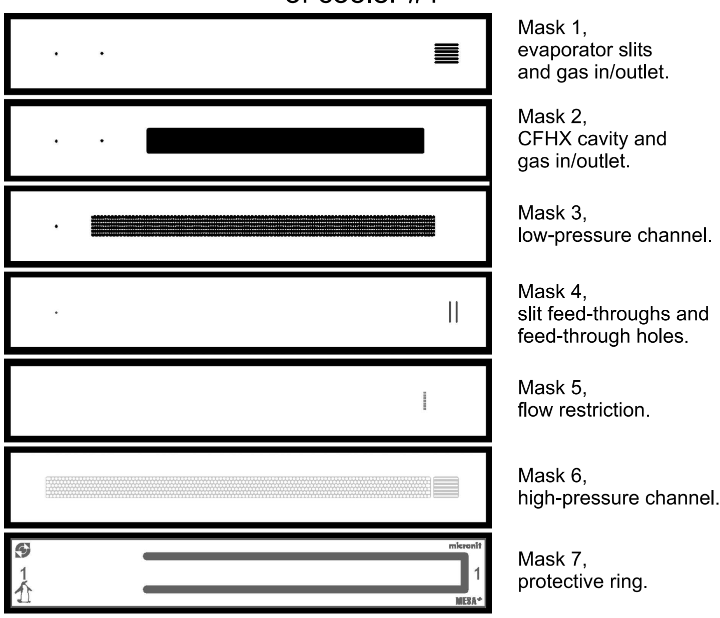

Figure C.1: Mask layout.

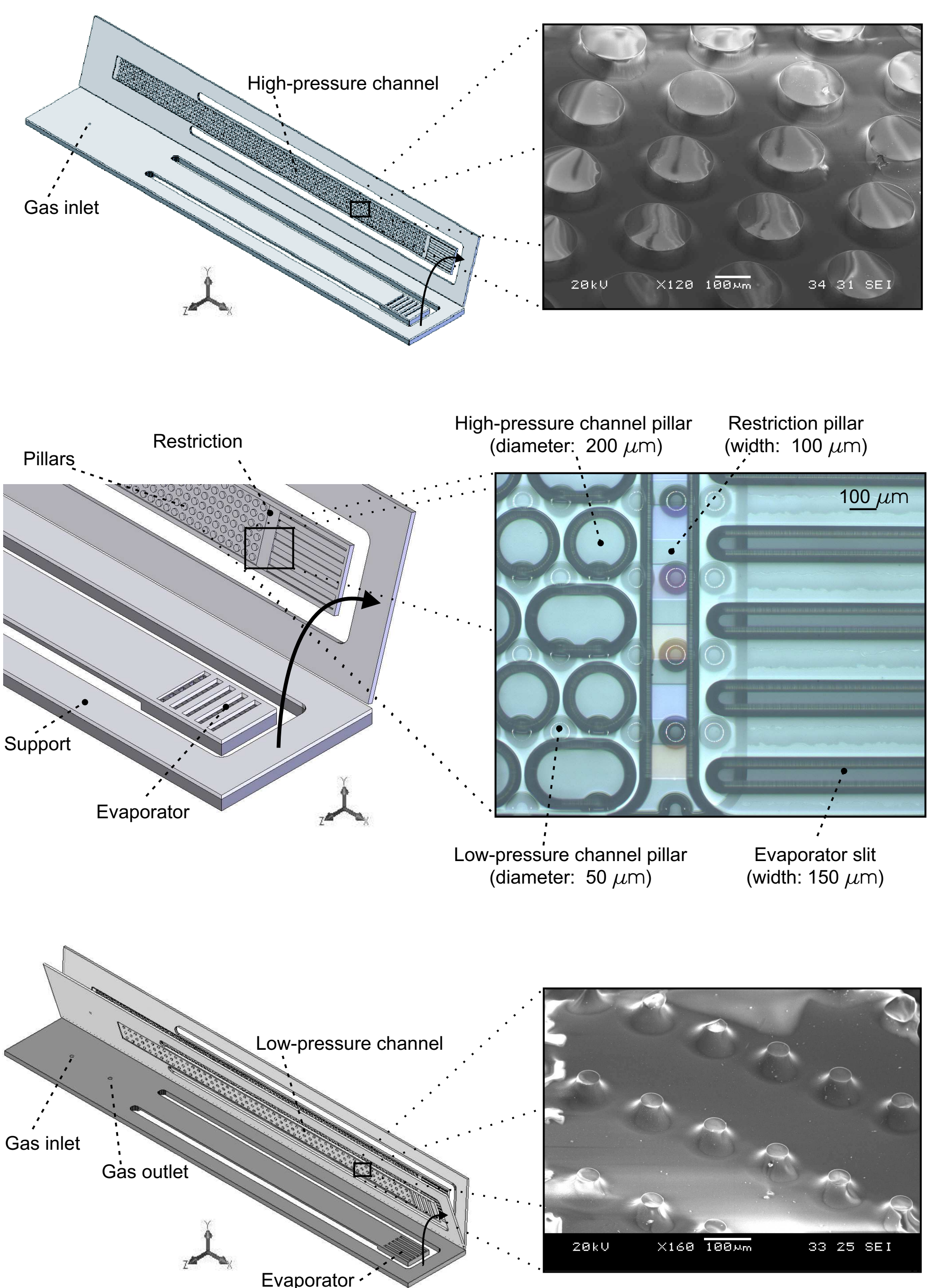

Figure C.2: Schematics and detailed (SEM) pictures of the fabricated cold stages.

Appendix D

Getter data sheet

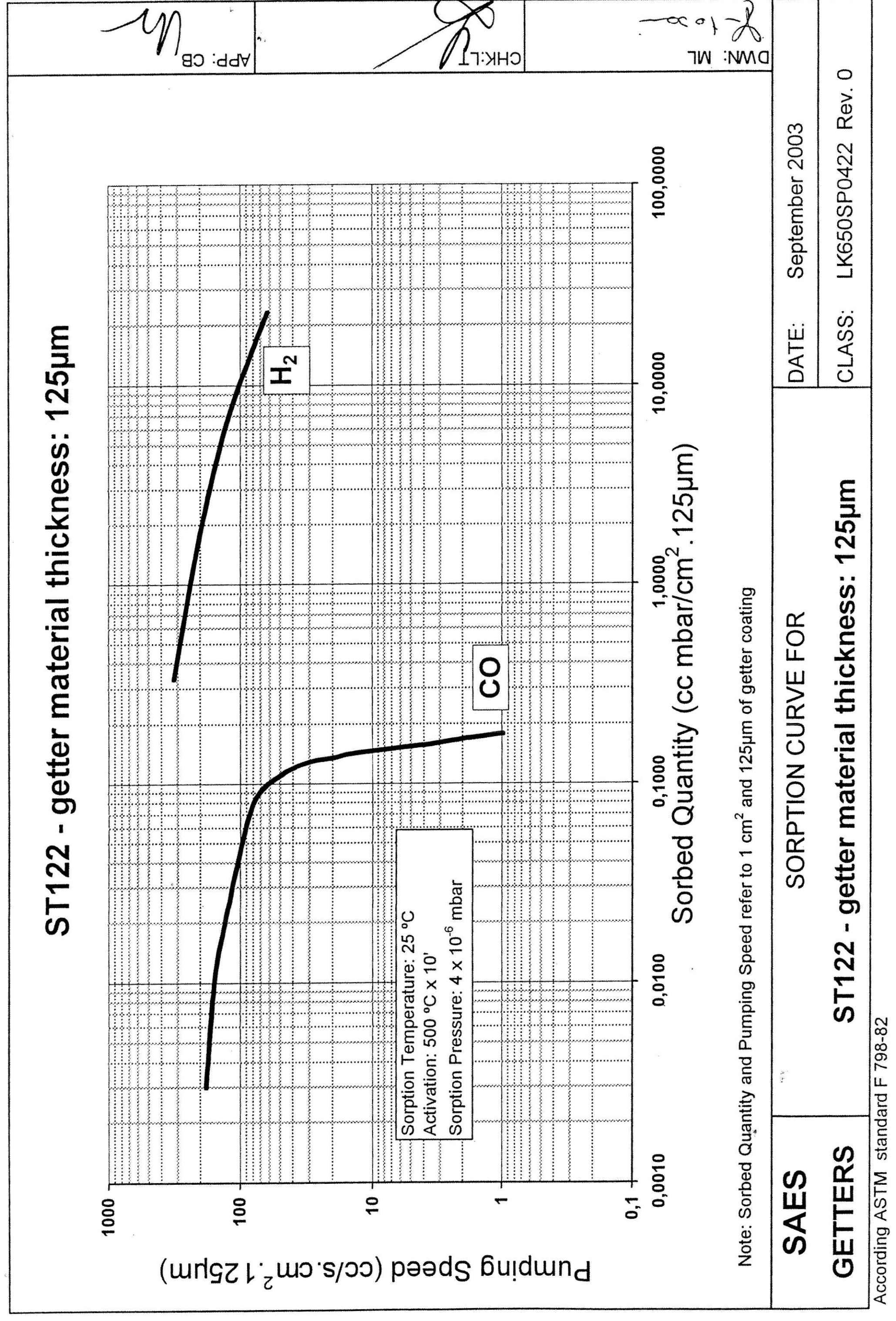

Figure D.1: ST122 getter data sheet.

Summary

Cooling of electronic circuitry to very low temperatures can improve the signal-to-noise ratio and bandwidth of a system. In many cases the system, which is to be cooled, is very small so an accompanying small cooler would be obvious. This thesis describes the research performed in designing, optimizing and fabricating a cryogenic micro cold stage by means of MEMS (Micro-Electro-Mechanical Systems) technology only. This technology is highly suitable for the fabrication of a micro cooler because of the high accuracy, possibility to integrate the system with the electronic circuitry and use of batch processing, which can result in relatively low cost per unit.

The goal is to develop a micro cold stage based on the recuperative Linde-Hampson cooling cycle with a total volume smaller than 1 cm^3. Nitrogen gas is chosen as the work fluid because it has a cryogenic boiling temperature, its cheap, non toxic and inflammable. To create sufficient cooling power, a pressure change from 80 to 6 bar is chosen which for nitrogen results in a cooling enthalpy of about 14.7 $J \cdot g^{-1}$. The boiling temperature of nitrogen at 6 bar is about 96 K. Using these pressures also opens the possibility to combine the cold stage with a sorption compressor. Because of its low thermal conductivity and compatibility with the available MEMS technology and knowledge, borosilicate glass (D263T) is chosen as the construction material of the micro cold stage.

The micro cooler is designed for those applications where the device to be cooled has a very low dissipation or no dissipation at all. In these cases the required cooling power is mainly determined by the total parasitic heat load from the environment. By a clever design of the cryogenic enclosure of such a small device, the required cooling power can be limited to a few mW only. Therefore, we aim at a net cooling power of about 10 mW. The mass flow is in the order of 1 $mg \cdot s^{-1}$ to create a gross cooling power of about 15 mW. This implies that a total parasitic heat loss of only 5 mW is accepted.

The CFHX is a crucial part of the system since a lot of heat (about 16 times more than the gross cooling power) is being transported from the high-pressure to the low-pressure gas, which strongly increases the overall COP of the cold stage. It is therefore essential that the CFHX design is optimized. The dimensions of the CFHX are optimized by minimizing the entropy that is generated. In this optimization, all heat- and pressure-drop losses in the CFHX are written as a production of entropy. By minimizing the total entropy production, it is possible to find an optimal CFHX configuration, which has minimum losses and thus maximum COP. The channel dimensions of the optimal micro CFHX, which are based on this optimization study, are: 37 mm x 2.1 mm x 53 μm. This specific design has a COP of about 0.063 and should generate a net cooling power of about 14.0 mW. If more heat loss is accepted, the CFHX can have smaller dimensions but it will also have a lower net cooling power. For a net cooling power of about 10 mW an optimal channel size of 17 mm x 2.0 mm x 35 μm was calculated which has a COP of

about 0.055.

Mechanical stress calculations show that due to the high gas pressure inside the channels, the stress in the CFHX body can exceed maximum stress values for glass which could result in a mechanical failure. Both the high- and low-pressure channels as well as the restriction are supplied with pillars to keep the stress within limits. Because of these pillars, the pressure drop in the flow channels will be higher than the calculated pressure drop in the entropy minimization study. To compensate for the influence of the pillars on the pressure drop, the height of the channels is increased from 35 μm to 50 μm. The optimum configuration, using the minimization of entropy principle, for that height is: 25 mm x 2.0 mm x 50 μm with a net cooling power of 12.6 mW, see table D prototype number 1. Besides this "optimal" design, seven other designs, all based on it, are fabricated.

The micro cooler is fabricated in D263T glass wafers using HF etching and abrasive etching (a.k.a. powder blasting). The production process has seven lithography steps and roughly 100 process steps. The cold stage consists of a stack of three wafers that are connected through a fusion bonding process. In two of the wafers, micro channels are etched to transport the gas from the inlet to the restriction and back from the evaporator to the outlet. To create a mass flow of 1 mg$\cdot$s^{-1} with a pressure difference of 74 bar, the height of the restriction has to be only 300 nm. The cold stage is surrounded by a supportive ring for protection and to simplify handling. This ring is thermally separated from the cold stage. This support also facilitates the integration of the cold stage with a micro vacuum chamber in a later phase of the project. From the eight initial designs, six (five single stages and one multistage) survived the production process and were tested in a measurement setup.

All of the tested single stage designs cooled down to liquid nitrogen temperature ($\pm$100 K). Cooling power measurements indicated that the micro cold stages suffer from a parasitic heat load induced by the measurement setup. This heat load is calculated and strongly depends on the chosen surface emissivities of the used thermocouple, wiring and the heater. Both a minimum and maximum value is estimated and found to be respectively 6 mW and 10 mW. The measured net cooling powers of the different cold stages are compensated for this heat load, see table 1.

Table 1. Cold stage prototype, measurement results.

Prototype number	**1**	**2**	**4**	**5**	**6**
CFHX channel width [mm]	2.0	2.0	2.0	2.0	4.0
CFHX channel length [mm]	25	15	25	35	25
Mass flow [mg$\cdot$s^{-1}]	1.0	1.0	2.0	2.0	2.0
P_{net} calculated [mW]	12.6	7.8	20.0	24.1	25.5
P_{net} measured [mW]	3	1	7.5	16	13
P_{net} compensated [mW]	11 $\pm$ 2	9 $\pm$ 2	15.5 $\pm$ 2	24 $\pm$ 2	21 $\pm$ 2

Results show that most of the expected cooling powers are located within the measured net cooling power domain. For two cold stages, numbers 4 and 6, the measured power is less than the expected value. This is due to unintentional variations in the measurement setup. It is clear that the measurement setup has a large influence on the determination of the net cooling power which results in a large uncertainty. Nevertheless, the results are certainly satisfying and it can be concluded that the used calculation model gives a reliable prediction of the net cooling power of a micro cold stage.

A critical issue in the operation of the micro cooler is clogging caused by the deposition of water molecules. Water molecules deposit inside the CFHX and deposited ice crystals

migrate to the flow restriction, thus blocking the flow and reducing the cooling power. As a result, the cold tip warms up and the deposited water moves to the evaporator part. This clogging phenomenon has been investigated extensively which provided significant insight in the way this clogging develops. In the future, these micro coolers will be combined with small compressors thus establishing closed-cycle micro refrigerators. By carefully pumping and purging these devices prior to closing, the amount of residual water can be limited. If the restriction does clog, the deposited water can be removed using a small heater at the cold tip. This way all water present in the system can be moved through the cold stage and collected at the warm end by adequate filtering. In this respect, the application of sorption compressors is very attractive.

For thermal insulation and thus to operate properly, the micro cold stage needs to be situated inside a vacuum environment. A vacuum package has been miniaturized using MEMS technology to create such a vacuum environment for the micro cooler. The chamber volume (≈ 0.1 cm^3) is encapsulated in a stack of three wafers. The bottom and middle wafers are made of glass and the top wafer of silicon. The pressure inside the chamber is measured via a thin film Pirani sensor which is deposited on a small cantilever powder blasted in the middle wafer. The dimensions of this cantilever approximate the dimensions of a typical micro cooler. The vacuum package includes electrical feedthroughs for power supply and voltage read-out. Calculations show that in order to provide sufficient vacuum insulation, the pressure inside the chamber should stay below about 10^{-3} mbar. Chamber pressures in the order of 10^{-3} mbar or below have been reached. However, due to physical leaks no long-life vacuum has been established. The package with the smallest leak had a leak rate of about $3 \cdot 10^{-8}$ mbar$\cdot$cm$^3\cdot$s^{-1} and showed getter saturation after approximately 4 days. It is expected that tenting along the electrical feedthroughs is causing the leaks.

Samenvatting

Koeling van elektronica naar zeer lage temperaturen kan de signaal-ruis verhouding en de bandbreedte van een systeem verbeteren. In veel gevallen is het te koelen systeem erg klein waarbij het gebruik van een kleine koeler zou dus voor de hand liggen. In dit proefschrift wordt het onderzoek naar het ontwerp, de optimalisatie en fabricage van een cryogene microkoeler met behulp van uitsluitend MEMS (Micro-Electro-Mechanical Systems) technologie beschreven. Deze technologie is vanwege zijn hoge nauwkeurigheid, mogelijkheid tot integratie van het systeem met de elektronica en het gebruik van een "batch" proces, wat mogelijk resulteert in een lage stukprijs, zeer geschikt voor de fabricage van een microkoeler.

Het doel is om een microkoeler te ontwikkelen welke gebaseerd is op de Linde-Hampson koelcyclus en een totaal volume heeft wat kleiner is dan 1 cm^3. Stikstof gas is gekozen als werkgas aangezien het een cryogene kooktemperatuur heeft, goedkoop is, chemisch inert en niet lichtontvlambaar. Een drukverschil van 80 naar 6 bar is gekozen om voldoende koelvermogen te creëren wat voor stikstof resulteert in een koel-enthalpie van ongeveer 14.7 $J{\cdot}g^{-1}$. De kooktemperatuur van stikstof bij 6 bar is ongeveer 96 K. Het gebruik van deze drukken opent tevens de mogelijkheid de koude trap te combineren met een sorptiecompressor. Borosilicate glas (D263T) is gekozen als fabricage materiaal voor de microkoeler vanwege zijn lage thermische geleidingscoëfficiënt en compatibiliteit met de beschikbare MEMS technologie en kennis.

De microkoeler is ontworpen voor die toepassingen waar het te koelen systeem nauwelijks of geen dissipatie heeft. In deze gevallen wordt het vereiste koelvermogen met name bepaald door de totale parasitaire warmtebelasting van de omgeving. Door een ingenieus ontwerp van de cryogene behuizing van het systeem kan het koelvermogen beperkt worden tot slechts een aantal mW. Er wordt daarom gemikt op een netto koelvermogen van ongeveer 10 mW. De massastroom in het systeem is ordegrootte 1 $mg{\cdot}s^{-1}$ wat resulteert in een bruto koelvermogen van ongeveer 15 mW. Dit impliceert dat slechts 5 mW aan totale parasitaire warmtebelasting wordt geaccepteerd.

De tegenstroomwarmtewisselaar (TSWW) is een cruciaal onderdeel in het systeem aangezien veel warmte (ongeveer 16 keer het bruto koelvermogen) getransporteerd wordt van hoge druk- naar het lage druk gas. Aangezien dit in hoge mate de efficiëntie van de koude trap bevorderd is het essentieel dat het TSWW ontwerp wordt geoptimaliseerd. De dimensies van de TSWW worden geoptimaliseerd door de gegenereerde entropie te minimaliseren. Alle warmte en drukval verliezen worden geschreven als een productie van entropie. Door de totale entropie productie te minimaliseren is het mogelijk een optimale TSWW configuratie te vinden welke minimale verliezen en daardoor een maximale efficiëntie heeft. De kanaaldimensies van de optimale micro TSWW, die op deze optimalisatie studie gebaseerd zijn, zijn: 37 mm x 2.1 mm x 53 μm. Dit specifieke ontwerp

heeft een efficiëntie van ongeveer 0.063 en heeft een potentieel netto koelvermogen van ongeveer 14.0 mW. Als meer warmteverlies wordt geaccepteerd, is het mogelijk de TSWW dimensies te reduceren wat echter ook resulteert in een lager netto koelvermogen. Voor een netto koelvermogen van ongeveer 10 mW is een optimale kanaalgrootte van 17 mm x 2.0 mm x 35 μm berekend met een efficiëntie van ongeveer 0.055.

Mechanische stressberekeningen tonen aan dat, als gevolg van de hoge gasdruk in de kanalen, de stress in de TSWW behuizing, de maximaal toelaatbare stress waarde voor glas kan overschrijden. Hierdoor kan de behuizing bezwijken onder de druk. Zowel de hoge als lage druk kanalen als ook de restrictie worden voorzien van paaltjes om de stress binnen de limiet te houden. Door toedoen van deze paaltjes zal het drukval in de kanalen echter hoger zijn dan de berekende waarde in de entropiestudie. Ter compensatie wordt de kanaalhoogte vergroot van 35 μm naar 50 μm. De optimale configuratie voor deze hoogte, welke wederom wordt bepaald via het minimalisatie van entropie principe, is: 25 mm x 2.0 mm x 50 μm met een netto koelervermogen van 12.6 mW, zie tabel D prototype nummer 1. Naast dit "optimale" ontwerp zijn er nog 7 andere ontwerpen gefabriceerd. Al deze ontwerpen zijn gebaseerd op het "optimale" ontwerp.

De microkoelers worden geproduceerd in D263T glazen wafers via HF ets en poederstraaltechnieken. Het productieproces heeft zeven lithografiestappen en ruwweg honderd processtappen. De koude trap bestaat uit 3 "gefusionbonde" wafers. In twee van deze wafers zijn microkanalen geëtst waardoor het gas vanaf de ingang naar de restrictie wordt getransporteerd. Van daaruit gaat het door de verdamper terug naar de uitgang. Om een massastroom van 1 mg$\cdot$s^{-1} bij een drukval van 74 bar te creëren is een restrictiehoogte van slechts 300 nm vereist. De koude kop wordt gesteund door een glazen ring ter bescherming. Deze ring heeft geen thermisch contact met de koude kop en maakt tevens integratie van een mogelijke micro vacuümkamer, tijdens een later stadium van het project, mogelijk. Van de acht initiële ontwerpen hebben er zes, vijf ééntraps- en één meertrapskoeler, het productieproces overleefd en zijn getest in een meetopstelling.

Alle ééntrapskoelers koelen af naar vloeibare stikstof temperatuur ($\pm$100 K). Uit koelvermogensmetingen blijkt dat de microkoelers last hebben van de parasitaire warmtebelasting van de meetopstelling. Deze warmtebelasting is berekend en hangt sterk af van de gekozen oppervlakte-emissiviteit van het gebruikte thermokoppel, bedrading en het stookelement. Er is zowel een maximale als minimale schatting gemaakt voor dit verlies en deze zijn respectievelijk 6 mW en 10 mW. De gemeten netto koelvermogens van de verschillende koude trappen zijn gecompenseerd voor deze warmtebelasting, zie tabel 1.

Tabel 1. Meetresultaten van de verschillende koude trappen.

Prototype nummer	**1**	**2**	**4**	**5**	**6**
TSWW kanaal breedte [mm]	2.0	2.0	2.0	2.0	4.0
TSWW kanaal lengte [mm]	25	15	25	35	25
Massastroom [mg$\cdot$s^{-1}]	1.0	1.0	2.0	2.0	2.0
P_{netto} berekend [mW]	12.6	7.8	20.0	24.1	25.5
P_{netto} gemeten [mW]	3	1	7.5	16	13
P_{netto} gecompenseerd [mW]	11 $\pm$ 2	9 $\pm$ 2	15.5 $\pm$ 2	24 $\pm$ 2	21 $\pm$ 2

In de resultaten is te zien dat het merendeel van de verwachtte koelvermogens binnen het gemeten domein liggen. Voor de prototypes nummer 4 en 6 is het gemeten koelvermogen echter minder dan verwacht. Dit is te wijden aan onbedoelde variaties in de meetopstelling. Het is duidelijk dat de meetmethode een grote invloed heeft op de bepaling van het netto koelvermogen wat resulteert in een grote meetfout. Desalniettemin zijn

de resultaten bevredigend en kan er worden geconcludeerd dat het gebruikte rekenmodel een betrouwbare voorspelling geeft voor het netto koelvermogen van een microkoeler.

Een kritische kwestie in de werking van de microkoeler is verstopping veroorzaakt door de depositie van watermoleculen. Watermoleculen deponeren in de warmtewisselaar en migreren richting de restrictie waardoor de stroming wordt geblokkeerd en het koelvermogen afneemt. Hierdoor warmt de koude kop op en begeven de gedeponeerde watermoleculen zich richting de verdamper. Dit verstoppingfenomeen is uitgebreid onderzocht wat inzicht heeft verschaft in de manier waarop de verstopping zich ontwikkelt. In de toekomst zal de koelcyclus gesloten zijn door de microkoeler te combineren met een kleine compressor. De hoeveelheid water resterend in de koeler kan worden gelimiteerd door, voorafgaand aan de sluiting van het systeem, de koeler af te pompen en te spoelen. Mocht de restrictie toch verstoppen, kan het deponeerde water worden verwijderd met behulp van een klein verwarmingselement bevestigd op de verdamper. Zodoende kan al het water zich door het systeem verplaatsen en aan de warme kant worden verzameld met behulp van adequate filtering. In dit opzicht bieden sorptiecompressoren een uitkomst.

De microkoeler bevindt zich in een vacuümomgeving voor thermische isolatie wat cruciaal is om goed te functioneren. Om zo'n omgeving te creëren is de vacuümbehuizing geminiaturiseerd met behulp van MEMS technologie. Het kamervolume van ongeveer 0.1 cm^3 wordt gefabriceerd in een stapel van drie wafers. De onderste en middelste wafer bestaan uit glas en de bovenste uit silicium. De druk in de vacuümkamer wordt gemeten met behulp van een dunne film Piranisensor welke gedeponeerd is op een kleine vinger die gepoederstraald is in de middelste wafer. De dimensies van deze vinger komen overeen met de dimensies van een typische microkoeler. Elektronische doorvoeren ten behoeve van stroomvoeding en uitlezing zijn geïntegreerd met de vacuümbehuizing. Berekeningen tonen aan dat de druk in de micro vacuümkamer lager moet zijn dan 10^{-3} mbar om goede thermische isolatie te verzekeren. Kamerdrukken van 10^{-3} mbar en lager zijn gerealiseerd. Deze lage druk kon echter niet voor langere duur in stand worden gehouden aangezien al de behuizingen niet volledig hermetisch gesloten waren. De behuizing met het kleinste luchtlek had een lekstroom van ongeveer 10^{-8} mbar·cm^3·s^{-1} waarbij getterverzadiging na ongeveer 4 dagen was bereikt. De verwachting is dat openingen langs de elektronische doorvoeren de lekkage veroorzaken.

Dankwoord

Hoe interessant de wetenschappelijke inhoud van een proefschrift ook moge zijn, het dankwoord is en blijft het meest gelezen gedeelte. Het schrijven van deze pagina's dwingt de auteur terug te kijken op zijn promotie, zich alle hulp van eenieder te herinneren. Als je alle mensen op een rijtje zet besef je pas hoeveel personen er hebben meegewerkt aan dit project. Het is dan ook een goed gebruik deze persoonlijk te bedanken.

Allereerst wil ik mijn promotor Horst Rogalla bedanken voor het bieden van de mogelijkheid om bij de leerstoel Lage Temperaturen mijn promotie te vervullen.

Marcel ter Brake, bedankt dat je mij vier jaar geleden wist over te halen deze promotieplek aan te nemen. Ik kan me nog goed herinneren dat ik voor mezelf had besloten niet te gaan promoveren en vooral na mijn afstuderen niet langer in 't Twentse land te blijven hangen. Echter, na wat vakkundig propagandawerk van jouw kant voor een toch wel erg mooie opdracht was ik om. Dit betekende nog vier jaar Enschede en je weet, ik was niet zo'n Twente fan. Ik heb er echter geen dag spijt van gehad, sterker nog, ik ben ontzettend blij dat ik het heb gedaan! Ook de persoonlijke samenwerking met jou is iets waar ik met veel plezier op terugkijk. Menig kleine vraag liep uit op een urenlange discussie. Jouw enthousiasme en kritische blik hebben bijgedragen aan het resultaat wat voor ons ligt. Ook buiten het werk, tijdens vele congressen, uitjes, of pokeravonden was de sfeer altijd goed en gezellig. Nogmaals bedankt.

De oorsprong van het Twentse microkoeling project is te vinden bij het werk van Johannes Burger. Dankzij het succes van Johannes zijn promotiewerk mocht ik aan de slag met het vervolg. Betreffende Johannes zou ik graag willen beginnen met een observatie. Johannes, ik zou jou willen typeren als een echte "die-hard fysicus". Precies in je werk, ultiem nieuwsgierig, (tikkeltje) verstrooid en altijd druk met duizend-en-één dingen tegelijk. Je gaat helemaal op in je werk en vindt het altijd leuk om erover te vertellen. Ik mocht hier dan ook vaak van profiteren. De keerzijde van de medaille was echter wel dat je vaak te druk was voor overleg of moest afzeggen voor bijeenkomsten. Desalniettemin hebben vaak de kleinste opmerkingen of suggesties de grootste invloed en voor al die kleine opmerkingen wil ik je hartelijk bedanken.

Harry Holland heeft me de laatste vier jaar bijgestaan als technische vraagbaak. Ideeën zijn leuk maar ze in het lab voor elkaar krijgen is een tweede. Harry, je pragmatische aanpak van problemen en brede kennis van zaken hebben mij geholpen in het behalen van mooie resultaten. Immer simpele oplossingen voor moeilijke problemen.

Het dynamische duo voor de kennis en de handigheidjes op het gebied van de micromechanica was ongetwijfeld Gunter Venhorst en Theo Veenstra. Gunter, bedankt voor het eindeloos tekenen en aanpassen van de maskers. Dit is in mijn ogen wel één van de meest frustrerende jobs tijdens het project geweest. Theo, bedankt voor al je inbreng, het meedenken en het sleutelen. Samenwerken met jou ging altijd zeer relaxed en ik vond

onze discussies over muziek altijd erg boeiend. Hopelijk is Harry niet meer boos op ons vanwege 't akkefietje met de vacuümpomp. Het was misschien toch niet zo'n goed idee 5 bar op de pomp te zetten.

Srinivas Vanapalli, compagnon en concurrent in het microkoeling gebied. Ik wil je bedanken voor de prettige samenwerking en alle nuttige discussies.

Behalve alle mensen die rechtstreeks bij mijn project betrokken waren wil ik ook graag alle andere mensen van koeling en instrumentatie bedanken: Gideon, Bert, Erwin en Robert-Jan, bedankt voor alle hulp, al 't koffiegezelschap de vele aangename uitjes.

Alle medewerkers van Lage Temperaturen wil ik bedanken voor hun hulp her en der en het gezelschap in de (ex)koffiekamer. Ook Ans en Inke wil ik hartelijk bedanken voor al het geregel en alle praatjes. ATF (Aio-Task-Force), bedankt voor de mooie presentaties, tips en vooral de vele Grolschjes.

Tijdens mijn promotie heb ik ook een aantal studenten mogen begeleiden gedurende hun stage en/of afstuderen. Zij hebben tijdens hun werk vaak belangrijke metingen verricht. Joost Beukers en Robert-Jan Meijer, bedankt voor al jullie werk. In het geval van Joost Koning bleef het niet alleen bij een paar mooie resultaten maar resulteerde het werk in een hoofdstuk van dit proefschrift. Joost, bedankt voor al je werk en voor het feit dat je je afstudeerverslag in LaTeX hebt gemaakt!

Ook alle mensen van Micronit wil ik graag bedanken voor hun vakkundig werk. Met name wil ik Ronny van 't Oever, Chantal Berendsen en Marko Blom bedanken voor hun inzet. De mensen van de "MicMec" wil ik bedanken voor de tips, aanwijzingen en handige trucjes om glas te bewerken. Met name Henri Jansen, Martijn Goedbloed en Jan van Nieuwkastelen wil ik hiervoor bedanken.

Naast alle hulp welke rechtstreeks betrekking heeft gehad op mijn werk zijn er ook veel mensen die mijn promovendusleven een stuk aangenamer hebben gemaakt op het sociale vlak. Met kop en schouders steekt daarboven uit: Ronald Sipkema, alias Roon, alias FrD. Ronnie, bedankt voor al het amusement. Om en nabij 180 liter Senseo koffie, 16.2 kilo separator vlees, 180 noedel soeppies, 15 liter "bei'passundâh sâus", 3600 koffiekoekjes en 33750 "kills" hebben zeker gezorgd voor een hoop plezier en ontspanning. Ook van de synthesizers, audio interfaces, Behringer hardware, masterkeyboards en Logic konden we, en kunnen we, geen genoeg van krijgen.

Verder is daar de vriendengroep bekend onder de naam "VriendenWeekend". Beroemd en berucht voor al haar activiteiten. Naast het daadwerkelijke officiële en officieuze VW hebben we een hoop lol gehad de afgelopen jaren. Ik wil met name Daaf (a.k.a Daffie), Sijmen (a.k.a Symus), Sjoerd (a.k.a de Snauwelaere), Jeroen (a.k.a Herr Crouzen), Bart (a.k.a BarTender), Frank (a.k.a Franklin Koemans), Jelle (a.k.a Yellius Milete), Chris (a.k.a Chris... Chris... Chris...), Max (a.k.a. MaxiJazz) en Ronald Sipkema (a.k.a. FrD) bedanken voor alle uren lol tijdens de poker-, film-, spelletjes- en stapavonden en alle memorabele tripjes. Dat er nog vele mogen volgen.

Muziek... één van mijn grootste verslavingen. Deze mag ik sinds jaar en dag delen met een band. De samenstelling is door de jaren heen soms veranderd, de naam is altijd hetzelfde gebleven. De muziekstijl is in ieder geval drastisch veranderd van rock en pop heel geleidelijk naar funk en jazz. Ik wil Erik-Jan de Hoon, Bart Verdaasdonk, Joost van Ingen, Marjolein Hilgerink en Bouke Lases erg bedanken voor hun muzikale steun en toeverlaat.

Mensen van de BACO, bedankt voor de trouwe dienst! Met name de "ouwe garde": Erik, Michel, Wouter, Gossie (Martijn), Lieuwe, Maarten, Sanneke, Joris en Roel bedankt

voor al het vermaak. Hopelijk wordt "Le Baceau" ooit nog eens realiteit. Van de nieuwe lichting met name Bas en Charlotte bedankt voor al het plezier.

Ik wil mijn familie, Jos, Mieke en Michiel erg bedanken voor al hun steun en interesse in mijn werk. Pa, bedankt voor al je tips en stiekem toch vaak wijze opmerkingen. Tenslotte wil ik Susan bedanken voor al haar steun, gezelschap en liefde.

List of publications

- Lerou, P.P.P.M., Jansen, H., Venhorst, G.C.F., Holland, H.J., Veenstra, T.T., Burger, J.F., ter Brake, H.J.M., Elwenspoek, M., Rogalla, H., "Progress in micro Joule-Thomson cooling at Twente University", Cryocoolers 13, Springer Science+Business Media, Inc., New York (2005), pp. 489-496.
- Lerou, P.P.P.M., Veenstra, T.T., Burger, J.F., ter Brake, H.J.M., Rogalla, H., "Optimization of counterflow heat exchanger geometry through minimization of entropy generation", Cryogenics, (2005) 45 659-669.
- Lerou, P.P.P.M., Vanapalli, S., Jansen, H.V., Burger, J.F., Veenstra, T.T., Venhorst, G.C.F., Holland, H.J., Elwenspoek, M, ter Brake, H.J.M., Rogalla, H., "Microcooling developments at the University of Twente", Advances in cryogenic engineering: Transactions of the Cryogenic Engineering Conference - CEC 2006, Vol. 823, pp. 977-984.
- Ter Brake, H.J.M., Lerou, P.P.P.M., Vanapalli, S., Jansen, H.V., Burger, J.F., Veenstra, T.T., Venhorst, G.C.F., Holland, H.J., Elwenspoek, M.and Rogalla, H., "Microcooling research at the University of Twente", ICEC 2006.
- Lerou, P.P.P.M., Vanapalli, S., Jansen, H.V., Burger, J.F., Veenstra, T.T., Venhorst G.C.F., Holland, H.J., Elwenspoek, M., ter Brake, H.J.M., Rogalla, H., "Microcooling developments at the University of Twente", to be published in Advances in Cryogenic Engineering, (2006).
- Lerou, P.P.P.M., Venhorst, G.C.F., Berends, C., Veenstra, T.T., Blom, M., Burger, J.F., ter Brake, H.J.M., Rogalla, H., "Fabrication of a micro cryogenic cold stage using MEMS-technology", Journal of Micromechanics and Microengineering, (2006) 16 1919-1925.
- Lerou, P.P.P.M., Jansen, H., Venhorst, G.C.F., Holland, H.J., Veenstra, T.T., Burger, J.F., ter Brake, H.J.M., Elwenspoek, M., Rogalla, H., "All-micromachined Joule-Thomson cold stage", Cryocoolers 14, (2007).
- Lerou, P.P.P.M., ter Brake, H.J.M., H.J. Holland, Burger, J.F., Rogalla, H., "Insight in clogging of MEMS based micro cryogenic coolers", accepted for publication in Applied Physics Letters 90, (2007).